University of Zagreb
Faculty of Mechanical Engineering and Naval Architecture

MASTER'S THESIS

Jelena Mačak

Zagreb, 2018

University of Zagreb
Faculty of Mechanical Engineering and Naval Architecture

MASTER'S THESIS

CFD Simulation of Wall Wetting with the Volume of Fluid and Thin Liquid Film Approach

Mentor:
prof. dr. sc. Hrvoje Jasak

Student:
Jelena Mačak

Zagreb, 2018

First of all, I have to express my respect and gratitude to my mentor, Prof. Hrvoje Jasak, for giving me the opportunity to expand my knowledge in more ways than I could ever have imagined.
I am also grateful to Prof. Željko Tuković – without his help, I'd hardly be able to complete my task.
A sincere thank you goes to all of the assistants who offered me help and valuable advice, especially to Mr. Vuko Vukčević, for all the patience and kindness I received.
I am very thankful to Prof. Edin Berberović, for making his code for Kistler's contact angle model public. This alleviated the pains of my first encounters with C++.
I also have to thank Ms. Izidora Herold, for solving many administrative issues.
I am grateful to all of my loving friends and colleagues – especially to those who shared the room 816 with me, and who became exceptionally dear to me.
Finally, I am grateful to my parents, without whom I would not be.

Statement | Izjava

I hereby declare that I have made this thesis independently using the knowledge acquired during my studies and the cited references.

Izjavljujem da sam ovaj rad radila samostalno koristeći znanja stečena tijekom studija i navedenu literaturu.

Zagreb, July 2018 Jelena Mačak

SVEUČILIŠTE U ZAGREBU
FAKULTET STROJARSTVA I BRODOGRADNJE
Središnje povjerenstvo za završne i diplomske ispite
Povjerenstvo za završne i diplomske ispite studija zrakoplovstva

Sveučilište u Zagrebu Fakultet strojarstva i brodogradnje	
Datum	Prilog
Klasa:	
Ur.broj:	

DIPLOMSKI ZADATAK

Student: **Jelena Mačak** Mat. br.: 0035189694

Naslov rada na hrvatskom jeziku: **Simulacija interakcije kapljice i zida proračunskom mehanikom fluida i formulaciji modela slobodne površine i tankog tekućeg sloja**

Naslov rada na engleskom jeziku: **CFD Simulation of Wall Wetting with the Volume of Fluid and Thin Liquid Film Approach**

Opis zadatka:

Aircraft are subject to buildup of ice, frost and/or snow on their surfaces while on the ground during cold weather in the presence of high relative humidity, rain and/or snow. Safe operation of aircraft in cold weather involves deicing of wings and fuselage by means of a thin liquid film of deicing liquid, applied in spray form to aircraft body. Deicing performance is critically dependent on the spreading of liquid film on surfaces, dependent on relevant physical properties of the system: density and viscosity ratio, surface tension and liquid contact angle of the liquid-solid-air system.

In this project, feasibility of wall wetting simulations by means of Computational Fluid Dynamics (CFD) shall be examined. Two model formulations shall be considered: a 3-D two-fluid free surface Volume of Fluid (VoF) flow model and a 2-D thin liquid film model.

The candidate shall perform the following tasks:

- Perform a literature survey on the simulation of thin liquid films using CFD. Identify relevant models for surface tension and contact angle within the framework of 3-D VoF and thin liquid film model. If adequate models do not exist, propose a physically consistent model formulation and implement it in OpenFOAM software;
- Identify from the literature a validation case related to deposition of water droplets on a surface, aimed at evaluating the phenomena related to wall wetting and moving contact lines;
- Perform a 3-D VoF CFD simulation of droplet-wall interaction. Compare the simulation results against available experimental or relevant numerical data;
- Perform an equivalent simulation of the droplet-wall interaction within the thin liquid film framework. Compare the results of the thin liquid film model with the 3-D CFD simulation and available experimental data.
- Discuss the feasibility, accuracy and relative cost of the 3-D VoF and 2-D liquid film simulations.

The Thesis shall list the bibliography and any assistance received during this study.

Zadatak zadan:	Rok predaje rada:	Predviđeni datumi obrane:
3. svibnja 2018.	5. srpnja 2018.	11., 12. i 13. srpnja 2018.

Zadatak zadao: Predsjednik Povjerenstva:

Prof. dr. sc. Hrvoje Jasak Prof. dr. sc. Ivica Smojver

Contents

List of Figures

List of Tables

List of Symbols

Subscripts

Abbreviations

Superscripts

Summary

The focus of this thesis is the numerical modelling of liquid-wall interaction, also referred to as wetting. Wetting is an important part of many industrial applications, and, for aerospace industry, it is relevant as it relates to hazardous ice accretions. Numerical study of the phenomenon could lead to safety improvements and cost reductions, which was the motivation behind the thesis.

This thesis examines the feasibility of wall wetting simulations by means of Computational Fluid Dynamics (CFD), using two model formulations: a 3-D two-fluid free surface Volume of Fluid (VoF) flow model and a 2-D thin liquid film model. Both are implemented within the CFD toolbox `foam-extend`.

Implementation of wetting was performed within the VoF `interFoam` solver and within the thin liquid film `liquidFilmFoam` solver. In `interFoam`, wetting is realized using a boundary condition, while in `liquidFilmFoam`, an additional force term was added into the momentum equation, resulting in a new mathematical formulation.

The VoF boundary condition was tested using an experiment related to droplet deposition on an inclined plate. Thin liquid film model was tested using experimental and numerical data related to rivulet flows. Methods were compared using a case of droplet exposed to shear flow on an inclined plate.

Keywords: wetting, contact angle, Volume of Fluid, thin liquid film model, CFD, `foam-extend`

Sažetak

Ovaj rad se bavi numeričkim modeliranjem fenomena kvašenja, odnosno interakcije kapljevine i nepropusne stijenke. Kvašenje je esencijalan dio mnogih industrijskih procesa, a radi svoje poveznice sa stvaranjem leda, relevantno je za zrakoplovstvo. U zrakoplovnoj industriji, numerička simulacija fenomena bi mogla dovesti do značajnih poboljšanja na polju sigurnosti kao i do smanjenja troškova, što je bila motivacija za pisanje ovog rada.

Ovaj rad istražuje mogućnosti simulacije kvašenja korištenjem proračunskih metoda računalne dinamike fluida (RDF). U radu su razmatrana dva pristupa: 3-D dvofazni model slobodne površine i 2-D formulacija tankog tekućeg sloja. Obje formulacije su implementirane unutar `foam-extend` softverskog paketa.

Kvašenje je implementirano u 3-D rješavač `interFoam` i u 2-D rješavač `liquidFilmFoam`. U `interFoam`-u, kvašenje je realizirano primjenom rubnog uvjeta, dok je u `liquidFilmFoam`-u isto ostvareno dodavanjem sile u jednadžbu očuvanja količine gibanja, dovodeći do nove matematičke formulacije modela.

Rubni uvjet modela slobodne površine je testiran usporedbom s eksperimentalnim podacima vezanim uz gibanje kapljice niz nagnutu ploču. Model tankog tekućeg sloja je testiran usporedbom s eksperimentalnim i numeričkim podacima o odvajanju struja tankog filma kapljevine. Metode su međusobno uspoređene simulacijom gibanja kapljice pogonjene strujom zraka niz nagnutu ravninu.

Ključne riječi: kvašenje, kontaktni kut, model slobodne površine, model tankog tekućeg sloja, RDF, `foam-extend`

Prošireni sažetak

Kvašenje, definirano kao sposobnost kapljevine da ostvari kontakt s krutom podlogom, je integralan dio mnogih industrijskih procesa, a za zrakoplovstvo predstavlja relevantan fenomen radi svoje poveznice s leđenjem aerodinamičkih površina. Stvaranje leda na krilima zrakoplova je direktna posljedica kvašenja: kondenzirane vodene kapljice iz oblaka, promjera većih od 50 μm, kada dospiju na površinu krila imaju tendenciju širiti se prije nego što pređu u kruto agregatno stanje. Aerodinamička hrapavost koja nastaje akumulacijom leda mijenja sliku strujanja u graničnom sloju, te posljedično dovodi do nepoželjnih promjena u raspodjeli tlaka, smanjenja uzgona, povećanja otpora te smanjenja upravljivosti zrakoplova. S obzirom da su postojeći sustavi za zaštitu od zaleđivanja energetski neefikasni, numerička analiza fenomena bi mogla dovesti do razvoja adekvatnijih rješenja.

Dinamičko ponašanje kapljevine na podlozi je fenomen kompleksnog fizikalnog opisa, gdje kontaktni kut predstavlja odlučujući parametar:

- Povlačenje kapljevine na podlozi je prisutno za kontaktne kutove manje od *povlačećeg kontaktnog kuta*, θ_r;
- Širenje kapljevine na podlozi je prisutno pri kontaktnim kutovima većim od *napredujućeg kontaktnog kuta*, θ_a;
- Kapljevina ostaje nepomična na podlozi za kontaktne kutove u području histereze, odnosno za kontaktne kutove između prethodno pomenutih graničnih vrijednosti, $\theta_r < \theta < \theta_a$.

Ovaj rad se bavi numeričkim modeliranjem dinamičkog ponašanja kapljevine korištenjem dvaju metoda računalne dinamike fluida. Razmatrana je 3-D formulacija modela slobodne površine i 2-D formulacija modela tankog tekućeg sloja.

0.1. Kvašenje u formulaciji modela slobodne površine

Kvašenje u formulaciji modela slobodne površine je ostvareno kroz rubni uvjet koji koristi Kistlerov model dinamičkog kontaktnog kuta:

$$\theta_d = f_{\mathrm{H}}(\mathrm{Ca} + f_{\mathrm{H}}^{-1}(\theta_e)) \,, \tag{0.1}$$

gdje je θ_d dinamički kontaktni kut, Ca kapilarni broj, θ_e ravnotežni kontaktni kut, a f_{H} Hoffmanova funkcija, definirana kao:

$$f_{\mathrm{H}} = \arccos\left\{1 - 2\tanh\left[5.16\Big[\frac{x}{1+1.13x^{0.99}}\Big]^{0.706}\right]\right\} . \tag{0.2}$$

Kapilarni broj iz jednadžbe (0.1) predstavlja bezdimenzijski omjer viskoznih sila i površinske napetosti:

$$\mathrm{Ca} = \frac{\mu v_{cl}}{\sigma} \,. \tag{0.3}$$

U jednadžbi (0.3), μ je dinamička viskoznost, v_{cl} je brzina kontaktne linije a σ je površinska napetnost. Brzina kontaktne linije v_{cl} se računa prema izrazu:

$$v_{cl} = \frac{\mathbf{v} \cdot \mathbf{n}_I}{\sqrt{1 - \mathbf{n}_b \cdot \mathbf{n}_I}} \,, \tag{0.4}$$

gdje je $\mathbf{v}$ vektor brzine fluida, $\mathbf{n}_I$ jedinična normala na slobodnu površinu između plina i kapljevine i $\mathbf{n}_b$ jedinična normala na podlogu.

U slučaju napredovanja kapljevine na podlozi, izraz (0.5) je istinit, te se jednadžba (0.1) računa s $\theta_e = \theta_a$. U slučaju istinitog izraza (0.6), kapljevina se povlači s podloge, a u jednadžbu (0.1) ulazi $\theta_e = \theta_r$.

$$\mathbf{v} \cdot \mathbf{n}_I > 0 \tag{0.5}$$

$$\mathbf{v} \cdot \mathbf{n}_I < 0 \tag{0.6}$$

0.2. Kvašenje u formulaciji modela tankog tekućeg sloja

U formulaciji modela tankog tekućeg sloja, kvašenje je ostvareno uvođenjem sile kontaktnog kuta $\mathbf{f}_\theta$ u jednadžbu očuvanja količine gibanja. Ova sila je definirana kao:

$$\mathbf{f}_\theta = \beta\sigma(1 - \cos\theta)\mathbf{n}_{cl} \,, \tag{0.7}$$

gdje je β faktor korekcije, σ površinska napetost, θ kontaktni kut, a $\mathbf{n}_{cl}$ jedinična normala na kontaktnu liniju.

Jedinična normala na kontaktnu liniju izražena je putem površinskog gradijenta debljine filma h:

$$\mathbf{n}_{cl} = \frac{\nabla_s h}{|\nabla_s h|} \,. \tag{0.8}$$

Dinamički kontaktni kut je proračunat uporabom Kistlerovog modela (0.1), s kapilarnim brojem Ca definiranim jednadžbom (0.3). Brzina kontaktne linije v_{cl}, potrebna za računanje kapilarnog broja, koristi izraz:

$$v_{cl} = \mathbf{n}_{cl} \cdot \bar{\mathbf{v}} \,, \tag{0.9}$$

gdje je $\bar{\mathbf{v}}$ osrednjena vrijednost brzine tankog sloja kapljevine. Ovisno o predznaku brzine v_{cl}, kapljevina napreduje ili se povlači s podloge. Za $v_{cl} < 0$, kapljevina se povlači s podloge i jednadžba (0.1) se računa s $\theta_e = \theta_r$. Za $v_{cl} > 0$, kapljevina kvasi podlogu te u jednadžbu (0.1) ulazi $\theta_e = \theta_a$.

S ciljem što fizikalnijeg numeričkog opisa, sila kontaktnog kuta $\mathbf{f}_\theta$ se računa samo za one kontrolne površine u kojima kontaktni kut postoji. Identifikacija kontrolnih površina se provodi pomoću granične visine h_p. Sve kontrolne površine kvašene visinom filma h_p se smatraju potpuno suhima. Kontrolne površine s visinom filma $h > h_p$, a koje imaju barem jednu potpuno suhu susjednu kontrolnu površinu su identificirane kao parcijalno mokre. Sukladna matematička formulacija jednadžbe očuvanja količine gibanja glasi:

$$\begin{aligned} \frac{d}{dt}\int_{S_w} h\bar{\mathbf{v}} dS + \oint_{\partial S_w} \mathbf{m} \cdot (h\overline{\mathbf{v}\mathbf{v}}) dL = \frac{1}{\rho}\int_{S_{fs}} \boldsymbol{\tau}_{fs} dS - \frac{1}{\rho}\int_{S_w} \boldsymbol{\tau}_w dS \\ + \frac{1}{\rho}\oint_{L_{cl}} \mathbf{f}_\theta dL + \int_{S_w} h\mathbf{f}_t dS - \frac{1}{\rho}\int_{S_w} h\nabla_s p dS \,. \end{aligned} \tag{0.10}$$

U jednadžbi (0.10), h je debljina filma, $\bar{\mathbf{v}}$ je osrednjena brzina filma, $\mathbf{m}$ je jedinična bi-normala na podlogu, ρ je gustoća kapljevine, $\boldsymbol{\tau}_{fs}$ je tangencijalno naprezanje na slobodnoj površini, $\boldsymbol{\tau}_w$ je viskozno naprezanje na podlozi, $\mathbf{f}_t$ je tangencijalna komponenta volumenske sile i p je tlak.

Integral po duljini kontaktne linije je numerički aproksimiran izrazom:

$$\frac{1}{\rho}\oint_{L_{cl}} \mathbf{f}_\theta dL \approx \frac{1}{\rho}\left(\frac{\mathbf{f}_\theta}{L_{PN}}\right)_P^n S_P \,, \tag{0.11}$$

gdje je L_{PN} geodetska duljina između dvaju susjednih konačnih površina. Diskretizirana jednadžba očuvanja količine gibanja glasi:

$$a_P^v \bar{\mathbf{v}}_P^n + \sum_N a_N^v \bar{\mathbf{v}}_N^n = \mathbf{r}_P^v - \frac{1}{\rho}\{[\nabla_s(hp)]_P^n - p_P^n(\nabla_s h)_P^n\}\,, \tag{0.12}$$

gdje se izvorski član $\mathbf{r}_P^v$ za parcijalno mokre kontrolne površine računa s članom sile kontaktnog kuta (0.11), dok se za sve ostale kontrolne površine u domeni računa bez navedenog člana.

0.3. Rezultati

Rubni uvjet napisan za 3-D model slobodne površine je implementiran u rješavač `interFoam`. U svrhu testiranja rubnog uvjeta, izvršena je numerička simulacija gibanja kapljice niz hidrofilnu i hidrofobnu nagnutu ploču. Kvalitativna usporedba s eksperimentalnim podacima za slučaj hidrofilne podloge je prikazana Slikom 0.1, dok je slučaj hidrofobne podloge prikazan Slikom 0.2. Simulacija je pokazala odlično poklapanje s eksperimentalnim rezultatima za napredujuće gibanje kapljice. Nesukladnosti postoje za povlačenje kapljevine, pogotovo u slučaju hidrofilne podloge.

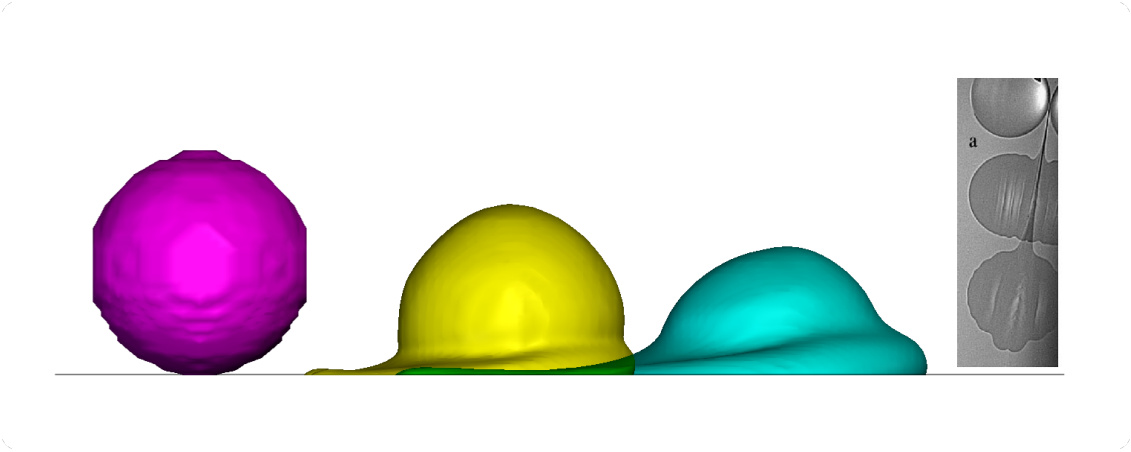

Slika 0.1: Promjena oblika kapljice na hidrofilnoj podlozi

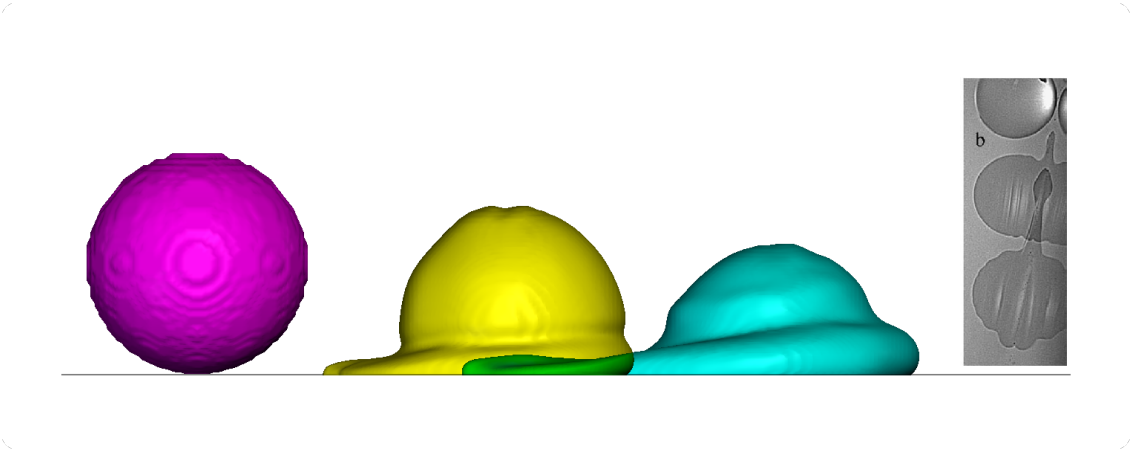

Slika 0.2: Promjena oblika kapljice na hidrofobnoj podlozi

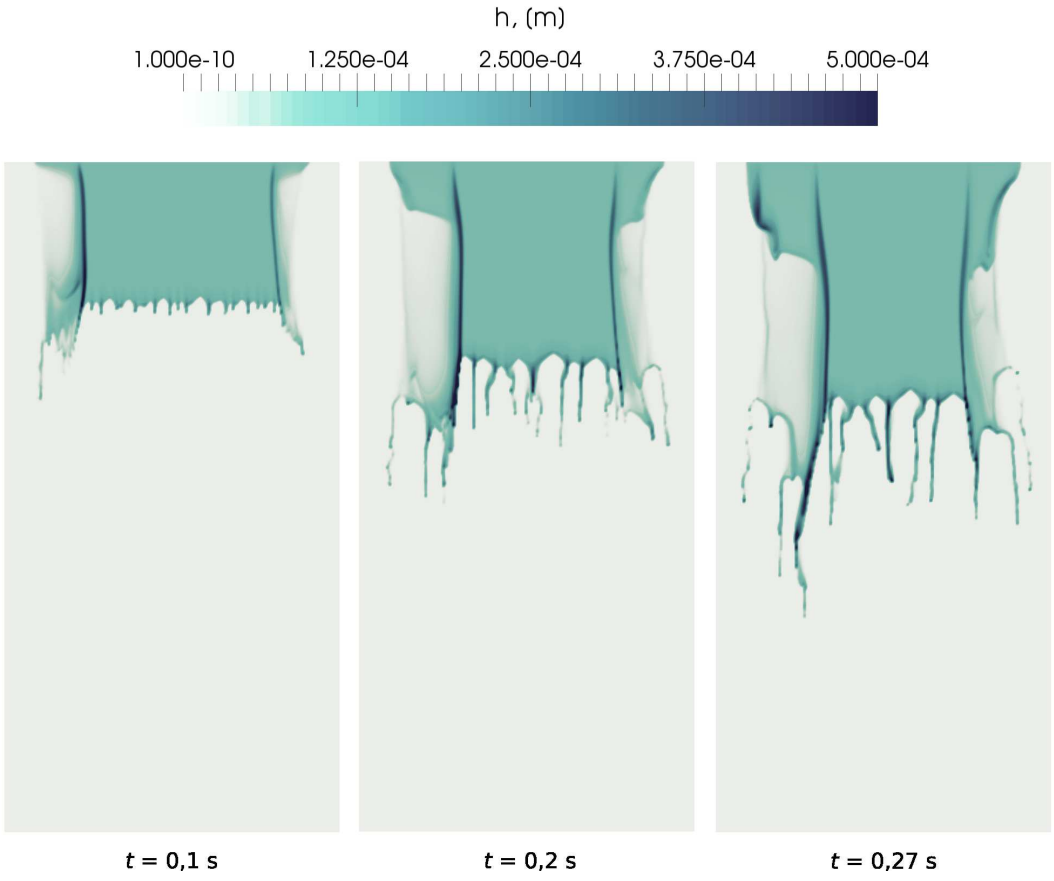

Slika 0.3: Odvajanje struja filma kapljine

Formulacija modela tankog tekućeg sloja, prilagođena za uvjete djelimičnog kvašenja podloge, je implementirana u rješavač `liquidFilmFoam`. U svrhu testiranja modela, provedena je simulacija odvajanja struja tankog tekućeg sloja na vertikalno postavljenoj ploči. Rezultati simulacije su prikazani Slikom 0.3. Odvajanje struja kapljevine je ostvareno simulacijom, međutim uočeni su problemi s divergencijom rješenja. Budući da ove nestabilnosti nisu rezultat promjena uvedenih u kod u svrhu pisanja ovog rada, razlozi za oscilacije rješenja ostaju pitanje za buduća istraživanja.

Kvalitativna usporedba rješenja dobivenih razmatranim metodama za slučaj gibanja kapljice pogonjene strujom zraka niz nagnutu ploču prikazana je Slikom 0.4. S obzirom na pomenute probleme `liquidFilmFoam` rješavača, nesukladnosti među rješenjima nisu iznenađujuće. Unatoč nefizikalnim oscilacijama u trenutnoj verziji rješavača, 2-D model tankog tekućeg sloja ostaje atraktivna potencijalna alternativa 3-D modelu slobodne površine; ekonomska isplatljivost ove metode opravdava mogućnost za daljnji razvoj.

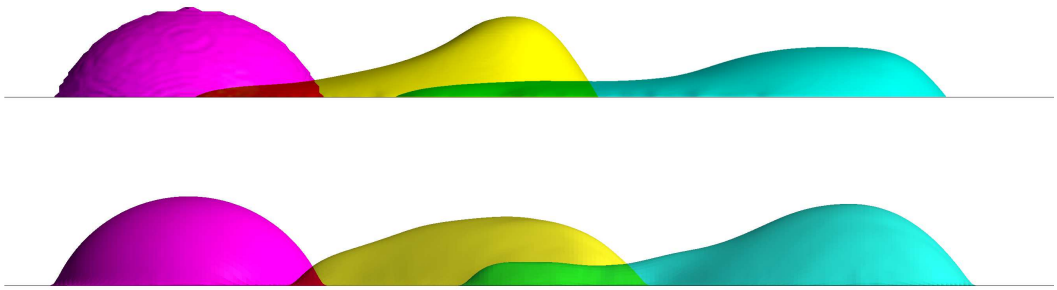

Slika 0.4: Usporedba promjene oblika kapljice: model slobodne površine (iznad), model tankog tekućeg sloja (ispod)

Chapter 1.

Introduction

Wetting, defined as the ability of a liquid to get in contact with a solid substrate, is a complex process to describe, both from scientific and engineering viewpoint. There are several outcomes for a droplet impacting a substrate. Between the initial contact and the equilibrium state, the droplet may spread, slide, roll-off, retract or remain immobile on the surface, depending on physical and chemical properties of the liquid-substrate combination and external influences, such as exposure to aerodynamic forces. Dynamic behaviour of liquid is governed by adhesion forces which arise at the contact line - the place which separates dry and wet substrate area. The pivotal property of these adhesion forces is the surface tension, defined as excess free energy per unit area linked to the formation of interface between liquid-gas phases. Influence of surface tension is observable through existence of contact angles. However, mechanisms of surface tension are resulting from molecular interactions and depend highly on the microscopic morphology of the substrate. Having a problem associated with length scales well beyond observation is the main cause of difficulty when studying wetting flows.

1.1. Droplets in Technical Processes

In spite of complexity of its physics, droplet wetting is essential to a great number of industrial applications. For example, [1] lists these technical processes where liquid-solid interaction is important:

- insecticides on leaves,

- oils on metallic surfaces,
- paints and inks,
- soldering and brazing,
- blending of polymers,
- reinforcement of polymers with fibre,
- biocompatibility of polymers,
- powder coating,
- cleaning and dyeing of fabrics,
- detergents,
- waterproofing fabrics,
- preventing deterioration of blacktop roads.

Significance of droplet flows is further illustrated by the amount of scientific interest. According to [2], topic of "droplet" is a subject of more than 6700 papers published between 1964 and 2014, in the areas of engineering, chemistry, physics, material science, energetics, environmental science, agricultural sciences, chemical engineering, biochemistry, biology, mathematics, medicine, pharmacology and others. Considering the omnipresence of water on Earth, the variety of these areas is far from surprising. Consequently, droplet flows are a frequent subject for CFD simulations. Some examples are CFD modelling of wind-driven rain [3, 4] and liquid film flow on inclined plates [5].

1.2. Wetting in Aeronautical Engineering

1.2.1. Ice Accretion

Ice accumulation on the lifting surfaces hazardously affects flight performances and reduces overall handling capabilities. Since ice poses a serious threat to flight safety, mechanisms of ice accretion are a subject of numerous research. For example in [6],

effects of ice accretion on wings, tail surfaces, engine inlets and rotary wings were experimentally investigated. Impact of supercooled large droplet ice accretions on aircraft controls was studied in [7]. The most severe consequences of icing include decreased lift, increased drag, decreased stall angle, changes in the pressure distribution, vibrations, early boundary layer transitions and reduced controllability.

In-flight icing occurs usually due to supercooled droplets impacting and freezing on a solid structure. Droplets of different diameters, impact velocities and temperatures tend to form different types of ice. These types are described in [8] as:

- **Rime ice** – rough, milky, opaque ice formed by the instantaneous freezing of small, supercooled droplets as they strike a solid surface. Rime ice normally occurs at low temperatures, below $-15°C$, low liquid water content and low airspeed;

- **Glaze ice** – clear and smooth ice resulting from supercooled droplets striking a surface but not freezing rapidly on contact. It is denser, harder, and sometimes more transparent than rime ice. Glaze ice normally occurs at warmer water temperature (between $-5°C$ and $0°C$) and higher liquid water content. In glaze icing conditions, water may flow downstream and create ice shapes including "horns", protruding from unprotected leading edge surfaces;

- **Mixed ice** – a condition where both rime and glaze ice coexist. It is observed at intermediate temperatures between $-15°C$ and $5°C$.

Considering the severe consequences of icing on flight safety, numerical simulation represents a helpful tool for prediction of ice accretion and design of systems for protection. Some examples are numerical simulation of ice accretion on a helicopter rotor [9] and numerical simulation of rime ice accretions on an aerofoil [10].

Numerical description of ice accretion is complex and multidisciplinary, with physics of wetting being of importance when studying impact of supercooled large droplets. These droplets, with diameters above 50 μm, tend to slide and spread on the surface before freezing and forming glaze ice. A reliable CFD description of liquid-surface interaction could potentially increase the accuracy of glaze ice accretion simulations.

1.2.2. Ice Protection Systems

There are two distinct types of in-flight ice protection systems: *de-icing systems*, which control the ice formation, and *anti-icing systems*, which prevent the ice formation. De-icing systems are designed to work periodically, removing the ice after it begins to accumulate. They are typically used on parts of aircraft structure where a small amount of ice accretion does not critically affect the flight performances.

Anti-icing systems are designed to completely avoid any ice formation. They are turned on before entering icing conditions and they work continuously during the entirety of flight-time. Anti-icing systems are necessary in the most critical areas, where it is required to prevent impinging droplets freezing. Most common are the thermal anti-icing systems, which either use hot bleed air from the engine compressor or an electrical power supply.

Usual *modus operandi* of the thermal anti-icing systems involves keeping the surface at temperatures well above freezing point, which causes the water droplets to evaporate upon the impact. High energy consumption needed for maintaining the evaporation temperature is justified by the avoidance of *runback ice*.

The phenomenon of runback ice was studied in [11], where it is described as ice accretion which occurs on wings with thermal anti-icing systems when the system does not evaporate 100% of the water that impinges on the surface. The water runs back from the impingement zone, leaving the leading-edge region without ice. When the water reaches the region where the added heat no longer raises the surface temperature above freezing, the water begins to freeze and a ridge line develops. Frozen rivulets follow the ridge line in cases where the air temperature is close to freezing, which leads to ice shapes with large chordwise extent.

According to [8], more than 70% energy consumed by a thermal anti-icing system is used for water evaporation. In order to reduce the cost of typical anti-icing mechanisms, which require a continuous supply of hot air, chemicals, or electrical power, *ice mitigation* techniques are used. These passive techniques use special properties of some coatings to reduce water and ice adhesion to the surface. For example, superhydrophobic coatings, studied in [8], exhibit extreme water repellency. They prevent ice formation by promoting water shedding from the surface, before freezing occurs.

Ice build-up on aircraft structure also occurs while on ground, during cold weather

in the presence of high relative humidity, rain and/or snow. In order to fulfil the requirements for airworthiness, de-icing must be performed on the affected surfaces prior to take-off. According to [12], de-icing is generally carried out by using heated fluids dispensed from spray nozzles mounted on specially designed de-icing trucks. Similar procedure is carried out when applying anti-ice coating, used as an ice mitigation tool. In both cases, liquid-solid interaction is critical for successful aircraft ground operation.

1.2.3. Other Applications

Apart from ice-related issues, droplet wetting is important when studying effects of heavy rain on the aircraft structure. For example, [13] studied erosion damage caused by rain drops. During taxiing and take-off, rain may reduce visibility and affect handling of the aircraft. One of possible rain-removal systems includes applying a hydrophobic coating on the aircraft wind-shield [14].

Liquid-solid interaction is also important for the issues related to aircraft maintenance, e.g. removing the contamination of lifting surfaces using cleaning liquids. Furthermore, obvious droplet wetting applications, such as spray painting and direct fuel injections in internal combustion engines, could be considered as aeronautical when applied to an aircraft.

Considering the variety of possible applications, CFD simulation of wetting could be beneficial to aerospace industry – especially when related to prediction of icing events, where it could be used as a valuable tool for reducing safety risks, as well as the cost. The utmost importance of both for the aeronautics was the motivation behind this thesis.

1.3. Thesis Outline

The focus of this thesis is the numerical modelling of liquid-wall interaction, also referred to as wetting.

Chapter 2. deals with the physical description of wetting phenomenon, with the most of the attention given to the nature of surface tension and how it relates to contact angles and contact line motion. Several dynamic contact angle models are described within the same chapter.

Wetting could be potentially modelled using any of the existing methods which

describe the free surface flow. Consequent to the increasing amount of scientific interest in two-phase flows, the current state of art offers several approaches, described for example in [15, 16]. This thesis considers two model formulations: a 3-D two-fluid free surface Volume of Fluid (VoF) flow model and a 2-D thin liquid film model.

Mathematical and numerical description of the VoF method is given in Chapter 3. The VoF method uses an indicator function to differentiate between the phases. From numerical point of view, the indicator function is defined as the volume phase fraction, which describes how much of a computational cell is occupied with the regarded phase. When applied to droplet flows, height of the computational cell has to be in the scale of a few dozens micrometers, in order to properly capture liquid spreading. This leads to very slow computational times, and thus makes the method expensive.

Mathematical and numerical formulation of the thin liquid film model is given in Chapter 4. Here, the computational domain is represented by the substrate surface which is completely covered by an arbitrary number of non-overlapping flat polygonal control areas. Centroids of controls areas carry the information of liquid film thickness. Being two-dimensional, this model formulation has the potential to be more efficient than the VoF method. However, two-dimensionality also limits the model to flows over hydrophilic substrates, with contact angles less than 90°.

Numerical modelling of wetting is described in Chapter 5. Wetting in the VoF `interFoam` solver is realized using a boundary condition which utilizes the Kistler's dynamic contact angle model, while in the thin liquid film `liquidFilmFoam` solver, wetting is accounted for by adding a force term into the momentum equation, which governs the liquid spreading.

Boundary condition written for the `interFoam` solver was tested by performing a simulation of water droplet impact onto an inclined plate. The results were compared to experimental data. Same experiment could not be recreated in `liquidFilmFoam` solver, due to its limitation to contact angles less than 90°. Instead, a rivulet flow simulation was performed and compared to experimental and numerical data. Methods were compared using a case of droplet exposed to shear flow on an inclined plate. Results are given in Chapter 6. Conclusion is given in Chapter 7.

Chapter 2.

Physics of Droplet Flows

2.1. Surface Tension

Surface tension is the key phenomenon of an equilibrium liquid-gas system: while the gaseous phase freely fills up the entire available domain, the liquid phase assumes a stable shape. Liquid, as a phase with greater density, has considerable intermolecular forces. These forces are balanced in the bulk fluid, where each liquid molecule is surrounded by an equal number of liquid molecules. However, in the interface region, where liquid and gas molecules meet, stronger attraction between liquid molecules causes an imbalance resulting in intermolecular forces acting towards the bulk region. In nature, this is most commonly observed in the spherical shape of water droplets.

According to [17], while the interface is a few molecular diameters order of thickness, at a macroscopic level it appears as a sharply defined region with a discontinuous change of density and other thermodynamic properties, often considered as a thin, uniformly stretched membrane. Thus, the surface tension σ, can be defined as a force acting per unit length across a line on this fictitious membrane in such a way that the liquid behaves as if enclosed in an envelope of constant tension.

Another interpretation of surface tension defines it as the excess free energy per unit area associated with the formation of interface between two phases [18]. Surface tension is not a unique property of liquid-gas systems; it exists for any combination of two phases and also in the case of two immiscible same-phase fluids. Its quantity depends on physical and chemical properties of the phases.

2.2. Equilibrium Contact Angle

Figure 2.1 depicts a three phase equilibrium system: a sessile liquid droplet on a horizontal solid substrate, surrounded by a gas. Circular edge of the droplet (represented by points A and B, since Figure 2.1 is a two-dimensional side-view) is a location where all three phases interact. This line is known as the *contact* or *triple line*. Coexistence of three phases at the contact line results in three surface tensions: σ_{ls} – between liquid and solid, σ_{gs} – between gas and solid, and σ_{gl} – between gas and liquid, which is, for the sake of clarity, further simply denoted as σ. The horizontal solid surface and the tangent of liquid-gas interface form the equilibrium contact angle θ_e.

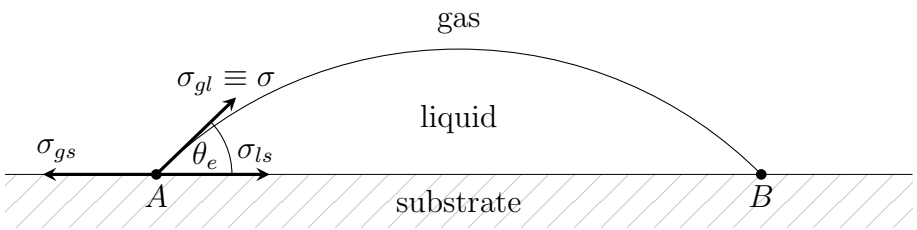

Figure 2.1: Force balance at the contact line

The balance of forces at the contact line leads to the Young equation [19]:

$$\sigma_{gs} = \sigma_{ls} + \sigma \cos\theta_e \,, \tag{2.1}$$

which defines the relationship between the three surface tensions and the contact angle.

As described in [18], wetting can be viewed as a direct consequence of the Young equation. Situation where the substrate is partially covered with liquid (as depicted in Figure 2.1 and on the left side of Figure 2.2) is called the *partial wetting state*. In partial wetting, a unique equilibrium contact angle exists for the given thermodynamic state and the gas-liquid-substrate combination. A change in any of the thermodynamic properties leads to a change in the three surface tensions along with the establishment of a new equilibrium contact angle, such that the balance of forces in equation (2.1) is satisfied.

For example, a change in temperature could lead to such a change in surface tensions that the surface tension at the gas-solid interface becomes equal to the sum of liquid-solid and gas-liquid surface tensions. In this case, the equilibrium contact angle reduces

to zero and the liquid forms a film which completely covers the substrate. This situation, depicted in the middle of Figure 2.2, is called the *complete wetting state*.

The opposite extreme situation, with an equilibrium contact angle of 180°, is called the *complete drying state*, depicted on the right in Figure 2.2. Here, by changing the temperature (or some other thermodynamic property), the sum of gas-solid and liquid-gas surface tensions becomes equal to the liquid-solid surface tension. Wetted area now becomes reduced to a point, leaving the substrate completely dry.

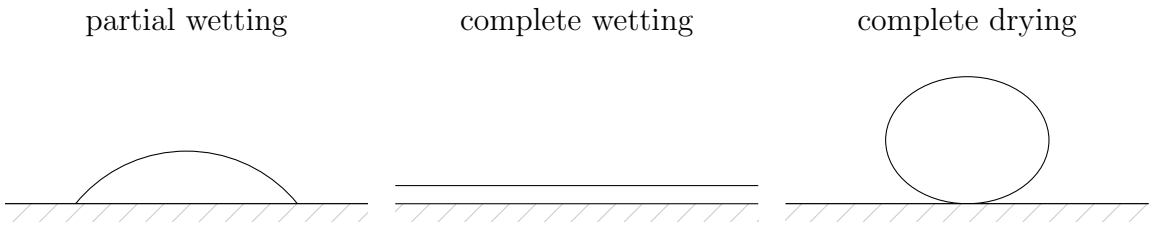

Figure 2.2: Wetting of a liquid droplet on a solid substrate

The equilibrium contact angle is uniquely defined for the thermodynamic state and the gas-liquid-solid combination. In the case of air-water combination (with constant thermodynamic properties of the system) material of substrate surface greatly affects the value of equilibrium contact angle. Substrate materials where $\theta_e < 90°$ promote wetting and are commonly referred to as *hydrophilic* (Figure 2.3, left). Analogously, materials where $\theta_e > 90°$ are called *hydrophobic* (Figure 2.3, right).

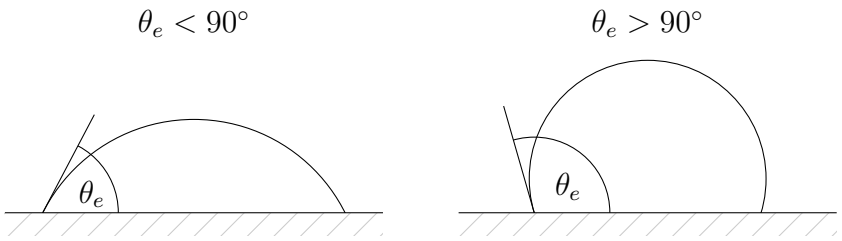

Figure 2.3: Hydrophilic and hydrophobic substrate

2.3. Advancing and Receding Contact Angle

As described in [20], the Young equation (2.1) gives only one equilibrium contact angle for a homogeneous pure liquid on a perfectly flat, rigid, and smooth substrate

without any impurity or heterogeneity. Since these conditions are practically unachievable, experimental measurements of the apparent contact angle differ from the analytical solutions. Due to substrate roughness and other causes of heterogeneity, several values of contact angles for a droplet in the state of static equilibrium can be experimentally observed. These values range from the receding contact angle θ_r to the advancing contact angle θ_a, with the equilibrium contact angle θ_e from (2.1) laying somewhere between these two extremes. Difference of advancing and receding contact angle is referred to as the *contact angle hysteresis* [21]:

$$\Delta\theta = \theta_a - \theta_r \, . \tag{2.2}$$

A direct consequence of the contact angle hysteresis can be seen in cases where a droplet remains immobile on an inclined surface (Figure 2.4). Only after the inclination angle reaches a critical value, will the droplet slide or roll-off the surface. So, if a horizontal substrate surface, where a sessile droplet is deposited, was slowly rotated, the contact line would not displace immediately. The effect of gravitational force would instead shift the droplet's centre of gravity initiating an internal flow field. Consequently, the contact angles would adjust while leaving the contact line attached to its original position.

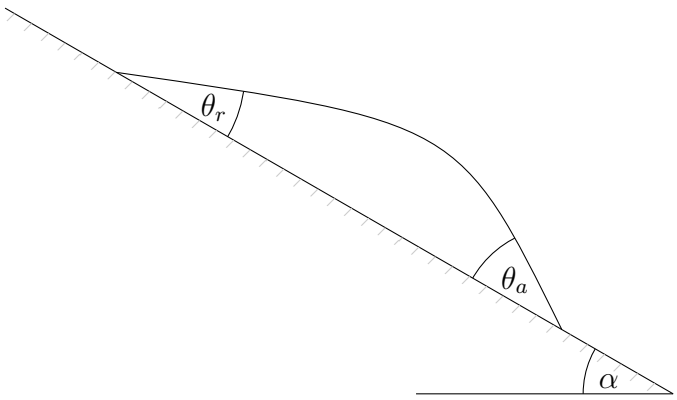

Figure 2.4: Droplet on an inclined substrate

This behaviour becomes obvious when the balance of forces along the inclined plane is observed. At the contact line, there are two forces counteracting the gravity: the adhesion force due to the hysteresis and the friction force due to the shear stress at the surface. Only when gravity overcomes the sum of aforementioned forces, contact angles reach out of the hysteresis band and the contact line becomes mobile.

For an idealised frictionless scenario, [22] proposes the following relation as a force balance at the contact line:

$$H = \sigma(\cos\theta_r - \cos\theta_a) = \frac{mg\sin\alpha}{w}\,. \tag{2.3}$$

Here, the hysteresis force per unit length is denoted as H and it is a function of the gas-liquid surface tension σ and the receding and advancing contact angles, respectively θ_r and θ_a. The gravity force per unit length is given by the right hand side of equation (2.3), where m is the mass of the droplet, g is the gravitational acceleration, w is the droplet's width and α is the minimum tilting angle to make the droplet slide. Therefore, the motion of a droplet is realised only when the gravitational force becomes greater than the hysteresis force which keeps the droplet pinned to the substrate.

Description of the hysteresis consequences clarifies the premise behind naming its extreme values. The advancing contact angle is determined for an increase in wetted area, where liquid is advancing across a dry substrate. This is seen in Figure 2.4, where the droplet advances downhill, wetting the previously dry area. Uphill, the opposite happens: the receding contact angle corresponds to a decrease in wetted area, where liquid retracts on a wet substrate. Another illustration of contact line motion is shown in Figure 2.5, where the left side depicts droplet spreading on a flat substrate (advancing motion) and the right side depicts droplet retracting (receding motion).

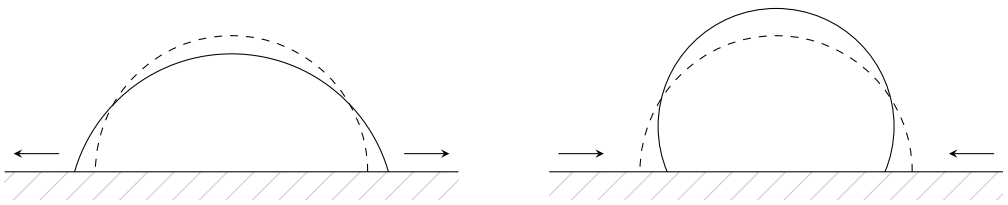

Figure 2.5: Advancing and receding motion of the contact line

2.4. Dynamic Contact Angle

The motion of contact line is possible only for contact angles beyond the hysteresis. The *dynamic contact angle*, which is observed on a mobile droplet, is a result of molecular interactions and its value is strongly linked to the microscopic landscape of the substrate. Since such a detailed description isn't possible within the scope of continuum

mechanics, the existing models for dynamic contact angles are mostly empirical and based on relations between the equilibrium contact angle θ_e and the capillary number Ca. One of those empirical models is that of Kistler [23]:

$$\theta_d = f_{\mathrm{H}}(\mathrm{Ca} + f_{\mathrm{H}}^{-1}(\theta_e)) \,, \tag{2.4}$$

which uses the Hoffman function defined as:

$$f_{\mathrm{H}} = \arccos\left\{1 - 2\tanh\left[5.16\Big[\frac{x}{1+1.13x^{0.99}}\Big]^{0.706}\right]\right\} . \tag{2.5}$$

The capillary number Ca in equation (2.4) is a dimensionless quantity which represents the ratio of viscous and surface tension forces, defined as:

$$\mathrm{Ca} = \frac{v\mu}{\sigma} \,, \tag{2.6}$$

with v being the magnitude of the characteristic velocity, μ the dynamic viscosity and σ the surface tension.

Another well known empirical model is the Hoffman-Voinov-Tanner law [24, 25, 26]:

$$\theta_d^3 - \theta_e^3 = c_T \mathrm{Ca}^{1/3} \,, \tag{2.7}$$

where c_T is a numerical constant dependent on the substrate-fluids combination. This model is valid only for surface tension dominated flows (Ca < 1), which presents an important restriction. The Hoffman-Voinov-Tanner law is a simplified version of what is often referred to as the Cox-Voinov model, defined in [27] as:

$$\theta_d^3 - \theta_m^3 = 9\mathrm{Ca}\ln\frac{x}{L_m} \,, \tag{2.8}$$

also valid only for flows with Ca < 1. In (2.8), θ_m is the microscopic contact angle, observable in the scale of surface roughness. This angle is often assumed to either have a constant value equal to the equilibrium contact angle θ_e or to change as a function of capillary number Ca. The dynamic contact angle θ_d is the one observable by the experiments. Quantity x is the distance from the contact line where the apparent (dynamic) contact angle is measured and L_m represents the microscopic length scale. Value of this parameter is typically in the range of 10 μm [28].

Conclusively, all dynamic contact angle models presented in this section are based on the hydrodynamic theory. Kistler's model (2.4) is the only one which isn't restricted

by the capillary number and for surface tension dominated flows (Ca $<$ 1) it reduces to the Hoffman-Voinov-Tanner law [27], which demonstrates the similarity between the models.

In literature, e.g. [29], contact angle models based on the molecular-kinetic theory can also be found. These models take into account the microscopic properties of the solid substrate and they relate the change of the contact angle to the displacement of molecules at the contact line. Due to the complexity of molecular-kinetic models, they weren't thoroughly investigated in this thesis.

Chapter 3.

Volume of Fluid

Volume of Fluid (VoF) is a mathematical model consisted of partial differential equations which describe the free surface flow. In order to differentiate between the phases, VoF method uses an indicator function, which is, from the numerical perspective, defined as a phase volume fraction. Mathematical formulation of the method, given in Section 3.1., is taken from [15].

To make the VoF method appropriate for computational handling, the mathematical model is discretised using the Finite Volume Method (FVM). The resulting numerical model, along with the discretisation procedure, is given in Section 3.2. All of the equations presented in aforesaid section are also taken from [15], unless otherwise noted.

According to the FVM principles, discretisation procedure is performed on the computational domain and on the partial differential equations. Computational domain is discretised spatially by splitting the flow domain into a finite number of non-overlapping control volumes or cells and temporally by splitting the time interval into a finite number of time steps of equal or varying duration. Final result of the discretisation procedure is a set of linear algebraic equations, which can be solved numerically.

3.1. Mathematical Model

3.1.1. General Transport Equation

Every fluid flow can be mathematically described using the transport equations of its conservative properties - namely mass, momentum and energy. For an arbitrary control

volume V, as depicted in Figure 3.1, the general form of transport equation for a flow quantity φ is the following:

$$\frac{d}{dt}\int_V \varphi dV + \oint_{\partial V} \mathbf{F}_C \cdot d\mathbf{S} - \oint_{\partial V} \mathbf{F}_D \cdot d\mathbf{S} = \int_V Q_V dV + \oint_{\partial V} \mathbf{Q}_S \cdot d\mathbf{S}\,, \tag{3.1}$$

where t is the time, $\mathbf{F}_C = \varphi\mathbf{v}$ is the flux over the boundary due to convection, $\mathbf{v}$ is the fluid velocity, $\mathbf{F}_D$ flux over the boundary due to diffusion, Q_V internal source, $\mathbf{Q}_S$ source at the boundary, ∂V boundary of the control volume V and $d\mathbf{S}$ outward pointing surface element vector. Flow quantity φ is completely generic and it could represent scalar, vector or a tensor field. Applying Gauss' theorem to equation (3.1) leads to:

$$\frac{d}{dt}\int_V \varphi dV + \int_V \nabla \cdot \mathbf{F}_C dV - \int_V \nabla \cdot \mathbf{F}_D dV = \int_V Q_V dV + \int_V \nabla \cdot \mathbf{Q}_S dV\,, \tag{3.2}$$

which represents the integral form of the transport equation, valid for an arbitrary control volume of a finite size. If the volume tends to a single point, transport equation (3.2) becomes reduced to its differential form:

$$\frac{\partial \varphi}{\partial t} + \nabla \cdot \mathbf{F}_C - \nabla \cdot \mathbf{F}_D = Q_V + \nabla \cdot \mathbf{Q}_S\,. \tag{3.3}$$

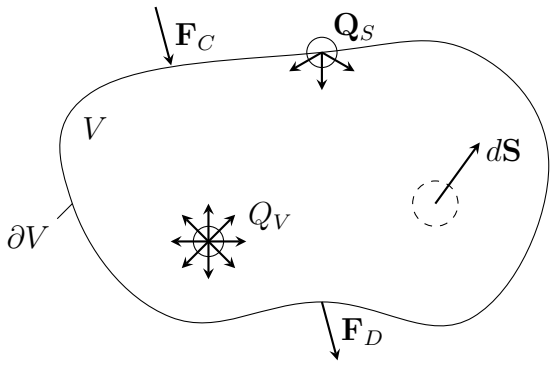

Figure 3.1: General form of the conservation law

3.1.2. Governing Equations

There are three conservation laws which govern any fluid flow: conservation of mass, conservation of momentum and conservation of energy. For a laminar incompressible isothermal flow of two immiscible fluids, only mass and momentum conservation have to be considered. However, there is a discontinuity in fluid properties at the interface region

which has to be specially treated. Thus, each fluid (phase) is tracked by a different value of an indicator function. The interface between the fluids is then implicitly defined as the region where the indicator function undergoes a step change.

Conservation laws are derived by substituting the generic flow quantity φ in equation (3.3) with the relevant flow property. The differential form of mass conservation is thus obtained by substituting φ with mass per unit volume, i.e. fluid density ρ:

$$\frac{\partial \rho}{\partial t} + \nabla \cdot \rho \mathbf{v} = 0 \,. \tag{3.4}$$

Equation (3.4) states that, under the assumption that there are no mass sources, the mass in a control volume can only be changed by flow across the boundaries.

Conservation of linear momentum is derived in a similar manner from equation (3.3). Here, the quantity φ is substituted by momentum per unit volume $\rho\mathbf{v}$. It is assumed that there is no momentum diffusion when the fluid is at rest: $\mathbf{F}_D = 0$. The source terms stem from surface and body forces acting upon the control volume. The only body force considered here is due to gravity: $\rho\mathbf{g}$, where $\mathbf{g}$ is the gravitational acceleration. Surface forces manifest themselves as stresses acting across the control volume boundary. The stress tensor $\boldsymbol{\sigma}$ for a Newtonian fluid in a local thermodynamic equilibrium is defined as:

$$\boldsymbol{\sigma} = -\Big(p + \frac{2}{3}\mu \nabla \cdot \mathbf{v}\Big)\mathbf{I} + \mu\Big(\nabla\mathbf{v} + (\nabla\mathbf{v})^{\mathrm{T}}\Big) \,, \tag{3.5}$$

where p is pressure, μ dynamic viscosity and $\mathbf{I}$ unit tensor.

For a two-phase flow, there is an additional internal force due to surface tension, denoted as $\mathbf{f}_\sigma$, acting upon the interface region. Therefore, the transport equation for linear momentum is the following:

$$\frac{\partial(\rho\mathbf{v})}{\partial t} + \nabla \cdot (\rho\mathbf{v}\mathbf{v} - \boldsymbol{\sigma}) = \rho\mathbf{g} + \mathbf{f}_\sigma \,. \tag{3.6}$$

Conservation equations (3.4) and (3.6) treat the two immiscible fluids as a continuum, which means that density ρ and dynamic viscosity μ are defined as weighted averages of the two-phase system:

$$\rho = \alpha\rho_1 + (1-\alpha)\rho_2 \,, \tag{3.7}$$

$$\mu = \alpha\mu_1 + (1-\alpha)\mu_2 \,. \tag{3.8}$$

Subscripts 1 and 2 denote different fluids and $\alpha = \alpha(x,t)$ is the indicator function defined as:

$$\alpha(x,t) = \begin{cases} 1, & \text{for the point } (x,t) \text{ inside fluid 1} \\ 0, & \text{for the point } (x,t) \text{ inside fluid 2} \end{cases} . \tag{3.9}$$

The indicator function associates different values with different fluids. As defined in (3.9), it is a step function, implying discontinuous change of density and viscosity in the interface region. To allow treatment of a two-phase system as a continuum, a transitional area of small finite thickness δ is introduced, where function $\alpha(x,t)$ experiences a smooth change in its value:

$$\alpha(x,t) = \begin{cases} 1, & \text{for the point } (x,t) \text{ inside fluid 1} \\ 0, & \text{for the point } (x,t) \text{ inside fluid 2} \\ 0 < \alpha_\delta < 1, & \text{for the point } (x,t) \text{ inside transitional area} \end{cases} . \tag{3.10}$$

Value of $\alpha(x,0)$ is given by the initial fluid distribution. Further propagation of α in space and time is described by the phase mass conservation equation:

$$\frac{D\alpha}{Dt} = \frac{\partial \alpha}{\partial t} + \mathbf{v} \cdot \nabla \alpha = 0 \, . \tag{3.11}$$

Equation (3.11) completes the mathematical description of a laminar two-phase flow.

In order to make the mathematical model more suitable for numerical solution, first the continuity equation (3.4) is rewritten as:

$$\frac{\partial \rho}{\partial t} + \mathbf{v} \cdot \nabla \rho + \rho \nabla \cdot \mathbf{v} = 0 \, . \tag{3.12}$$

By rearranging the terms in equation (3.12), the divergence of velocity can be expressed as:

$$\nabla \cdot \mathbf{v} = \frac{-1}{\rho} \Big(\frac{\partial \rho}{\partial t} + \mathbf{v} \cdot \nabla \rho \Big) = \frac{-1}{\rho} \frac{D\rho}{Dt} = -\frac{D(\ln \rho)}{Dt} \, . \tag{3.13}$$

For incompressible fluids, the material derivative of density, $\frac{D\rho}{Dt}$, reduces to zero. In the case of a two-phase flow, this can be proved by using the definition of average density ρ from (3.7) and then applying the relation (3.11) to the indicator function material derivative:

$$\nabla \cdot \mathbf{v} = \frac{-1}{\rho} \frac{D}{Dt} \big(\alpha(\rho_1 - \rho_2) + \rho_2 \big) = \frac{-(\rho_1 - \rho_2)}{\rho} \left(\frac{D\alpha}{Dt} \right) = 0 \, , \tag{3.14}$$

which represents the continuity equation for incompressible fluids. Using the incompressibility condition (3.14) allows the transport equation for α (3.11) to be written in its conservative form:

$$\frac{\partial \alpha}{\partial t} + \nabla \cdot (\alpha \mathbf{v}) = 0 \,. \tag{3.15}$$

Applying the incompressibility condition (3.14) to the momentum equation (3.6) reduces it to the following:

$$\frac{\partial (\rho \mathbf{v})}{\partial t} + \nabla \cdot (\rho \mathbf{v}\mathbf{v}) - \nabla \cdot (\mu \nabla \mathbf{v}) = -\nabla p + \rho \mathbf{g} + \mathbf{f}_\sigma + (\nabla \mathbf{v}) \cdot (\nabla \mu) \,. \tag{3.16}$$

Finally, the set of governing equations for a two-phase consists of the continuity equation (3.14):

$$\nabla \cdot \mathbf{v} = \frac{-1}{\rho} \frac{D}{Dt} \big(\alpha(\rho_1 - \rho_2) + \rho_2 \big) = \frac{-(\rho_1 - \rho_2)}{\rho} \left(\frac{D\alpha}{Dt} \right) = 0 \,,$$

the momentum equation (3.16):

$$\frac{\partial (\rho \mathbf{v})}{\partial t} + \nabla \cdot (\rho \mathbf{v}\mathbf{v}) - \nabla \cdot (\mu \nabla \mathbf{v}) = -\nabla p + \rho \mathbf{g} + \mathbf{f}_\sigma + (\nabla \mathbf{v}) \cdot (\nabla \mu) \,,$$

and the indicator function transport equation (3.15):

$$\frac{\partial \alpha}{\partial t} + \nabla \cdot (\alpha \mathbf{v}) = 0 \,,$$

along with the two constitutive relations for fluid density (3.7):

$$\rho = \alpha \rho_1 + (1 - \alpha) \rho_2 \,,$$

and dynamic viscosity (3.8):

$$\mu = \alpha \mu_1 + (1 - \alpha) \mu_2 \,.$$

The momentum equation (3.16) has an internal force due to surface tension $\mathbf{f}_\sigma$, which is described in the following section.

3.1.3. Surface Tension

The momentum equation (3.16) features an internal force due to surface tension, which manifests itself as a tension acting upon the interface. This tensile force is tangential to the interface and separates the two fluids of diverse densities. If the interface

is curved, there is also a normal component of this force (Figure 3.2). When the fluids are in the state of static equilibrium, the normal component of surface tension is mechanically balanced by the pressure jump across the interface.

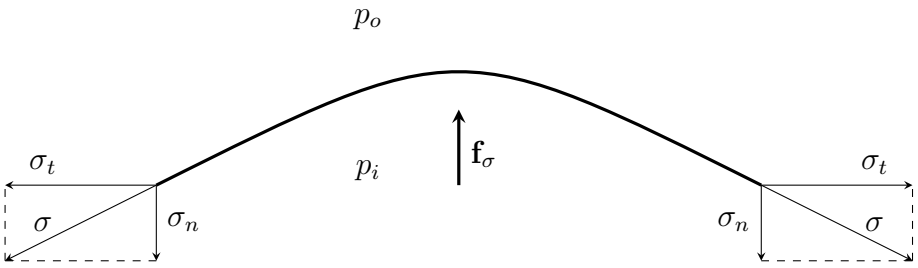

Figure 3.2: Forces on a curved interface

The pressure jump across the interface Δp is proportional to the mean interface curvature κ:

$$\Delta p = p_i - p_o = \sigma\left(\frac{1}{R_1} + \frac{1}{R_2}\right) = \sigma\kappa\,, \tag{3.17}$$

In the equation above, p_i is the higher pressure, present on the concave side of the curved free surface. Analogously, p_o is the lower pressure, on the convex side of the free surface. Quantities R_1 and R_2 denote the principal radii of the curvature.

Surface tension force $\mathbf{f}_\sigma$ is a function of the pressure jump, as defined in (3.17). To include this force into the momentum equation (3.16), it has to be expressed as a pressure gradient $\mathbf{f}_\sigma = \nabla p$. This formulation would make the force differentiable across the whole domain, hence allowing a description in accordance with the continuum mechanics principles. However, the force acts only in the transitional interface area, so it has to be expressed as a function which is equal to zero everywhere else in the domain. Another difficulty arises from the fact that the pressure jump is discontinuous at the transitional area.

Formulation which overcomes the aforementioned issues is called the *Continuum Surface Force* (CSF) model, developed by [30]. This model relates the unit normal vector to the interface, $\mathbf{n}_I$, with the gradient of the indicator function α:

$$\mathbf{n}_I = \frac{\nabla\alpha}{|\nabla\alpha|}\,. \tag{3.18}$$

Since the indicator function experiences a change only in the transitional area between the two fluids, its gradient reduces to zero in the rest of the domain. This property

makes the interface normal $\mathbf{n}_I$ continuous throughout the entirety of the flow domain. The mean interface curvature κ can now be expressed as a function of $\mathbf{n}_I$:

$$\kappa = -\nabla \cdot \left(\frac{\nabla \alpha}{|\nabla \alpha|} \right). \tag{3.19}$$

The pressure jump Δp is a discontinuity which occurs at the interface layer. As described in the previous section, this layer is defined as an area of finite thickness δ, throughout which the indicator function α experiences a smooth change. Therefore, it is reasonable to assume that the change in pressure would behave similarly. In other words, pressure gradient in the transitional area can be expressed as proportional to the indicator function gradient. This leads to the definition of the surface tension force $\mathbf{f}_\sigma$, in accordance with the CSF model:

$$\mathbf{f}_\sigma = \nabla p = -\sigma \left(\nabla \cdot \left(\frac{\nabla \alpha}{|\nabla \alpha|} \right) \right) (\nabla \alpha). \tag{3.20}$$

By substituting the relation (3.20) into the momentum equation (3.16), the set of governing equations becomes fully defined. In order to complete the mathematical model, the initial and boundary conditions have to be specified.

The adhesion forces which arise at the contact line weren't yet addressed. Since these forces act only where the two fluids come in contact with the solid boundary, this behaviour is defined within the boundary conditions and will be discussed in Chapter 5.

3.2. Numerical Model

The derivation of numerical model given in this section is taken from [15]. Discretisation procedure follows the Finite Volume Method, described in detail in [31, 32].

3.2.1. Spatial Discretisation

In order to spatially discretise the model, the entire flow domain is split into a finite number of non-overlapping control volumes or cells. Control volumes may have an arbitrary number of flat faces, as depicted in Figure 3.3. The computational point P is located at the centroid of the control volume and vector $\mathbf{d} = \overline{PN}$ connects it to the

centroid of the neighbouring control volume, denoted with N. Vector $\mathbf{A}$ is the face area vector, outward pointing and normal to the face. If there is a non-zero angle between vectors $\mathbf{d}$ and $\mathbf{A}$, the control volume is non-orthogonal. In that case, the contributions to gradients at cell faces are split into orthogonal and non-orthogonal contributions. Vector $\mathbf{D}$ is introduced to account for orthogonal contributions:

$$\mathbf{D} = \frac{\mathbf{d}}{\mathbf{d} \cdot \mathbf{A}} |\mathbf{A}|^2 \,, \tag{3.21}$$

and vector $\mathbf{k}$ for non-orthogonality:

$$\mathbf{k} = \mathbf{A} - \mathbf{D} \,. \tag{3.22}$$

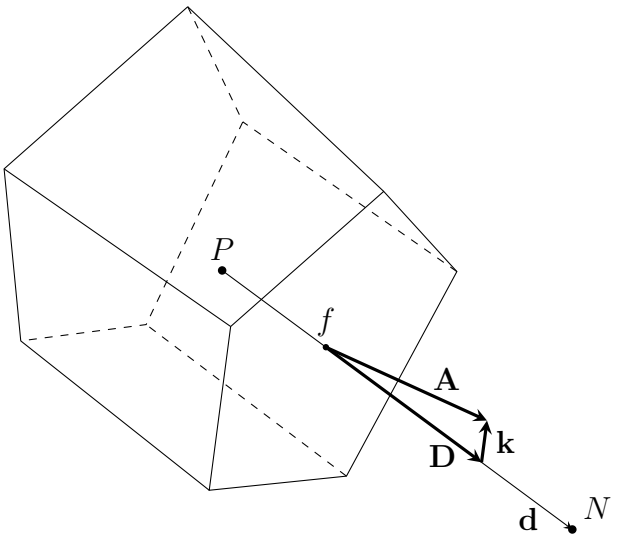

Figure 3.3: Geometric quantities of a control volume

3.2.2. Discrete Equations

To discretise the partial differential equations, first the volume integrals have to be represented as surface integrals. For that a generalized form of Gauss' theorem is used. Gauss' theorem applied to divergence of an arbitrary vector function $\boldsymbol{\varphi}$ is the following:

$$\int_V \nabla \cdot \boldsymbol{\varphi} dV = \oint_{\partial V} d\mathbf{S} \cdot \boldsymbol{\varphi} \,. \tag{3.23}$$

The same theorem applied to gradient of an arbitrary scalar function φ leads to this relation:

$$\int_V \nabla\varphi dV = \oint_{\partial V} d\mathbf{S}\varphi \,. \tag{3.24}$$

Similarly, for gradient of an arbitrary vector function $\boldsymbol{\varphi}$, Gauss' theorem reads as:

$$\int_V \nabla\boldsymbol{\varphi} dV = \oint_{\partial V} d\mathbf{S}\boldsymbol{\varphi} \,. \tag{3.25}$$

In above equations, $d\mathbf{S}$ is the surface area vector and ∂V is the surface area of the control volume. Since the control volumes are bound by a finite number of flat faces, the surface integrals can be approximated as sums of face integrals. Thus equation (3.23) can be written as:

$$\int_V \nabla\cdot\boldsymbol{\varphi} dV = \oint_{\partial V} d\mathbf{S}\cdot\boldsymbol{\varphi} = \sum_{f=1}^{n}\left(\int_f d\mathbf{S}\cdot\boldsymbol{\varphi}\right) \approx \sum_{f=1}^{n}\mathbf{A}_f\cdot\boldsymbol{\varphi}_f \,, \tag{3.26}$$

where f denotes the face centroid, $\mathbf{A}_f$ is the face area vector and n is the number of flat faces of the control volume. Every face (except those at the boundaries of the domain) is shared by two cells. One of those cells is the owner with face area vector $\mathbf{A}_f$ pointing towards the other, neighbouring cell. Thus, the sum in equation (3.26) is split into sum over owner faces and sum over neighbouring faces:

$$\sum_{f=1}^{n}\mathbf{A}_f\cdot\boldsymbol{\varphi}_f = \sum_{\substack{owner\\faces}}\mathbf{A}_f\cdot\boldsymbol{\varphi}_f + \sum_{\substack{neighbouring\\faces}}\mathbf{A}_f\cdot\boldsymbol{\varphi}_f \,. \tag{3.27}$$

The face values are (unless otherwise stated) linearly interpolated from cell-centred values:

$$\boldsymbol{\varphi}_f = \mathcal{L}_P\boldsymbol{\varphi}_P + (1-\mathcal{L}_P)\boldsymbol{\varphi}_N \,, \tag{3.28}$$

where $\mathcal{L}_P$ is the interpolation factor defined as ratio of distance $|\overline{fN}|$ between face center f and neighbour cell centroid N, and distance $|\overline{PN}|$ between computational point P and neighbour cell centroid N:

$$\mathcal{L}_P = \frac{|\overline{fN}|}{|\overline{PN}|} \,. \tag{3.29}$$

Similarly, equations (3.24) and (3.25) can be transformed into:

$$\int_V \nabla\varphi dV \approx \sum_{f=1}^{n}\mathbf{A}_f\varphi_f \,, \tag{3.30}$$

and

$$\int_V \nabla \boldsymbol{\varphi} dV \approx \sum_{f=1}^{n} \mathbf{A}_f \boldsymbol{\varphi}_f \,. \tag{3.31}$$

Finally, the equations (3.26), (3.30) and (3.31) can be used to express the gradient of a flow property over a cell:

$$(\nabla \cdot \boldsymbol{\varphi})_P \approx \frac{1}{V_P} \sum_{f=1}^{n} \mathbf{A}_f \cdot \boldsymbol{\varphi} \,, \tag{3.32}$$

$$(\nabla \varphi)_P \approx \frac{1}{V_P} \sum_{f=1}^{n} \mathbf{A}_f \varphi \,, \tag{3.33}$$

$$(\nabla \boldsymbol{\varphi})_P \approx \frac{1}{V_P} \sum_{f=1}^{n} \mathbf{A}_f \boldsymbol{\varphi} \,. \tag{3.34}$$

3.2.3. Indicator Function

On a discrete mesh, the indicator function α is defined as a volume fraction of fluid which occupies the cell:

$$\alpha_P = \frac{\text{Volume of fluid 1}}{\text{Total volume of the control volume}} \,. \tag{3.35}$$

The above definition of indicator function α is in accordance with definition (3.10). Thus, $\alpha_P = 1$ indicates that the cell volume is completely filled with fluid 1. Accordingly, $\alpha_P = 0$ indicates that there is none of the fluid 1 in the cell, i.e. the cell is completely occupied with fluid 2. Finally, if $0 < \alpha_P < 1$, the cell is partially filled with fluid 1, which indicates existence of interface between the fluids in the cell.

The integral form of indicator function transport equation (3.15) is the following:

$$\int_t^{t+\delta t} \left(\int_V \frac{\partial \alpha}{\partial t} dV \right) dt + \int_t^{t+\delta t} \left(\int_V \nabla \cdot \alpha \mathbf{v} dV \right) dt = 0 \,. \tag{3.36}$$

Discretisation of the equation above is done by splitting the values at the new time level (denoted by superscript n) from the ones evaluated at the old time-level (superscript o) and writing the latter into the source term. Thus, fully discretised form of equation (3.36) is:

$$\alpha_P^n \frac{V_P}{\Delta t} + \sum_{f=1}^{n} \frac{1}{2} (\alpha \mathbf{F})_f^n = S_{\alpha_P} \,, \tag{3.37}$$

with source term S_{α_P} defined as:

$$S_{\alpha_P} = \alpha_P^o \frac{V_P}{\Delta t} - \sum_{f=1}^{n} \frac{1}{2}(\alpha \mathbf{F})_f^o \, . \tag{3.38}$$

In equations (3.37) and (3.38), V_P is the volume of the cell, Δt is the duration of the time-step between new and old time instance and $\mathbf{F}_f$ is the volumetric flux defined as:

$$\mathbf{F}_f = \mathbf{A}_f \cdot \mathbf{v}_f \, , \tag{3.39}$$

where $\mathbf{A}_f$ is the face area vector and $\mathbf{v}_f$ is the face-centred value of velocity. Discretisation of convective term from equation (3.36) is done by first applying Gauss' theorem (3.32) in order to represent it as a sum over faces. Temporal discretisation is done by using the second order accurate Cranck-Nicolson scheme. Face-centred values of the indicator function α_f are interpolated from cell-centred values of neighbouring cells:

$$\alpha_f = \beta \alpha_P + (1 - \beta)\alpha_N \, , \tag{3.40}$$

with β being the weighting factor. Relation (3.40) allows equation (3.37) to be reformulated in terms of cell and its nearest neighbours:

$$a_P \alpha_P^n = \sum_{nb=1}^{n} a_{nb} \alpha_{nb}^n + S_{\alpha_P} \, , \tag{3.41}$$

where subscript nb denotes the nearest neighbours. Equation (3.41) is linear algebraic with diagonal coefficient a_P and neighbouring coefficients a_{nb}.

3.2.4. Momentum Equation

The integral form of the momentum conservation equation (3.16) is the following:

$$\begin{aligned} \int_t^{t+\delta t} \left(\int_V \frac{\partial \rho \mathbf{v}}{\partial t} dV \right) dt + \int_t^{t+\delta t} \left(\int_V \nabla \cdot (\rho \mathbf{v}\mathbf{v}) dV \right) dt - \int_t^{t+\delta t} \left(\int_V \nabla \cdot (\mu \nabla \mathbf{v}) dV \right) dt \\ = - \int_t^{t+\delta t} \left(\int_V \nabla p dV \right) dt + \int_t^{t+\delta t} \left(\int_V \rho \mathbf{g} dV \right) dt \\ + \int_t^{t+\delta t} \left(\int_V \sigma \kappa \nabla \alpha dV \right) dt + \int_t^{t+\delta t} \left(\int_V (\nabla \mathbf{v}) \cdot (\nabla \mu) dV \right) dt \, . \end{aligned} \tag{3.42}$$

Integrating the above equation over the control volume leads to its partially disecretised form:

$$\int_t^{t+\delta t} \left(\left(\frac{\partial \rho \mathbf{v}}{\partial t} \right)_P V_P + \sum_{f=1}^{n} \rho_f \mathbf{F}_f \mathbf{v}_f - \sum_{f=1}^{n} \mu_f \mathbf{A}_f (\nabla \mathbf{v})_f \right) dt = \int_t^{t+\delta t} (S_{\mathbf{v}_P} V_P) dt \,, \quad (3.43)$$

with the source term $S_{\mathbf{v}_P}$ defined as:

$$S_{\mathbf{v}_P} = -(\nabla p)_P + \mathbf{g}\rho_P + \sigma \kappa_P (\nabla \alpha)_P + (\nabla \mathbf{v})_P \cdot (\nabla \mu)_P \,. \quad (3.44)$$

Discretisation procedure follows a similar routine as described in the previous section. The main difference stems from the fact that the momentum equation (3.42) is conservation of a vector quantity, thus volume integrals are approximated as sums of face integrals using Gauss' theorem in forms (3.32) and (3.34). Terms of interest in equations (3.43) and (3.44) are the convection term, the diffusion term and the curvature term κ_P. Important issues during the discretisation are prediction of the face values from cell centred values of two cells sharing the face, treatment of the mesh non-orthogonality and keeping the consistency in the discretisation.

Convection Term

The partially discretised convection term takes this form:

$$\int_V \nabla \cdot (\rho \mathbf{v} \mathbf{v}) dV \approx \sum_{f=1}^{n} \rho_f \mathbf{F}_f \mathbf{v}_f \,, \quad (3.45)$$

where $\mathbf{F}_f$ is the volumetric flux defined in (3.39). Product $\rho_f \mathbf{F}_f$ represents the mass flux through face, thus the approximation of densities has to be done in such a way that the mass is also conserved. Face values of density are approximated using the old time-level and new time-level face values of the indicator function α, combined with the constitutive relation for density (3.7):

$$\rho_f = \frac{1}{2}(\alpha_f^o + \alpha_f^n)\rho_1 + \left(1 - \frac{1}{2}(\alpha_f^o + \alpha_f^n)\right)\rho_2 \,. \quad (3.46)$$

The definition of face densities above guarantees conservative mass fluxes at the faces.

Approximation of face-centred velocity requires accurate and bounded differencing scheme. Upwind differencing scheme complies with the boundedness criteria, but introduces large amount of numerical diffusion. Central differencing scheme produces more

accurate solution, but doesn't comply with the boundedness criteria. Thus, for predicting the face values of velocity a specially developed High Resolution differencing scheme is used [33].

Diffusion Term

Partially discretised diffusion term takes the following form:

$$\int_V \nabla \cdot (\mu \nabla \mathbf{v}) dV \approx \sum_{f=1}^{n} \mu_f \mathbf{A}_f (\nabla \mathbf{v})_f \, . \tag{3.47}$$

Face value of dynamic viscosity μ_f is linearly interpolated using equation (3.28). Same equation is also applied to face value of velocity gradient $(\nabla \mathbf{v})_f$.

Calculation of dot-product $\mathbf{A}_f \cdot (\nabla \mathbf{v})_f$ differs for orthogonal and non-orthogonal meshes. For an orthogonal mesh, the face area vector $\mathbf{A}_f$ is equal to vector $\mathbf{D}_f$, defined in equation (3.21). In that case, the dot-product is the following:

$$\mathbf{A}_f \cdot (\nabla \mathbf{v})_f = \mathbf{D}_f \cdot (\nabla \mathbf{v})_f = |\mathbf{D}_f| \frac{\mathbf{v}_N - \mathbf{v}_P}{|\mathbf{d}_f|} \, . \tag{3.48}$$

For a non-orthogonal mesh, it is necessary to include the non-orthogonal correction $\mathbf{k}_f$, defined in (3.22). Thus, the dot-product is the following:

$$\mathbf{A}_f \cdot (\nabla \mathbf{v})_f = \underbrace{\mathbf{D}_f \cdot (\nabla \mathbf{v})_f}_{orthogonal\ contribution} + \underbrace{\mathbf{k}_f \cdot (\nabla \mathbf{v})_f}_{non-orthogonal\ correction} \, , \tag{3.49}$$

with the orthogonal contribution $\mathbf{D}_f \cdot (\nabla \mathbf{v})_f$ calculated as in (3.48).

Curvature

In the momentum equation (3.42), the term containing the free surface curvature κ is discretised in the following way:

$$\int_V \sigma \kappa \nabla \alpha dV = \sigma \kappa_P (\nabla \alpha)_P V_P \, . \tag{3.50}$$

In the equation above the cell-centred gradient of the indicator function $(\nabla \alpha)_P$ is calculated using the Gauss' theorem (3.33) with linearly interpolated face value α_f according to equation (3.28).

The free surface curvature is defined in equation (3.19) as a divergence of unit normal to the interface $\mathbf{n}_I$. The unit normal $\mathbf{n}_I$ is expressed using the gradient of the indicator

function α in (3.18). Using Gauss' theorem for divergence of a vector quantity (3.32), the cell-centred value of curvature is the following:

$$\kappa_P = -\left(\nabla \cdot \left(\frac{\nabla\alpha}{|\nabla\alpha|}\right)\right)_P = \frac{1}{V_P}\sum_{f=1}^{n} \mathbf{A}_f \cdot \left(\frac{(\nabla\alpha)_f}{|\nabla\alpha|_f}\right). \tag{3.51}$$

Here, the face value $(\nabla\alpha)_f$ is obtained using linear interpolation (3.28), with cell-centred gradient $(\nabla\alpha)_P$ calculated as described.

Temporal Discretisation

Temporal discretisation of the momentum equation (3.43) is done in a manner similar to temporal discretisation of the indicator function α. New time-level values are separated from the old time-level values, with the latter added into the source term. Using the Euler implicit time differencing scheme yields this form of fully discretised momentum equation:

$$\frac{(\rho\mathbf{v})_P^n}{\Delta t} + \frac{1}{V_P}\sum_{f=1}^{n} \rho_f \mathbf{F}_f \mathbf{v}_f^n + \frac{1}{V_P}\sum_{f=1}^{n} \mu_f \mathbf{D}_f \cdot (\nabla\mathbf{v})_f^n = S_{\mathbf{v}_P} - (\nabla p)_P\,, \tag{3.52}$$

with the source term $S_{\mathbf{v}_P}$ defined as:

$$S_{\mathbf{v}_P} = \frac{(\rho\mathbf{v})_P^o}{\Delta t} + \mathbf{g}\rho_P + \sigma\kappa_P(\nabla\alpha)_P + (\nabla\mathbf{v})_P \cdot (\nabla\mu)_P + \sum_{f=1}^{n} \mu_f \mathbf{k}_f \cdot (\nabla\mathbf{v})_f\,. \tag{3.53}$$

Since all face velocities at the right hand side of equation (3.52) are dependent only on cell-centred values of the cell and its nearest neighbours, the equation can be reformulated to:

$$a_P\mathbf{v}_P^n = \sum_{nb=1}^{n} a_{nb}\mathbf{v}_{nb}^n + S_{\mathbf{v}_P} - (\nabla p)_P\,, \tag{3.54}$$

where subscript nb denotes the nearest neighbours. For derivation of the pressure equation, it is useful to reformulate the equation above into:

$$\mathbf{v}_P^n = \frac{\mathbf{H}(\mathbf{v})_P}{a_P} - \frac{1}{a_P}(\nabla p)_P\,, \tag{3.55}$$

where $\mathbf{H}(\mathbf{v})_P$ is defined as:

$$\mathbf{H}(\mathbf{v})_P = \sum_{nb=1}^{n} a_{nb}\mathbf{v}_{nb}^n + S_{\mathbf{v}_P}\,. \tag{3.56}$$

3.2.5. Pressure Equation

The pressure equation is derived from the incompressibility condition (3.14) and from the momentum equation (3.55). Integral form of the incompressibility equation (3.14) is spatially discretised using Gauss' theorem (3.26):

$$\oint_V \nabla \cdot \mathbf{v} dV \approx \sum_{f=1}^{n} \mathbf{A}_f \cdot \mathbf{v}_f = 0 \,, \tag{3.57}$$

with new time-level velocities.

The new time-level face value of velocity is expressed from the momentum equation (3.55) by interpolating it to the face:

$$\mathbf{v}_f = \left(\frac{\mathbf{H}(\mathbf{v})}{a_P}\right)_f - \left(\frac{1}{a_P}\right)_f (\nabla p)_f \,. \tag{3.58}$$

All face values in the above equation except the pressure gradient, i.e. $\left(\frac{\mathbf{H}(\mathbf{v})}{a_P}\right)_f$ and $\left(\frac{1}{a_P}\right)_f$, are calculated using linear interpolation (3.28). Substitution of $\mathbf{v}_f$ from (3.58) into (3.57) yields:

$$\sum_{f=1}^{n} \left(\frac{1}{a_P}\right)_f \mathbf{A}_f \cdot (\nabla p)_f = \sum_{f=1}^{n} \mathbf{A}_f \cdot \left(\frac{\mathbf{H}(\mathbf{v})}{a_P}\right)_f \,. \tag{3.59}$$

For the face value of pressure gradient $(\nabla p)_f$ it is necessary to include orthogonal and non-orthogonal contribution:

$$\mathbf{A}_f \cdot (\nabla p)_f = \underbrace{\mathbf{D}_f \cdot (\nabla p)_f}_{orthogonal\ contribution} + \underbrace{\mathbf{k}_f \cdot (\nabla p)_f}_{non-orthogonal\ correction} \,, \tag{3.60}$$

with the orthogonal contribution defined as:

$$\mathbf{D}_f \cdot (\nabla p)_f = |\mathbf{D}_f| \frac{p_N - p_P}{|\mathbf{d}_f|} \,, \tag{3.61}$$

and the non-orthogonal correction given by:

$$\mathbf{k}_f \cdot (\nabla p)_f = \mathbf{k}_f \cdot \left(\mathcal{L}_P \left(\frac{1}{V_P} \sum_{f=1}^{n} \mathbf{A}_f p_f \right)_P + (1 - \mathcal{L}_P) \left(\frac{1}{V_P} \sum_{f=1}^{n} \mathbf{A}_f p_f \right)_N \right) . \tag{3.62}$$

This non-orthogonal correction is added into the source term in equation (3.59):

$$\sum_{f=1}^{n} \left(\frac{1}{a_P}\right)_f \mathbf{D}_f \cdot (\nabla p)_f = S_P \,, \tag{3.63}$$

with the source term S_P defined as:

$$S_P = \sum_{f=1}^{n} \mathbf{A}_f \cdot \left(\frac{\mathbf{H}(\mathbf{v})}{a_P} \right)_f - \sum_{f=1}^{n} \left(\frac{1}{a_P} \right)_f \mathbf{k}_f \cdot (\nabla p)_f \, . \tag{3.64}$$

Since the pressure in equation (3.63) is given in terms of a cell and its nearest neighbours, it is possible to reformulate the equation to the following:

$$a_P p_P = \sum_{nb=1}^{n} a_{nb} p_{nb} + S_P \, , \tag{3.65}$$

where nb represents the nearest neighbours.

The face velocity from (3.58) is used for calculation of volumetric fluxes in (3.39):

$$\mathbf{F}_f = \mathbf{A}_f \cdot \left(\left(\frac{\mathbf{H}(\mathbf{v})}{a_P} \right)_f - \left(\frac{1}{a_P} \right)_f (\nabla p)_f \right) . \tag{3.66}$$

3.2.6. Boundary Conditions

The two most widely used boundary conditions are the Dirichlet and the Neumann boundary conditions (BC). The former is also known as value specified with this mathematical formulation given by [34]:

$$\varphi_b = \varphi_{ref} \, , \tag{3.67}$$

where φ_b is a generic physical quantity at the boundary denoted with subscript b and φ_{ref} is the known prescribed value of the regarded quantity φ.

In cases where value is unknown, but flux is known, the Neumann BC is used. In [34], the Neumann or flux specified BC is mathematically written as:

$$\mathbf{F}_b^{\varphi} \mathbf{S}_b = \underbrace{\mathbf{F}_b^{\varphi} \cdot \mathbf{n}_b}_{specified \ \ flux} S_b = q_{ref} S_b \, , \tag{3.68}$$

where $\mathbf{F}_b^{\varphi}$ denotes the flux of generic quantity φ at the boundary b with surface area vector $\mathbf{S}_b$, of magnitude S_b and unit outward pointing normal vector $\mathbf{n}_b$. Quantity q_{ref} represents the known flux per unit area.

Since the flux is associated with gradient of the regarded physical quantity, equation (3.68) can be rewritten as:

$$(\nabla \varphi)_b \cdot \mathbf{n}_b = q_{ref} \, . \tag{3.69}$$

In some cases a combination of both aforesaid BCs is needed. This type of boundary condition is known as mixed or Robin BC with this mathematical formulation (given for example in [27]):

$$\varphi_b = w\varphi_{ref} + (1-w)(\varphi_P + (\nabla\varphi)_{ref} \cdot \mathbf{\Delta}) \,. \tag{3.70}$$

In the equation above w represents the weighting factor between the boundary condition types, φ_P is the cell centred value of the regarded quantity and $\mathbf{\Delta}$ is the face-to-cell distance.

3.2.7. Solution Procedure

The discretisation procedure results in a set of linear algebraic equations which are strongly coupled with each other. The pressure-velocity coupling is satisfied by using the PISO (Pressure Implicit with Splitting of Operators) algorithm which is described first. Then, full solution procedure for a two-phase system is given.

PISO Algorithm

The PISO algorithm consists of the following steps:

1. **Momentum Prediction**: solve (3.54):

$$a_P \mathbf{v}_P^n = \sum_{nb=1}^{n} a_{nb}\mathbf{v}_{nb}^n + S_{\mathbf{v}_P} - (\nabla p)_P$$

   with a guessed pressure filed p^* (usually from the previous time step) to get the velocity field $\mathbf{v}^*$;

2. **Pressure Solution**: use $\mathbf{v}^*$ to assemble $\mathbf{H}(\mathbf{v}^*)$ from (3.56):

$$\mathbf{H}(\mathbf{v})_P = \sum_{nb=1}^{n} a_{nb}\mathbf{v}_{nb}^n + S_{\mathbf{v}_P}$$

   to calculate the pressure field p^{**} using (3.65):

$$a_P p_P = \sum_{nb=1}^{n} a_{nb} p_{nb} + S_P \,.$$

   For a non-orthogonal mesh update the source term from (3.64):

$$S_P = \sum_{f=1}^{n} \mathbf{A}_f \cdot \left(\frac{\mathbf{H}(\mathbf{v})}{a_P}\right)_f - \sum_{f=1}^{n} \left(\frac{1}{a_P}\right)_f \mathbf{k}_f \cdot (\nabla p)_f \,;$$

3. **Explicit Velocity Correction**: use the new pressure field p^{**} in equation (3.66):

$$\mathbf{F}_f = \mathbf{A}_f \cdot \left(\left(\frac{\mathbf{H}(\mathbf{v})}{a_P} \right)_f - \left(\frac{1}{a_P} \right)_f (\nabla p)_f \right)$$

for a new set of conservative volumetric fluxes. With the new pressure field p^{**} solve (3.55):

$$\mathbf{v}_P^n = \frac{\mathbf{H}(\mathbf{v})_P}{a_P} - \frac{1}{a_P}(\nabla p)_P$$

to get new velocity field $\mathbf{v}^{**}$ consistent with the pressure field.

Solution Procedure for a Two-Fluid System

The solution sequence of a two-fluid system is the following:

1. initialize all the variables;

2. calculate the Courant number and adjust the time step if necessary;

3. solve α equation (3.37):

$$\alpha_P^n \frac{V_P}{\Delta t} + \sum_{f=1}^{n} \frac{1}{2}(\alpha \mathbf{F})_f^n = S_{\alpha_P} \,,$$

using the old time-level volumetric fluxes;

4. use the new α values together with the constitutive relations (3.7) and (3.8):

$$\rho = \alpha\rho_1 + (1-\alpha)\rho_2 \,,$$

$$\mu = \alpha\mu_1 + (1-\alpha)\mu_2 \,,$$

to obtain an estimate for the new viscosity, density and the face densities from (3.46):

$$\rho_f = \frac{1}{2}(\alpha_f^o + \alpha_f^n)\rho_1 + \left(1 - \frac{1}{2}(\alpha_f^o + \alpha_f^n)\right)\rho_2 \,;$$

5. use the above values to do a momentum prediction and continue with the PISO algorithm;

6. if the final time has not yet been reached, advance to the next time level and return to step 2.

Chapter 4.

Thin Liquid Film

Thin liquid film model represents a two-dimensional mathematical description of two-phase flows. Discretisation of the model according to the Finite Area Method (FAM), developed by [35], makes it suitable for CFD simulations.

The mathematical formulation in Section 4.1. is written as described by the original author of `liquidFilmFoam` solver [36]. The appropriate numerical model presented in Section 4.2. is taken from [35, 36]. Similar to the FVM, the discretisation procedure used in the FAM includes discretisation of computational domain and discretisation of mathematical model, where partial differential equations are transformed into a set of linear algebraic equations.

Thin liquid film model formulation as implemented in the current version of `foam-extend`[1] is given in Section 4.3.

4.1. Mathematical Model

Fluid flows are intrinsically three-dimensional. However, under certain circumstances, fluid flow can be accurately described using a reduced, two-dimensional mathematical model such as the *thin liquid film model*. Application of this model is limited to flows where the liquid layer thickness is significantly smaller than the other two dimensions, which provides the basis for the depth-averaged integration.

The thin liquid film model considers laminar liquid flow over an arbitrarily curved solid surface (Figure 4.1). The flow is isothermal and driven by forces due to surface

[1] `foam-extend 4.0`

tension, gravity, Coriolis force due to the rotation of the substrate and gas shear stress at the free surface. Since the film is sufficiently thin, the boundary layer approximation is valid:

- gradients in tangential direction are negligible compared to gradients in normal direction;
- normal component of velocity is negligible compared to tangential component;
- liquid film pressure is constant across the film thickness.

In addition to the boundary layer approximation, the velocity profile function is prescribed as a cubic polynomial. This assumption allows velocity to be expressed as a depth-averaged quantity, thus enabling the two-dimensional mathematical representation.

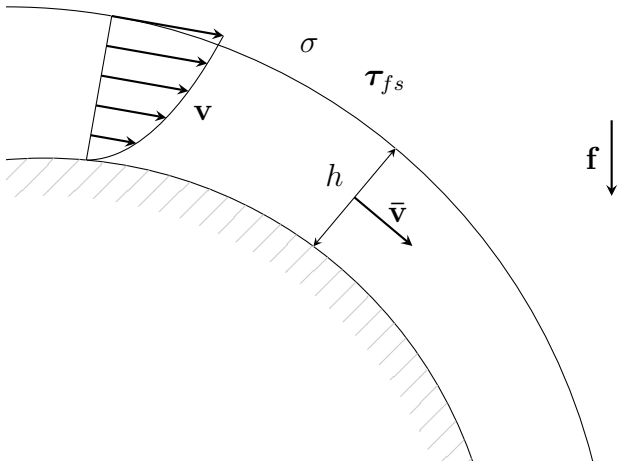

Figure 4.1: Thin liquid film

4.1.1. Continuity Equation

Figure 4.2 shows thin liquid film control volume V enclosed within a boundary control surface S. Integral form of the continuity equation for the control volume is:

$$\frac{d}{dt}\int_V dV + \oint_S \mathbf{n}\cdot(\mathbf{v}-\mathbf{v}_S)dS = \frac{1}{\rho}\int_V Q^m dV\ , \tag{4.1}$$

where $\mathbf{n}$ stands for the outward-pointing unit normal vector to the control surface, $\mathbf{v}$ is the liquid velocity, $\mathbf{v}_S$ is the control surface velocity, ρ is the liquid density and Q^m

is the mass source volume density. In order to simplify the net surface flux integral, the boundary surface S is split into segments, following the nomenclature presented in Figure 4.3. Subscript w denotes quantities at the solid substrate surface, subscript fs denotes the free surface and subscript io the inlet/outlet surface. Accordingly, the continuity equation (4.1) takes the following form:

$$\frac{d}{dt}\int_V dV + \int_{S_w} \mathbf{n}_w \cdot (\mathbf{v} - \mathbf{v}_w) dS + \int_{S_{io}} \mathbf{n}_{io} \cdot (\mathbf{v} - \mathbf{v}_{io}) dS + \int_{S_{fs}} \mathbf{n}_{fs} \cdot (\mathbf{v} - \mathbf{v}_{fs}) dS = \frac{1}{\rho}\int_V Q^m dV \; . \tag{4.2}$$

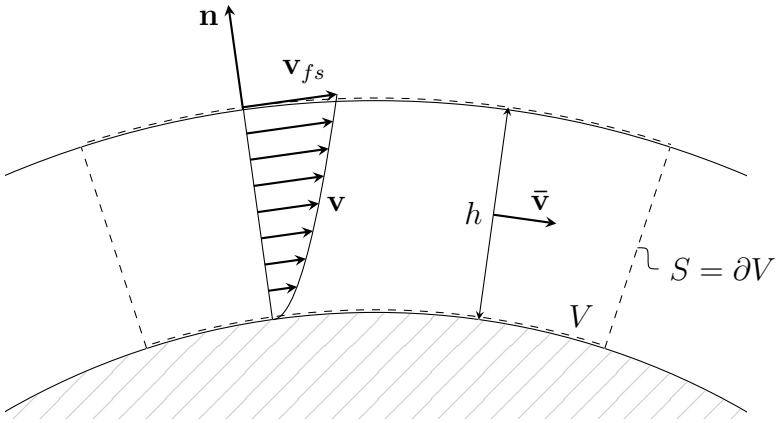

Figure 4.2: Thin liquid film control volume

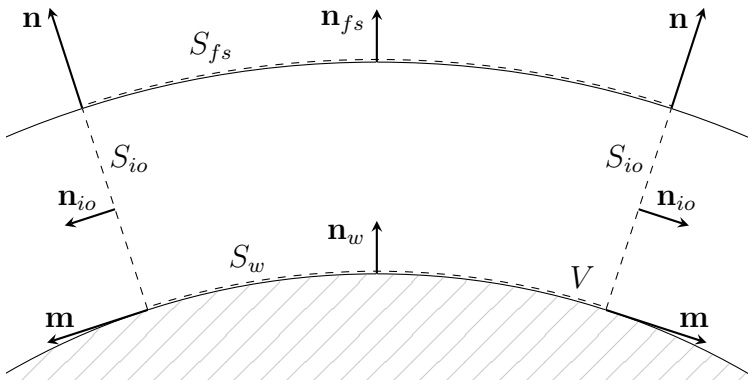

Figure 4.3: Control volume boundary surface

In the case of immobile substrate surface S_w the velocity $\mathbf{v}_w$ is equal to zero. Furthermore, due to the prescribed cubic velocity profile, the liquid velocity at the substrate boundary is also equal to zero. This implies that there is no flux at the substrate boundary. There is no flux at the free surface as well, since the free surface moves with the same surface-normal velocity as the liquid particles, implying $\mathbf{n}_{fs} \cdot (\mathbf{v} - \mathbf{v}_{fs}) = 0$. Finally, the inlet/outlet boundaries are fixed ($\mathbf{v}_{io} = 0$), so the only contributor to the net surface flux stems from the liquid velocity at the inlet/outlet boundary. Therefore, equation (4.2) is reduced to:

$$\frac{d}{dt}\int_V dV + \int_{S_{io}} \mathbf{m} \cdot \mathbf{v} dS = \frac{1}{\rho}\int_V Q^m dV \,, \tag{4.3}$$

where $\mathbf{m} \equiv \mathbf{n}_{io}$ is the outward pointing unit bi-normal vector to the inlet/outlet boundary surface. The equation (4.3) is a three-dimensional mathematical representation of the mass conservation within the control volume V. To make it two-dimensional, the volume integrals are written as surface integrals using $dV = h dS_w$ and surface integrals are written as line integrals using $dS_{io} = h dL_{io}$. Quantity h represents the local liquid film thickness and $L_{io} = \partial S_w$ represents the boundary line of the surface S_w. Finally, by introducing the mass source surface density as $\bar{Q}^m = hQ^m$, equation (4.3) is written as:

$$\frac{d}{dt}\int_{S_w} h dS + \oint_{L_{io}} \mathbf{m} \cdot \left(\int_0^h \mathbf{v} dh \right) dL = \frac{1}{\rho}\int_{S_w} \bar{Q}^m dS \,. \tag{4.4}$$

Since the depth-averaged velocity, which, in accordance to the boundary layer approximation, is tangential to the surface S_w, is defined as:

$$\bar{\mathbf{v}} = \frac{1}{h}\int_0^h \mathbf{v} dh \,, \tag{4.5}$$

the continuity equation takes this final form:

$$\int_{S_w} \frac{\partial h}{\partial t} dS + \oint_{L_{io}} h \mathbf{m} \cdot \bar{\mathbf{v}} dL = \frac{1}{\rho}\int_{S_w} \bar{Q}^m dS \,. \tag{4.6}$$

4.1.2. Momentum Equation

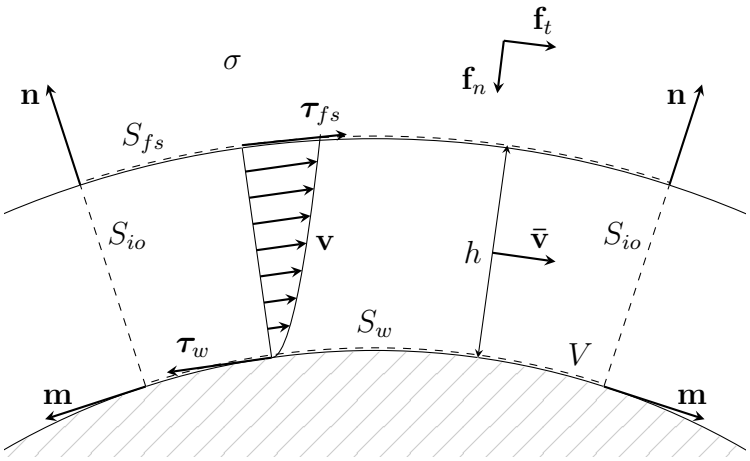

Figure 4.4: Thin liquid film flow driving forces

The main driving forces behind the flow are the body force, the surface tension force and the gas shear force at the free surface. Influence of those is included in the momentum equation. For the control volume V presented in Figure 4.4, the integral form of the momentum equation is the following:

$$\begin{aligned}\frac{d}{dt}\int_V \mathbf{v}dV + \oint_S \mathbf{n}\cdot\mathbf{v}(\mathbf{v}-\mathbf{v}_S)dS = \frac{1}{\rho}\oint_S \mathbf{n}\cdot(\mu\nabla\mathbf{v})dS + \int_V \mathbf{f}dV \\ -\frac{1}{\rho}\int_V \nabla p dV + \frac{1}{\rho}\int_V \mathbf{Q}^V dV\,,\end{aligned} \tag{4.7}$$

where μ is the liquid dynamic viscosity, $\mathbf{f}$ is the body force vector, p is the pressure and $\mathbf{Q}^V$ is the momentum source volume density.

Equation (4.7) is transformed in similar manner as the continuity equation (4.1). First, the surface is split into segments. Liquid and surface velocities at the boundaries are as described previously, thus fluxes at the substrate and at the free surface are zero in the convective term. According to the boundary layer approximation, the tangential components of gradients are negligible, hence the diffusive term integrals for inlet/outlet surface are also zero. The equation is then reduced to a two-dimensional form by again writing the volume integrals as surface integrals and surface integrals as line integrals. The momentum source volume density is included into the momentum source surface

density: $\bar{\mathbf{Q}}^V = h\mathbf{Q}^V$. The equation (4.7) is hence reduced to:

$$\begin{aligned}\frac{d}{dt}\int_{S_w}\left(\int_0^h \mathbf{v}dh\right)dS + \oint_{L_{io}} \mathbf{m}\cdot\left(\int_0^h \mathbf{v}\mathbf{v}dh\right)dL = \frac{1}{\rho}\oint_{S_{fs}} \mathbf{n}\cdot(\mu\nabla\mathbf{v})dS \\ +\frac{1}{\rho}\oint_{S_w} \mathbf{n}\cdot(\mu\nabla\mathbf{v})dS + \int_{S_w} h\mathbf{f}_t dS - \frac{1}{\rho}\int_{S_w} h\nabla_s p dS + \frac{1}{\rho}\int_{S_w} \bar{\mathbf{Q}}_t^V dS\,.\end{aligned} \tag{4.8}$$

Pressure gradient, body force and the source term vectors are split into normal and tangential components. Thus, $\nabla_s p$ is the tangential component of the pressure gradient. Due to the boundary layer approximation, the normal component of the pressure gradient is set to zero. Quantities $\mathbf{f}_t$ and $\bar{\mathbf{Q}}_t^V$ refer to the tangential components of the body force and the source term. The respective normal components of aforementioned quantities are taken into account via the pressure term. Using the mean velocity (4.5), the equation (4.8) becomes:

$$\begin{aligned}\frac{d}{dt}\int_{S_w} h\bar{\mathbf{v}}dS + \oint_{\partial S_w} \mathbf{m}\cdot(h\overline{\mathbf{v}\mathbf{v}} + \boldsymbol{\xi})dL = \frac{1}{\rho}\int_{S_{fs}\approx S_w} \boldsymbol{\tau}_{fs}dS - \frac{1}{\rho}\int_{S_w} \boldsymbol{\tau}_w dS \\ + \int_{S_w} h\mathbf{f}_t dS - \frac{1}{\rho}\int_{S_w} h\nabla_s p dS + \frac{1}{\rho}\int_{S_w} \bar{\mathbf{Q}}_t^V dS\,,\end{aligned} \tag{4.9}$$

where $\boldsymbol{\tau}_w$ is the tangential viscous stress force at the substrate boundary defined as: $\boldsymbol{\tau}_w = \mathbf{n}_w \cdot (\mu\nabla\mathbf{v})_w$. The tangential viscous stress force at the free surface $\boldsymbol{\tau}_{fs}$ is treated as specified and the correction tensor $\boldsymbol{\xi}$ is defined as:

$$\boldsymbol{\xi} = \int_0^h \mathbf{v}\mathbf{v}dh - h\overline{\mathbf{v}\mathbf{v}}\,. \tag{4.10}$$

The purpose of introducing the correction tensor $\boldsymbol{\xi}$ is to recover the difference in the convection term due to the usage of the mean velocity instead of the velocity profile function. Finally, the pressure term in equation (4.9) is reformulated according to the product differentiation rule:

$$h\nabla_s p = \nabla_s(hp) - p\nabla_s h\,. \tag{4.11}$$

This formulation ensures coupling of pressure and film thickness in the numerical procedure.

4.1.3. Liquid Film Velocity Profile

In order to determine the velocity profile, needed for calculation of the tangential viscous stress force $\boldsymbol{\tau}_w$ and correction tensor $\boldsymbol{\xi}$ in equation (4.9), a dimensionless distance

η is introduced:

$$\eta = \frac{h'}{h} \,, \tag{4.12}$$

where h' is the corresponding dimensional distance from the substrate across the film thickness: $0 \leq h' \leq h$. Using this dimensionless distance, velocity is expressed as:

$$\mathbf{v}(\eta) = \mathrm{diag}(\mathbf{v}_{fs}) \cdot \mathbf{F}(\eta) \,. \tag{4.13}$$

Equation (4.13) stems from the assumption that the flow variables are similar in the direction normal to substrate surface. The diagonal tensor $\mathrm{diag}(\mathbf{v}_{fs})$ consist of components of the film velocity at the free surface. Profile function $\mathbf{F}(\eta)$ is prescribed as:

$$\mathbf{F}(\eta) = \mathbf{a}\eta + \mathbf{b}\eta^2 + \mathbf{c}\eta^3 \,, \tag{4.14}$$

where $\mathbf{a}, \mathbf{b}$ and $\mathbf{c}$ are profile coefficients of the cubic polynomial, determined from the boundary conditions, as it will be described later. To express the mean liquid film velocity $\bar{\mathbf{v}}$, the profile integral vector $\boldsymbol{I}$ is introduced:

$$\boldsymbol{I} = \int_0^1 \mathbf{F}(\eta) d\eta = \frac{1}{2}\mathbf{a} + \frac{1}{3}\mathbf{b} + \frac{1}{4}\mathbf{c} \,. \tag{4.15}$$

Using the expression (4.15), the mean velocity is written as:

$$\bar{\mathbf{v}} = \mathrm{diag}(\mathbf{v}_{fs}) \cdot \boldsymbol{I} \,. \tag{4.16}$$

Profile coefficients in equation (4.14) have to be determined from boundary conditions, since they change in space and time. These boundary conditions are:

- at the substrate ($\eta = 0$):

$$F_i''(0) = I_i \frac{h^2}{\mu \bar{v}_i} [(\nabla_s p)_i - \rho (f_t)_i] \,, \tag{4.17}$$

- at the free surface ($\eta = 1$):

$$F_i(1) = 1 \,, \tag{4.18}$$

$$F_i'(1) = I_i \frac{(\tau_{fs})_i h}{\mu \bar{v}_i} \,. \tag{4.19}$$

Index i in equations (4.17), (4.18) and (4.19) denotes i-th component of the Cartesian vector and F_i' and F_i'' are the first and second derivatives of the profile function. Writing out the profile function and its derivatives in accordance to (4.14) leads to a system of linear algebraic equations:

$$\begin{aligned} a_i + b_i + c_i &= 1 \,, \\ a_i + 2b_i + 3c_i &= I_i \frac{(\tau_{fs})_i h}{\mu \bar{v}_i} \,, \\ 2b_i &= I_i \frac{h^2}{\mu \bar{v}_i} [(\nabla_s p)_i - \rho (f_t)_i] \,. \end{aligned} \tag{4.20}$$

This system is then solved for the unknown coefficients a_i, b_i and c_i. The quantities $(\tau_{fs})_i, (f_t)_i, p, h$ and $\bar{v}_i$ are treated as specified. So, once the profile coefficients are calculated, the velocity profile is also determined, and the tangential viscous stress force at the substrate can be calculated as:

$$\boldsymbol{\tau}_w = \frac{\mu}{h} \boldsymbol{\Gamma} \cdot \bar{\mathbf{v}} \,, \tag{4.21}$$

with the diagonal tensor $\boldsymbol{\Gamma}$ is defined as:

$$\boldsymbol{\Gamma} = \mathrm{diag}^{-1}(\boldsymbol{I}) \cdot \mathrm{diag}[\mathbf{F}'(0)] \,. \tag{4.22}$$

Tangential viscous stress force, as defined in (4.21), tends to infinity when $h = 0$. To avoid this, it is assumed that the whole area is pre-wetted by introducing the precursor film thickness. Finally, for the calculation of the correction $\boldsymbol{\xi}$, with the known profile coefficients, the integral in equation (4.10) takes the following form:

$$\boldsymbol{I}_{vv} = \int_0^h \mathbf{v}\mathbf{v} dh = \mathrm{diag}^2(\mathbf{v}_{fs}) \cdot \left(\frac{1}{3}\mathbf{a}\mathbf{a} + \frac{1}{5}\mathbf{b}\mathbf{b} + \frac{1}{7}\mathbf{c}\mathbf{c} + \frac{1}{2}\mathbf{a}\mathbf{b} + \frac{2}{5}\mathbf{a}\mathbf{c} + \frac{1}{5}\mathbf{b}\mathbf{c} \right) . \tag{4.23}$$

4.1.4. Liquid Film Pressure

The pressure term in the momentum equation (4.9) is written as a sum of two parts: the capillary pressure due to the surface tension and the hydrostatic pressure due to the normal component of body force vector. Capillary (or Laplace) pressure can be expressed as:

$$p_\sigma = -\sigma C \,, \tag{4.24}$$

where σ is the surface tension coefficient and C is the mean interface curvature approximated as:

$$C \approx \left(\frac{1}{R_1} + \frac{1}{R_2}\right) + \left(\frac{h}{R_1^2} + \frac{h}{R_2^2}\right) + \nabla_s \cdot \nabla_s h \, . \tag{4.25}$$

In (4.25), R_1 and R_2 denote the principal radii of curvature of the substrate surface. Under the assumption that the ratio between the film thickness and the minimal principal radii of substrate surface curvature is small enough, second term in equation (4.25) is neglected. Therefore, the expression is reduced to:

$$C \approx C_w + \nabla_s \cdot (\nabla_s h) \, . \tag{4.26}$$

Quantity C_w is the mean curvature of substrate surface expressed as:

$$C_w = \nabla_s \cdot \mathbf{n}_w \, . \tag{4.27}$$

The hydrostatic part of the pressure takes into account the normal components of the body force:

$$p_h = -\mathbf{n}_w \cdot \mathbf{f} h \, . \tag{4.28}$$

With both capillary and hydrostatic pressure determined, the total liquid film pressure is the following:

$$p = p_\sigma + p_h = -\sigma C_w - \sigma \nabla_s \cdot (\nabla_s h) - \mathbf{n}_w \cdot \mathbf{f} h \, . \tag{4.29}$$

4.2. Numerical Model

Numerical formulation presented in this section is taken from [35, 36].

4.2.1. Discretisation of Computational Domain

The computational domain consists of the time interval and the computational space. Temporal discretisation is performed by splitting the time interval into a finite number of time steps Δt, of equal or varying durations. The equations are then solved in a time-marching manner, so that the solutions in the current time instance $t = t^n$ depend on the already determined ones from the previous time instance $t = t^o$. The two instances are separated by the duration of time step: $t^n = t^o + \Delta t$.

Spatial discretisation is performed on the curved substrate surface, so that the computational space is completely covered by a finite number of non-overlapping control areas (CA). The CAs are flat and convex polygons, bounded by an arbitrary number of edges.

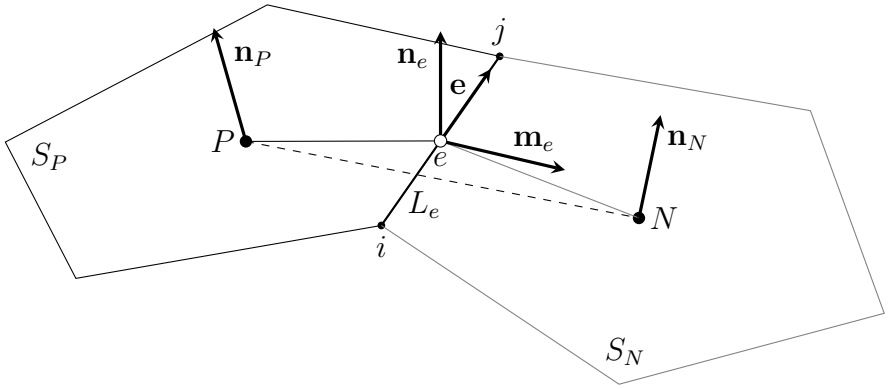

Figure 4.5: Polygonal control area

Figure 4.5 shows two sample neighbouring CAs, denoted as S_P and S_N with their respective unit normal vectors $\mathbf{n}_P$ and $\mathbf{n}_N$ pointing outward from the computational points, P and N, located at their centroids. Their shared edge of length L_e has its local orthogonal coordinate system, determined by its vertices i and j.

Edge-based unit normal vector $\mathbf{n}_e$ is calculated as an average of unit normal vectors at the vertices:

$$\mathbf{n}_e = \frac{\mathbf{n}_i + \mathbf{n}_j}{|\mathbf{n}_i + \mathbf{n}_j|} \,. \tag{4.30}$$

Unit bi-normal vector $\mathbf{m}_e$ is tangential to the discretised surface and points towards the neighbouring CA. It is determined as orthogonal to the edge and its unit normal vector $\mathbf{n}_e$, using the following relation:

$$\mathbf{m}_e = \mathbf{e} \times \mathbf{n}_e \,, \tag{4.31}$$

where $\mathbf{e}$ is the unit vector parallel to the edge.

4.2.2. Discretisation of Mathematical Model

Fully discretised form of the momentum equation (4.9) for the control area S_P reads as:

$$\begin{aligned}\frac{3h_P^n\bar{\mathbf{v}}_P^n - 4h_P^o\bar{\mathbf{v}}_P^o + h_P^{oo}\bar{\mathbf{v}}_P^{oo}}{2\Delta t}S_P + \sum_e h_e^n(\mathbf{m}\cdot\bar{\mathbf{v}})_e^n L_e + \sum_e(\mathbf{m}\cdot\boldsymbol{\xi})_e^n L_e = \frac{1}{\rho}(\boldsymbol{\tau}_{fs})_P^n S_P \\ -\frac{1}{\rho}(\boldsymbol{\tau}_w)_P^n S_P + h_P^n(\mathbf{f}_t)_P^n S_P - \frac{1}{\rho}[\nabla_s(hp)]_P^n S_P + \frac{1}{\rho}p_P^n(\nabla_s h)_P^n S_P + (\bar{\mathbf{Q}}_t^V)_P^n S_P\,.\end{aligned} \tag{4.32}$$

Here, subscript P refers to the centroid of the CA and subscript e refers to centre points of its bounding edges. According to the FA method, surface integrals from (4.9) are approximated by the face values defined at the centroid of CA, while the line integrals are represented by sums of edge integrals. Both are approximated by using the midpoint rule, which indicates second order accuracy. Superscript n refers to values at a new time-level, o refers to values at the old time-level, and oo to values at the "second old" time-level, defined as $t^{oo} = t^o - \Delta t^o$ – the three time-levels are due to the implicit backward temporal discretisation scheme of second order accuracy. At the first time step only one time-level is available, so the first order accurate Euler scheme is used for temporal discretisation.

The edge-centre value of mean liquid film velocity is interpolated from corresponding face-centre values using the expression which accounts for surface curvature:

$$\bar{\mathbf{v}}_e = (\mathbf{T}_e)^{\mathrm{T}}[e_x\mathbf{T}_P\cdot\bar{\mathbf{v}}_P + (1-e_x)\mathbf{T}_N\cdot\bar{\mathbf{v}}_N]\,, \tag{4.33}$$

where $\mathbf{T}_P$, $\mathbf{T}_N$ and $\mathbf{T}_e$ are transformation tensors from the global Cartesian coordinate system to the edge based local orthogonal system. Interpolation factor e_x is defined as the ratio of geodetic distances $\overline{eN}$ and $\overline{PeN}$ (Figure 4.5):

$$e_x = \frac{\overline{eN}}{\overline{PeN}}\,. \tag{4.34}$$

Other tensor or vector quantities at the edge centre are also interpolated using the equation (4.33), while scalars, for example edge-centre value of film thickness, do not need to be transformed from global to local coordinate system and are evaluated using this expression:

$$h_e = e_x h_P + (1-e_x)h_N\,. \tag{4.35}$$

Face-to-edge interpolation of convected velocity is performed using the *deffered correction* approach. Thus, the convection flux $(\mathbf{m} \cdot \boldsymbol{\xi})_e^n$ is evaluated using the following expression:

$$(\mathbf{m} \cdot \boldsymbol{\xi})_e^n = (\boldsymbol{I}_{vv})_e^n - h_e^n (\mathbf{m} \cdot \bar{\mathbf{v}})_e^n \bar{\mathbf{v}}_e^n \,, \tag{4.36}$$

where integral $(\boldsymbol{I}_{vv})_e^n$ is determined by linear interpolation of neighbouring face values. The tangential viscous stress force at the substrate $(\boldsymbol{\tau}_w)_P^n$ is also interpolated using the deffered correction approach:

$$(\boldsymbol{\tau}_w)_P^n = \frac{\mu}{h_P^n} \max(\boldsymbol{\Gamma}_P^n) \bar{\mathbf{v}}_P^n + \frac{\mu}{h_P^n} [\boldsymbol{\Gamma}_P^n - \max(\boldsymbol{\Gamma}_P^n)\mathbf{I}] \cdot \bar{\mathbf{v}}_P^n \,, \tag{4.37}$$

which implies implicit treatment of the first term on the right hand side of the equation and explicit treatment of the second (correction) term. Approximation of surface gradients is carried out using the following expression, written out for the example of film thickness:

$$(\nabla_s h)_P = \frac{1}{S_P} (\mathbf{I} - \mathbf{n}_P \mathbf{n}_P) \cdot \sum_e \mathbf{m}_e h_e L_e \,. \tag{4.38}$$

The pressure term from (4.32) is obtained by discretisation of equation (4.29):

$$p_P = -\sigma_P C_P - \sigma_P (\nabla_s \cdot \nabla_s h)_P - \mathbf{n}_P \mathbf{f}_P h_P \,. \tag{4.39}$$

The laplacian term from (4.39) is expressed as:

$$(\nabla_s \cdot \nabla_s h)_P = \frac{1}{S_P} \sum_e \mathbf{m}_e \cdot (\nabla_s h)_e L_e \,, \tag{4.40}$$

with edge bi-normal derivative calculated as:

$$\mathbf{m}_e \cdot (\nabla_s h)_e = |\boldsymbol{\Delta}_e| \frac{h_N - h_P}{L_{PN}} + \mathbf{k}_e \cdot (\nabla_s h)_e \,. \tag{4.41}$$

The first term of the right hand side of equation (4.41) represents the orthogonal contribution while the second term represent the non-orthogonal correction. Hence, quantity $\boldsymbol{\Delta}_e$ represents the orthogonal part of the unit bi-normal $\mathbf{m}_e$ defined as:

$$\boldsymbol{\Delta}_e = \frac{\mathbf{t}_e}{\mathbf{t}_e \cdot \mathbf{m}_e} \,, \tag{4.42}$$

where $\mathbf{t}_e$ stands for the unit vector tangential to the geodetic line $\overline{PeN}$ at the edge centre e. Quantity L_{PN} in the orthogonal contribution from equation (4.41) is the

length of mentioned geodetic distance $\overline{PeN}$. Finally, the non-orthogonal part of the unit bi-normal $\mathbf{m}_e$ is calculated as:

$$\mathbf{k}_e = \boldsymbol{\Delta}_e - \mathbf{m}_e \, . \tag{4.43}$$

The described procedure allows equation (4.32) to be written as a linear algebraic expression:

$$a_P^v \bar{\mathbf{v}}_P^n + \sum_N a_N^v \bar{\mathbf{v}}_N^n = \mathbf{r}_P^v - \frac{1}{\rho}\{[\nabla_s(hp)]_P^n - p_P^n(\nabla_s h)_P^n\} \, , \tag{4.44}$$

with the diagonal coefficient a_P, the neighbouring coefficients a_N and the source term $\mathbf{r}_P$ all depending on the unknown film thickness and velocity.

The continuity equation (4.6) for the control area CA takes this fully discretised form:

$$\frac{3h_P^n - 4h_P^o + h_P^{oo}}{2\Delta t} S_P + \sum_e (\mathbf{m} \cdot \bar{\mathbf{v}})_e^n h_e^n L_e = (\bar{\mathbf{Q}}^m)_P^n S_P \, . \tag{4.45}$$

To achieve effective coupling between film thickness and velocity, bi-normal edge velocity $(\mathbf{m}\cdot\bar{\mathbf{v}})_e^n$ is calculated using the momentum interpolation method. The face value velocity is expressed from equation (4.44) as:

$$\bar{\mathbf{v}}_P = \frac{\mathbf{H}_P(\bar{\mathbf{v}}^n)}{a_P^v} - \frac{1}{a_P^v}\frac{1}{\rho}\{[\nabla_s(hp)]_P^n - p_P^n(\nabla_s h)_P^n\} \, , \tag{4.46}$$

with:

$$\mathbf{H}_P(\bar{\mathbf{v}}^n) = -\sum_N a_N^v \bar{\mathbf{v}}_N^n + \mathbf{r}_P^v \, . \tag{4.47}$$

Therefore, the bi-normal edge velocity becomes:

$$(\mathbf{m} \cdot \bar{\mathbf{v}})_e^n = \mathbf{m}_e \cdot \left(\frac{\mathbf{H}}{a}\right)_e^n - \left(\frac{1}{a}\right)_e^n \frac{1}{\rho}\{\mathbf{m}_e \cdot [\nabla_s(hp)]_e^n - p_e^n \mathbf{m}_e \cdot (\nabla_s h)_e^n\} \, , \tag{4.48}$$

where terms $(\mathbf{H}/a)_e^n$ and $(1/a)_e^n$ are calculated using face-to-edge linear interpolation. Finally, the continuity equation (4.45) takes the following linear algebraic form:

$$a_P^h h_P^n + \sum_N a_N^h h_N^n = \mathbf{r}_P^h \, . \tag{4.49}$$

4.3. `liquidFilmFoam` Solver

The current version of `foam-extend`[2] utilizes a modified thin liquid film mathematical formulation. The key difference lies in the handling of viscous stress term $\boldsymbol{\tau}_w$.

[2] `foam-extend 4.0`

The viscous stress term is calculated using a version of Manning's formula [37]. First, the friction factor C_f is calculated using standard gravity for stabilisation:

$$C_f = \frac{2 \cdot 9,81 M^2}{(h + 1 \cdot 10^{-7})^{1/3}} \,, \tag{4.50}$$

where M is the internal field value of Manning field coefficient, usually set to $0,01$ m, for smooth surfaces. Using the friction factor based on Manning coefficient and film thickness h, makes this formulation practical for cases with material-based surface friction [38].

With the surface friction factor C_f determined, the viscous stress is the following:

$$\boldsymbol{\tau}_w = 0,0125 \mathrm{C}_f |\bar{\mathbf{v}}| \bar{\mathbf{v}} \,, \tag{4.51}$$

where $|\bar{\mathbf{v}}|$ is the mean velocity magnitude. Major consequence of this formulation is that the velocity profile becomes obsolete: in previous formulation (Section 4.1.), the shape of the velocity profile determined the viscous drag on the wall. Here, the wall drag is calculated using the material-sensitive Manning's coefficient, meaning that the velocity profile is a consequence of the wall drag and not *vice versa* [39].

Thus, the correction tensor $\boldsymbol{\xi}$ can be neglected from the momentum equation (4.9), reducing it to the following form:

$$\begin{aligned} \frac{d}{dt} \int_{S_w} h \bar{\mathbf{v}} dS + \oint_{\partial S_w} \mathbf{m} \cdot (h \overline{\mathbf{v}\mathbf{v}}) dL = \frac{1}{\rho} \int_{S_{fs} \approx S_w} \boldsymbol{\tau}_{fs} dS - \frac{1}{\rho} \int_{S_w} \boldsymbol{\tau}_w dS \\ + \int_{S_w} h \mathbf{f}_t dS - \frac{1}{\rho} \int_{S_w} h \nabla_s p dS \,. \end{aligned} \tag{4.52}$$

Since none of the momentum source terms were considered in this thesis, term $\bar{\mathbf{Q}}_t^V$ from equation (4.9) is also neglected. Similarly, in the continuity equation (4.6), mass source term $\bar{Q}^m$ is set to zero, making the continuity equation read as:

$$\int_{S_w} \frac{\partial h}{\partial t} dS + \oint_{L_{io}} h \mathbf{m} \cdot \bar{\mathbf{v}} dL = 0 \,. \tag{4.53}$$

Discretisation procedure remains as described in Section 4.2.

4.4. Conclusion

Using the prescribed cubic polynomial velocity distribution implies that the velocity at the substrate is equal to zero. This is in accordance with the no-slip boundary

condition. However, as shown by [40], when applied to two-phase flows, no-slip boundary condition leads to a stress singularity at the contact line. This is described in Section 4.1.3., where equation (4.21) shows that the tangential viscous stress at the substrate $\boldsymbol{\tau}_w$ tends to infinity when $h = 0$. Resolution of this contact line singularity is achieved by assuming that the whole substrate area is pre-wetted with a microscopic liquid film called *precursor film*. The precursor film thickness h_p is greater than zero, thus solution of equation (4.21) becomes definite.

Although the formulation of thin liquid film model, as described in Section 4.3., neglects the velocity profile, the assumption of precursor film is still justified. Reducing the film thickness h to zero would bring inconsistency to the momentum equation (4.52).

Direct implication of adopting the precursor film thickness is that of complete wetting. In other words, the thin liquid film formulation as given in this chapter represents the whole computational domain as the free surface between the fluids, which makes it unsuitable for simulations of partial wetting.

Thus, an expanded formulation of the thin liquid model is given in Chapter 5., which allows simulation of liquid-wall interaction. Numerical solution procedure for the expanded model is also given within the following chapter.

Chapter 5.

Modelling of Wall Wetting

A mathematical description of wall wetting was implemented in the CFD toolbox `foam-extend`, using two distinctive approaches. The first approach uses the 3-D Volume of Fluid method, in `foam-extend` realized within the `interFoam` solver. In `interFoam`, liquid-wall interaction is described using a boundary condition. Mathematical and numerical formulation of the boundary condition is given in Section 5.1.

The second approach uses the 2-D thin liquid film model, realized in the `liquidFilmFoam` solver within the `foam-extend` CFD toolbox. Here, the wall wetting is modelled by adding a force term directly into the momentum equation, resulting in a new thin liquid film mathematical formulation. The formulation is given in Section 5.2.

5.1. Volume of Fluid

5.1.1. Specification of Interface Normal

For physically accurate description of wetting, the boundary of interest is the wall, i.e. the impermeable solid substrate. With this solid boundary the liquid forms a contact angle which governs the spreading. In `interFoam`, this is accounted for by specifying the interface normal $\mathbf{n}_I$ needed for the calculation of interface curvature at the wall boundary [15]:

$$\mathbf{n}_I = \mathbf{n}_w \cos\theta_e + \mathbf{n}_t \sin\theta_e \,. \tag{5.1}$$

In the above equation, $\mathbf{n}_w$ is the unit normal vector to the wall boundary pointing towards the wall and $\mathbf{n}_t$ is the unit tangential vector to the wall pointing towards the

liquid. This formulation uses the static equilibrium contact angle θ_e for specification of the interface normal $\mathbf{n}_I$. However, as it was described in Chapter 2., using a constant value of the contact angle is insufficient since liquid tends to assume varied contact angles in dynamic situations. Thus, the equation (5.1) is rewritten in a more general form:

$$\mathbf{n}_I = \mathbf{n}_w \cos\theta + \mathbf{n}_t \sin\theta \,, \tag{5.2}$$

using the apparent contact angle θ instead of the equilibrium contact angle θ_e. The calculation of θ is described within the following section.

Considering that the interface normal is defined by (3.18):

$$\mathbf{n}_I = \frac{\nabla\alpha}{|\nabla\alpha|} \,,$$

the corrected value of $\mathbf{n}_I$ from (5.2) is used to adjust the gradient of the indicator function α at the wall boundary, thus limiting the liquid spreading.

5.1.2. Dynamic Contact Angle

Existing dynamic contact angle models were discussed in Section 2.4. Since the nature of liquid spreading is yet to be fully understood by science, it is hard to find a model which would accurately describe the contact line motion in all possible scenarios.

Models based on the molecular-kinetic theory are generally more consistent with the nature of liquid spreading. However, the price comes in form of their complexity: these models take into account the microscopic morphology of the substrate and thus reach out of the scope of continuum mechanics.

Models based on the hydrodynamic theory neglect microscopic properties of the substrate and consequently have a simpler mathematical formulation. However, the Cox-Voinov model (2.8) and its simplified version, the Hoffman-Voinov-Tanner law (2.7), are both limited by the contact line velocity and can be used only for surface tension dominated flows with $\mathrm{Ca} < 1$. A model without this limitation is that of Kistler (2.4):

$$\theta_d = f_{\mathrm{H}}(\mathrm{Ca} + f_{\mathrm{H}}^{-1}(\theta_e)) \,,$$

with the Hoffman function defined by (2.5):

$$f_{\mathrm{H}} = \arccos\left\{1 - 2\tanh\left[5.16\Big[\frac{x}{1+1.13x^{0.99}}\Big]^{0.706}\right]\right\} .$$

Due to its applicability to the full range of liquid velocities, the model above was implemented into the VoF-based `interFoam` solver.

In order to calculate the local capillary number Ca used in equation (2.4), local contact line velocity has to be specified.

Several ways of modelling the contact line velocity can be found in literature. The *conventional* approach, as used in [41], estimates the contact line velocity as a wall parallel projection of the interface-normal component of the cell-centre velocity:

$$(v_{cl})_P = \frac{\mathbf{n}_I - (\mathbf{n}_b \cdot \mathbf{n}_I)\mathbf{n}_b}{|\mathbf{n}_I - (\mathbf{n}_b \cdot \mathbf{n}_I)\mathbf{n}_b|} \cdot \mathbf{v}_P \,, \tag{5.3}$$

where $\mathbf{n}_I$ is the unit normal to the interface from (3.18) and $\mathbf{n}_b$ is the unit normal vector to the substrate boundary. Subscript P denotes the cell-centred values. However, velocity calculated by expression (5.3) is not physical, as shown in [42], and has to be corrected with the following expression:

$$(v_{cl,calculated})_P = (v_{cl})_P \frac{\theta \sin^2 \theta}{\theta - \cos\theta \sin\theta} \,, \tag{5.4}$$

where θ stands for the apparent contact angle, determined from the old time-level of the indicator function gradient.

In [27], velocity of the contact line propagation is calculated using the following expression:

$$(v_{cl})_P = \frac{\mathbf{v}_P \cdot \mathbf{n}_I}{\sqrt{1 - \mathbf{n}_b \cdot \mathbf{n}_I}} \,. \tag{5.5}$$

Expression (5.5) was also used for the estimation of the contact line velocity in this thesis.

Once the contact line velocity is determined, local capillary number is calculated using the equation (5.18):

$$\mathrm{Ca}_P = \frac{\mu (v_{cl})_P}{\sigma} \,.$$

The apparent contact angle can be then determined using the Kistler's model (2.4), where the equilibrium contact angle θ_e would be equal to receding or advancing contact angle, depending on the contact line propagation direction. Determination of the propagation direction is performed using the procedure given by [27], where the computational point velocity is compared to the interface normal:

$$\bar{\mathbf{v}}_P \cdot (\mathbf{n}_{cl})_P > 0 \,, \tag{5.6}$$

$$\bar{\mathbf{v}}_P \cdot (\mathbf{n}_{cl})_P < 0 \,. \tag{5.7}$$

If expression (5.6) is true, the computational cell is identified as a part of the advancing front and equation (2.4) is calculated with $\theta_e = \theta_a$. In the opposite case, when (5.7) is true, the cell is a part of the receding front and $\theta_e = \theta_r$ is used.

With the dynamic contact angle determined, new-time level interface normal $\mathbf{n}_I$ is calculated using the expression (5.1):

$$\mathbf{n}_I = \mathbf{n}_w \cos\theta + \mathbf{n}_t \sin\theta \,.$$

Resulting interface normal aligns the indicator function gradient at the solid boundary, used for the calculation of curvature in the surface tension term $\mathbf{f}_\sigma$, thus introducing the liquid-wall interaction into the momentum equation 3.16:

$$\frac{\partial(\rho\mathbf{v})}{\partial t} + \nabla \cdot (\rho\mathbf{v}\mathbf{v}) - \nabla \cdot (\mu\nabla\mathbf{v}) = -\nabla p + \rho\mathbf{g} + \mathbf{f}_\sigma + (\nabla\mathbf{v}) \cdot (\nabla\mu) \,.$$

5.2. Thin Liquid Film

5.2.1. Introduction

The formulation of thin liquid film model implemented in `liquidFilmFoam` assumes the state of complete wetting, due to the usage of percursor film thickness. To take into account phenomena which emerges as the result of partial wetting, area wetted with precursor film must be considered as dry. Accordingly, film of greater height than that of the precursor must be treated as a macroscopic liquid object.

As described in Chapter 2., partial wetting is inherently linked to the existence of contact angles. A surface-tangential force due to interaction of surface tensions at the contact line governs the dynamic behaviour of the liquid object. Quantity of this force in isothermal conditions varies only with the variation of the contact angle. Thus, to enable modelling of partial wetting flows (such as flows of droplets and rivulets), an additional term must be included into the momentum equation (4.9), where the influence of the contact angle would be accounted for.

Disjoining Pressure Approach

In thin liquid film theory, a common approach is to model the contact line behaviour using the *disjoining pressure* term, first introduced by [43, 44]. For example in [45], this

term is added into the stress balance condition at the free surface:

$$\mathbf{n} \cdot (-p\mathbf{I} + \boldsymbol{\sigma}) \cdot \mathbf{n} = \sigma\kappa + \Pi(h) \,. \tag{5.8}$$

Here, $\mathbf{n}$ is the unit normal vector to the free surface, p is the pressure, $\mathbf{I}$ is the identity matrix and $\boldsymbol{\sigma}$ is the viscous stress tensor. The normal component of the stresses is mechanically balanced out by the surface tension $\sigma\kappa$, where σ is the surface tension coefficient and κ is the interface curvature, and by the disjoining pressure, $\Pi(h)$, which takes into account the influence of intermolecular forces. Disjoining pressure is a function of film thickness h. In [46], it is defined as:

$$\Pi(h) = \frac{B}{h_p^n}\left[\left(\frac{h_p}{h}\right)^n + \left(\frac{h_p}{h}\right)^m\right], \tag{5.9}$$

where h_p is the precursor film thickness and coefficients (n, m) are such that $n > m > 1$. For example, [47] used values $(3, 2)$ for (n, m) and [46] used $(9, 3)$. An important relation between the disjoining pressure $\Pi(h)$ and the equilibrium contact angle θ_e was given by [47]:

$$\cos\theta_e = 1 - \frac{1}{\sigma}\int_{h_p}^{\infty} \Pi(h)dh \,, \tag{5.10}$$

which allows the coefficient B from (5.9) to be expressed in terms of the equilibrium contact angle. Thus, [45] gives this final relation for the disjoining pressure:

$$\Pi(h) = \frac{(n-1)(m-1)\sigma(1-\cos\theta_e)}{(n-m)h_p}\left[\left(\frac{h_p}{h}\right)^n + \left(\frac{h_p}{h}\right)^m\right]. \tag{5.11}$$

From equation (5.11), it follows that the disjoining pressure depends only on the film thickness h, since quantities m, n, h_p are all constants, while σ and θ_e remain constant in isothermal conditions. However, a drawback of this approach is the fact that the disjoining pressure term is calculated across the entirety of the domain, while, from the perspective of physics, the effect of intermolecular forces is only observed at the contact line. Also, as seen in (5.10), disjoining pressure is linked to the equilibrium contact angle. Thus, applying a dynamic contact angle model to the relation (5.10) would be questionable.

Tangential Tension Approach

Different, less common approach to modelling the contact line behaviour in the thin liquid film theory, is including the contact angle influence into the tangential stress

term. This approach was successfully implemented and validated through simulation of a rivulet flow in [48]. Here, the tangential stress term includes influences of the viscous forces at the substrate, the tangential component of the body force and the stress due to contact angle force. This force is denoted as *tangential force due to surface tension* and defined as:

$$F_\sigma = \sigma + \sigma_{ls} - \sigma_{gs} \, . \tag{5.12}$$

It is important to point out that while F_σ is denoted as force, it is not a vectorial quantity and has a dimension of force per unit length. Using Young's equation (2.1) to express the surface tension at the gas-solid interface, relation (5.12) becomes:

$$F_\sigma = \sigma(1 - \cos\theta) \, , \tag{5.13}$$

where θ refers to the apparent contact angle at the contact line. Force F_σ is then included into tangential stress due to contact angle $\boldsymbol{\tau}_\theta$ as:

$$\boldsymbol{\tau}_\theta = \beta \frac{\sigma(1 - \cos\theta)}{\Delta_{cl}} \mathbf{n}_{cl} \, , \tag{5.14}$$

where Δ_{cl} is the computational cell width in the direction normal to the contact line, $\mathbf{n}_{cl}$ is the unit normal vector to the contact line in the surface-tangential plane and β is an empirical coefficient introduced to account for discrepancies between the theory and observed behaviour of real surfaces.

This approach has the same drawback as the disjoining pressure approach: the stress term is calculated across the whole domain and thus introduces a tangential tension component inconsistent with the physical description of the phenomenon. However, since (5.14) is a function of the apparent contact angle it allows usage of a dynamic contact angle model. In [48], the apparent contact angle was approximated statistically, using a normal distribution with the equilibrium contact angle as a mean value.

5.2.2. Momentum Equation for Partial Wetting

As described in Section 4.1.2., the body force and source terms acting upon the liquid film are split into their normal and tangential components. Normal influence of surface tension is modelled through the capillary pressure term p_σ (Section 4.1.4., equation (4.24)). Tangential influence of surface tension, affected by the contact angle, has to be written into its separate term.

To achieve this, a slightly modified formulation of the *tangential tension approach* from [48] was used. The major difference lies in the contact line treatment. While in [48], the tangential influence was calculated throughout the entirety of the domain, here it was attempted to keep the mathematical formulation as close to the observed physical behaviour as possible. Thus, the contact angle influence is calculated only at the contact line location.

To keep the mathematical model unburdened by numerical quantities, the tangential stress is expressed as contact angle force per unit length:

$$\mathbf{f}_\theta = \beta\sigma(1-\cos\theta)\mathbf{n}_{cl}\ , \tag{5.15}$$

and included the into momentum equation (4.52) as a line integral. Thus, the final form of the momentum equation for partial wetting is the following:

$$\begin{aligned}\frac{d}{dt}\int_{S_w} h\bar{\mathbf{v}}dS + \oint_{\partial S_w} \mathbf{m}\cdot(h\overline{\mathbf{vv}})dL = \frac{1}{\rho}\int_{S_{fs}} \boldsymbol{\tau}_{fs}dS - \frac{1}{\rho}\int_{S_w}\boldsymbol{\tau}_w dS \\ +\frac{1}{\rho}\oint_{L_{cl}}\mathbf{f}_\theta dL + \int_{S_w} h\mathbf{f}_t dS - \frac{1}{\rho}\int_{S_w} h\nabla_s p dS\ .\end{aligned} \tag{5.16}$$

Integration of contact angle force $\mathbf{f}_\theta$ across the contact line length L_{cl} enhances the fact that this force exists only at the location of gas-liquid-solid interface.

Inclusion of the contact angle influence is not the only difference between the partial wetting and the complete wetting model. The stress term at the free surface, in the complete wetting momentum equation (4.9), was integrated over the substrate surface area, under the assumption that the difference between free surface and substrate area is negligible. However, for partial wetting flows this approximation does not hold up. Macroscopic liquid objects such as droplets and rivulets have considerable curvature of the interface, which makes their free surface shape entirely different from that of the substrate.

To calculate the contact angle force $\mathbf{f}_\theta$ needed for the momentum equation, the contact angle θ must be specified. The calculation of the contact angle follows a similar procedure as in the VoF method, described in Section 5.1.2., with the key differences outlined in Section 5.2.4.

5.2.3. Numerical Model for Partial Wetting

In the previous section, a line integral was added into the momentum equation (5.16):

$$\frac{1}{\rho}\oint_{L_{cl}} \mathbf{f}_\theta dL \,,$$

to model the dynamic behaviour of the contact line. However, considering the FAM principles, this integral cannot be discretised in the same manner as line integrals, since those are treated as sums of edge integrals. Contact line spreads itself somewhere across the width of the CA and it does not envelop all of the bounding edges. Therefore, relevant quantities for the contact angle force should be evaluated at face centroids and the integral should be numerically treated as a surface integral.

Inherent quality of the contact angle force is that it acts only upon the location of the gas-liquid-substrate interface. This would be justified by applying the force only to CAs which contain the contact line, while treating the rest with the momentum equation (4.32) which assumes complete wetting. Thus, first the "partially wet" CAs must be identified as such and then a discretised form of the contact angle force should be applied only to them.

Contact Line Location

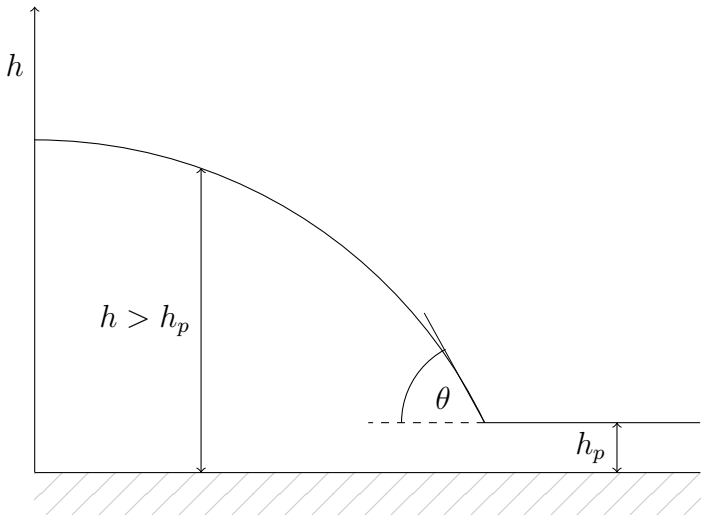

Figure 5.1: Droplet with precursor film

Thin liquid film model introduces the precursor film thickness in order to avoid singularities at the contact line. However, this leads to the conclusion that the whole substrate surface is wetted. In order to separate the macroscopic liquid objects from the precursor film, first the location of the contact line must be determined.

Figure 5.1 shows a side-view of a droplet deposited onto a substrate pre-wetted by a precursor film of uniform thickness h_p. The contact line is found where an abrupt change of thickness gradient takes place. At the location, an apparent contact angle can be measured, since the change in thickness introduces free surface curvature.

Considering that FAM is a two-dimensional method, information of the third dimension, the film thickness distribution, is carried within the control area face-centre values. Thus, from the FAM point of view, a droplet is seen as a set of all control areas where the average face-centre value of thickness is greater than the precursor film thickness (Figure 5.2). In other words, CAs with face-centre thickness equal to h_p are considered completely dry. Since the precursor film is uniformly distributed across the whole dry spatial domain, interpolated edge-centre thickness values for dry CAs will also be equal to h_p.

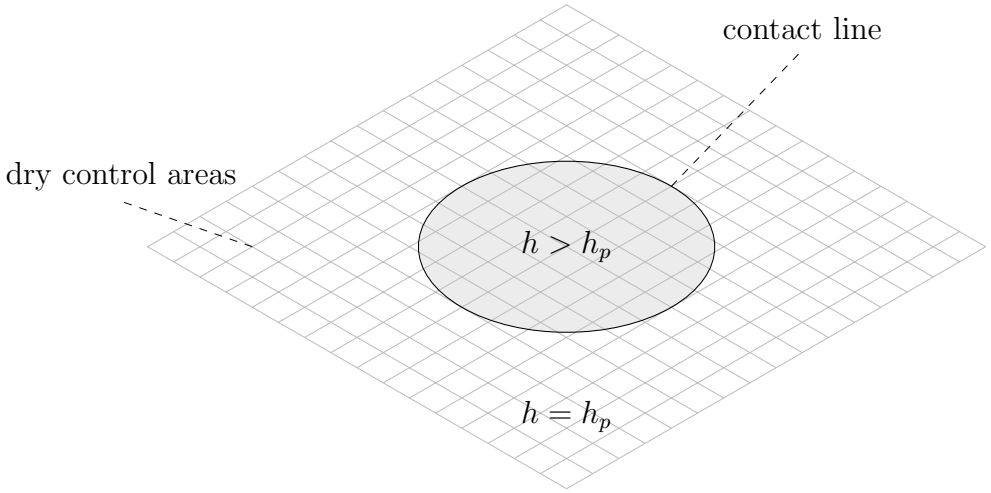

Figure 5.2: Droplet represented by finite area mesh

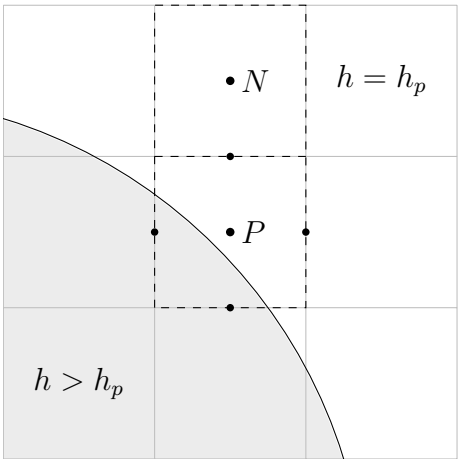

Figure 5.3: Contact line location in the control area

The partially wet CAs (where the contact line exists) inevitably have face-centre thickness greater than the dry CAs. However, partially wet CAs need to have at least one edge-centre value of thickness equal to h_p as they share an edge with a dry CA, as illustrated in Figure 5.3. Thus, CAs which contain the contact line can be determined as those which have at least one completely dry neighbouring CA.

5.2.4. Discretisation of the Contact Angle Force

The contact angle force is given by the equation (5.15) as:

$$\mathbf{f}_\theta = \beta\sigma(1 - \cos\theta)\mathbf{n}_{cl} \, .$$

Film thickness represents the quantity which separates wet from dry areas and the unit normal vector to the contact line $\mathbf{n}_{cl}$ can be expressed with the relation developed for the continuum surface force model by [30]:

$$(\mathbf{n}_{cl})_P = \frac{(\nabla_s h)_P}{|(\nabla_s h)_P|} \, , \tag{5.17}$$

with the thickness surface gradient used as the *color-function*. The face-centre gradient $(\nabla_s h)_P$ is approximated using the expression (4.38).

In order to calculate the apparent contact angle θ using the Kistler's model (2.4) local capillary number has to be known:

$$\mathrm{Ca}_P = \frac{\mu(v_{cl})_P}{\sigma} \, , \tag{5.18}$$

with v_{cl} being the contact line velocity. Several ways of modelling the contact line velocity were given in Section 5.1., all of which represent the velocity as a function of dot-product $\mathbf{n}_w \cdot \mathbf{n}_{cl}$. In FAM, the normal to contact line $\mathbf{n}_{cl}$ is defined as tangential to the substrate surface. Thus, the dot-product is equal to zero, and both expressions (5.3) and (5.5) get reduced to:

$$(v_{cl})_P = (\mathbf{n}_{cl})_P \cdot \bar{\mathbf{v}}_P \, . \tag{5.19}$$

Once the contact line velocity is determined, local capillary number is calculated using the equation (5.18). The apparent contact angle can be then expressed using Kistler's model (2.4):

$$\theta_P = f_{\mathrm{H}}(\mathrm{Ca}_P + f_{\mathrm{H}}^{-1}(\theta_e)) \, ,$$

with θ_e taking the values of the advancing θ_a or the receding contact angle θ_r, depending on the contact line velocity direction.

With the contact angle force $\mathbf{f}_\theta$ determined, the additional line integral from (5.16) can be approximated as:

$$\frac{1}{\rho} \oint_{L_{cl}} \mathbf{f}_\theta dL \approx \frac{1}{\rho} \left(\frac{\mathbf{f}_\theta}{L_{PN}} \right)_P^n S_P \, , \tag{5.20}$$

and added into equation (4.32). Quantity L_{PN} stands for the length of geodetic distance $\overline{PeN}$ (Figure 4.5), included to keep dimensional consistency. Having the tangential term inversely proportional to the geodetic distance introduces high mesh dependency on the solution.

Finally, the fully discretised momentum equation for the partially wet CAs reads as:

$$a_P^v \bar{\mathbf{v}}_P^n + \sum_N a_N^v \bar{\mathbf{v}}_N^n = \mathbf{r}_P^v - \frac{1}{\rho} \{ [\nabla_s (hp)]_P^n - p_P^n (\nabla_s h)_P^n \} \, , \tag{5.21}$$

with the contact angle force term $\frac{1}{\rho}(\mathbf{f}_\theta / L_{PN})_P^n$ included into the source term $\mathbf{r}_P^v$, together with other tangential contributions.

5.2.5. Solution Procedure

Numerical solution procedure is composed of these steps:

1. switch to the new time step and initialise the values of all dependent variables with the values from the previous time step;

2. update velocity profiles for all computational points in the mesh;

3. identify partially wetted cells;

4. for partially wetted cells:

   (a) calculate interface normal in the surface-tangential plane from (5.17):

   $$(\mathbf{n}_{cl})_P = \frac{(\nabla_s h)_P}{|(\nabla_s h)_P|} ,$$

   (b) calculate contact line propagation velocity using (5.19):

   $$(v_{cl})_P = (\mathbf{n}_{cl})_P \cdot \bar{\mathbf{v}}_P ,$$

   and identify the front as advancing or receding with (5.6) and (5.7):

   $$\bar{\mathbf{v}}_P \cdot (\mathbf{n}_{cl})_P > 0 \text{ (advancing front)} ,$$

   $$\bar{\mathbf{v}}_P \cdot (\mathbf{n}_{cl})_P < 0 \text{ (receding front)} ;$$

   (c) calculate the local capillary number from (5.18):

   $$\mathrm{Ca}_P = \frac{\mu (v_{cl})_P}{\sigma} ,$$

   (d) calculate the dynamic contact angle using (2.4):

   - for advancing front:

   $$(\theta_d)_P = f_{\mathrm{H}}(\mathrm{Ca}_P + f_{\mathrm{H}}^{-1}(\theta_a)) ,$$

   - for receding front:

   $$(\theta_d)_P = f_{\mathrm{H}}(\mathrm{Ca}_P + f_{\mathrm{H}}^{-1}(\theta_r)) ;$$

   (e) calculate the contact angle force from (5.15):

   $$\mathbf{f}_\theta = \beta\sigma(1 - \cos\theta)\mathbf{n}_{cl} .$$

   (f) assemble the momentum equation (5.21) for partially wetted CAs:

   $$a_P^v \bar{\mathbf{v}}_P^n + \sum_N a_N^v \bar{\mathbf{v}}_N^n = \mathbf{r}_P^v - \frac{1}{\rho}\{[\nabla_s(hp)]_P^n - p_P^n (\nabla_s h)_P^n\} ,$$

   with the contact angle force term $\frac{1}{\rho}(\mathbf{f}_\theta / L_{PN})_P^n$ included into the source term $\mathbf{r}_P^v$;

5. assemble the momentum equation (4.44) for every completely wetted and dry CAs:

$$a_P^v \bar{\mathbf{v}}_P^n + \sum_N a_N^v \bar{\mathbf{v}}_N^n = \mathbf{r}_P^v - \frac{1}{\rho}\{[\nabla_s(hp)]_P^n - p_P^n(\nabla_s h)_P^n\} ;$$

6. assemble equations (5.21) and (4.44) into:

$$[A^v][\bar{\mathbf{v}}] = [\mathbf{r}^v] , \tag{5.22}$$

   where $[A^v]$ is a sparse matrix consisted of coefficients a_P^v on the diagonal and a_N^v off the diagonal, $[\bar{\mathbf{v}}]$ is a vector consisting of the mean film velocity for each CA and $[\mathbf{r}^v]$ is a vector consisting of right hand side of equations and for each CA in the mesh;

7. solve equation (5.22) for average film velocity $\bar{\mathbf{v}}$;

8. calculate the edge bi-normal velocity using (4.48):

$$(\mathbf{m} \cdot \bar{\mathbf{v}})_e^n = \mathbf{m}_e \cdot \left(\frac{\mathbf{H}}{a}\right)_e^n - \left(\frac{1}{a}\right)_e^n \frac{1}{\rho}\{\mathbf{m}_e \cdot [\nabla_s(hp)]_e^n - p_e^n \mathbf{m}_e \cdot (\nabla_s h)_e^n\} ;$$

9. write the continuity equation (4.49) for each CA:

$$a_P^h h_P^n + \sum_N a_N^h h_N^n = \mathbf{r}_P^h ;$$

10. assemble equation (4.49) into:

$$[A^h][h] = [r^h] , \tag{5.23}$$

    with $[A^h]$ being a sparse matrix consisted of coefficients a_P^h and a_N^h, $[h]$ vector containing film thickness values for every CA and $[r^h]$ being the vector containing right hand sides of equation for every CA in the mesh;

11. solve equation (5.23) for film thickness h;

12. update liquid film pressure using (4.39):

$$p_P = -\sigma_P C_P - \sigma_P(\nabla_s \cdot \nabla_s h)_P - \mathbf{n}_P \mathbf{f}_P h_P ;$$

13. return to step 1 if converged solution is reached, otherwise return to step 2.

Chapter 6.

Results

Boundary condition written for the `interFoam` solver was tested by performing a simulation of water droplet impact onto an inclined plate (Section 6.1.). The results were compared to experimental data. Same experiment could not be recreated in `liquidFilmFoam` solver, due to its limitation to contact angles less or equal to 90°. Instead, a rivulet flow simulation was performed and compared to experimental and numerical data (Section 6.2.). Methods were compared using a case of droplet exposed to shear flow on an inclined plate (Section 6.3.).

6.1. Wetting of an Inclined Plate with VoF method

6.1.1. Experimental Set-Up

Droplets impacting inclined, dry walls were studied experimentally in [49], using high resolution digital photography and short exposure times. The geometry of impact is given in Figure 6.1 (a). Inclination angle α is defined as the angle between the droplet velocity vector (parallel to gravity and denoted with u in [49]) and the tangent to the plate.

Definition of measured quantities is shown in Figure 6.1 (b). Here x_{back} refers to the length of the contact line in backwards direction from the point of impact. Similarly, x_{front} is the contact line elongation in forward direction from the point of impact. Length y_a refers to the droplet height.

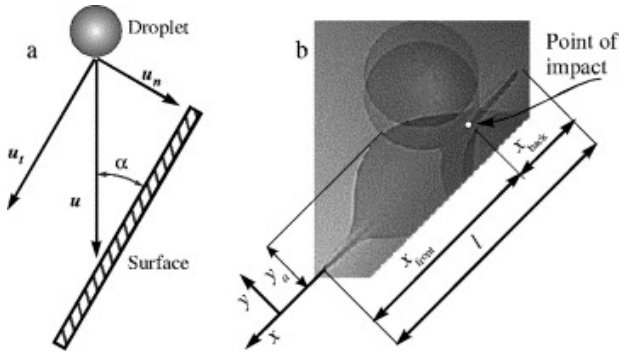

Figure 6.1: Geometry of droplet impact (a) and side view of a droplet on an inclined surface (b)

The aforesaid parameters were made dimensionless by dividing them with the droplet initial diameter:

$$x^* = \frac{x}{D}\,. \tag{6.1}$$

Spread factor x^* from the equation above determines the amount of spreading: front spread factor is defined for $x = x_{front}$ and back spread factor is defined for $x = x_{back}$. Time is also made dimensionless by multiplying it with the ratio of impact velocity magnitude v and initial diameter D:

$$t^* = \frac{tv}{D}\,. \tag{6.2}$$

Instant $t^* = 0$ corresponds to the droplet's first contact with the surface. Another quantity of interest is the initial Weber number, which represents the ratio of inertia to surface tension forces:

$$\mathrm{We} = \frac{\rho v^2 D}{\sigma}\,, \tag{6.3}$$

where ρ is the liquid density, v the initial velocity magnitude, D the initial droplet diameter and σ the surface tension coefficient. Liquid and substrate properties are shown in Table 6.1.

Table 6.1: Water and substrate properties

Smooth glass hysteresis	$\theta_r = 6°, \theta_a = 10°$
Smooth wax hysteresis	$\theta_r = 95°, \theta_a = 105°$
Surface tension, [N/m]	0,073
Dynamic viscosity, [mPas]	1,0
Density, [kg/m^3]	996
Droplet diameter, [mm]	2,7

6.1.2. Case Set-Up

In order to test the contact angle boundary condition, three experimental cases were numerically recreated:

- droplet impacting smooth glass substrate, $\alpha = 10°$ and We = 391;
- droplet impacting wax substrate, $\alpha = 10°$ and We = 391;
- droplet impacting smooth glass substrate, $\alpha = 45°$ and We = 90.

The computational domain for all cases consists of a rectangular cuboid of dimensions $6 \times 14 \times 4$ mm^3, with one of the boundaries representing the substrate and other 5 representing the atmosphere (Figure 6.2). Types of boundary conditions used at these boundary patches are given in Table 6.2.

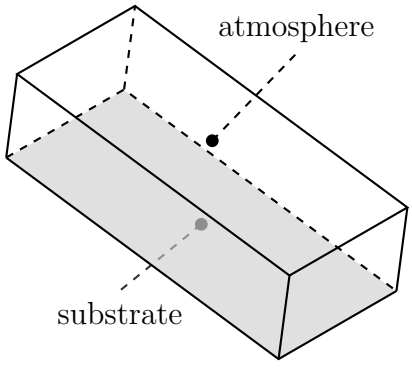

Figure 6.2: Computational domain for `interFoam` simulations

The wax substrate case used orthogonal mesh of $2,7 \cdot 10^6$ cells, with $0,05 \times 0,05 \times 0,02$ mm^3 being the dimensions of the cells at the substrate boundary. Glass substrate cases

used coarser mesh of $420 \cdot 10^3$ cells, with cells of dimensions $0,1 \times 0,1 \times 0,03$ mm^3 at the substrate boundary. Since it was determined that the mesh resolution did not significantly affect results for the glass substrate cases, additional mesh refinement was not performed.

Initial position and velocity of the droplet is specified using `setFields` utility. Plate inclination angle is accounted for by rotating the gravity vector. All cases used adjustable time step, with the maximum Courant number of 0,2. Numerical schemes used for `interFoam` simulations are given in Table 6.3.

Table 6.2: Boundary condition types

Substrate	
Velocity	`fixedValue`
Pressure	`fixedFluxPressure`
Water phase fraction	`dynamicKistlerAlphaContactAngle`
Atmosphere	
Velocity	`pressureInletOutletVelocity`
Pressure	`totalPressure`
Water phase fraction	`inletOutlet`

Table 6.3: Finite volume numerical schemes

Time schemes	
default	Euler
Gradient schemes	
default	Gauss linear
grad(U)	Gauss linear
alpha1	Gauss linear
Divergence schemes	
div(rho*phi,U)	Gauss limitedLinearV 1
div(phi,alpha)	Gauss Gamma 0.2
div(phirb,alpha)	Gauss interfaceCompression
Laplacian schemes	
default	Gauss linear corrected
Interpolation schemes	
default	linear
Surface normal gradient schemes	
default	corrected

6.1.3. Results

Comparison of numerically predicted and experimentally determined droplet shape evolution for the case of smooth glass substrate, inclination angle of $\alpha = 10°$ and Weber number We = 391 is shown in Figure 6.3. Time between the exposures is 1 ms.

Experiments confirmed that upon impacting glass, a highly hydrophilic substrate, droplet should experience only spreading motion. Numerical results, however, showed both spreading and sliding motion. The failure to capture this local contact line pinning is apparent in Figure 6.5. While the elongation in forward direction showed excellent agreement with the experiment, the backward spread factor progressively deviated in time.

Shape-wise comparison for the case of smooth wax substrate, inclination angle $\alpha = 10°$ and Weber number We = 391 is shown in Figure 6.4. Opposed to glass, wax is a hydrophobic substrate, and allows both spreading and sliding motion. However, the

sliding motion achieved by the simulation was moderately exaggerated compared to the experiment, which is evident in the backward spread factor curve shown in Figure 6.6. Estimation of front spread factor again showed excellent agreement with the experiment.

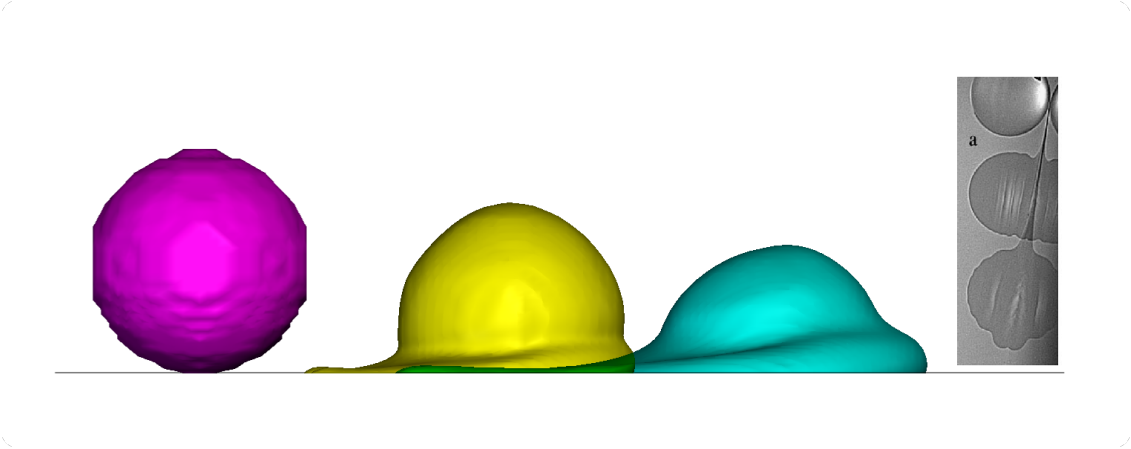

Figure 6.3: Deposition of water droplet on a smooth glass substrate

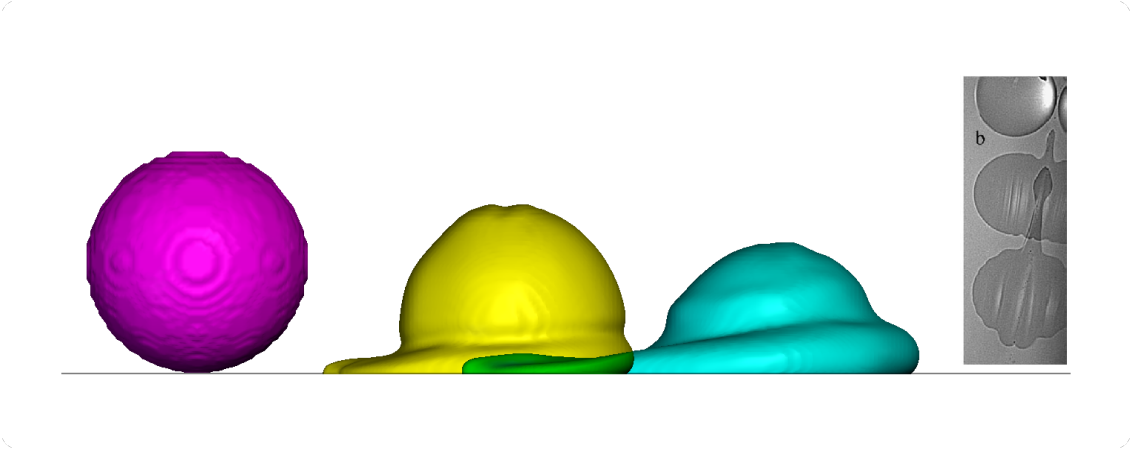

Figure 6.4: Deposition of water droplet on a wax substrate

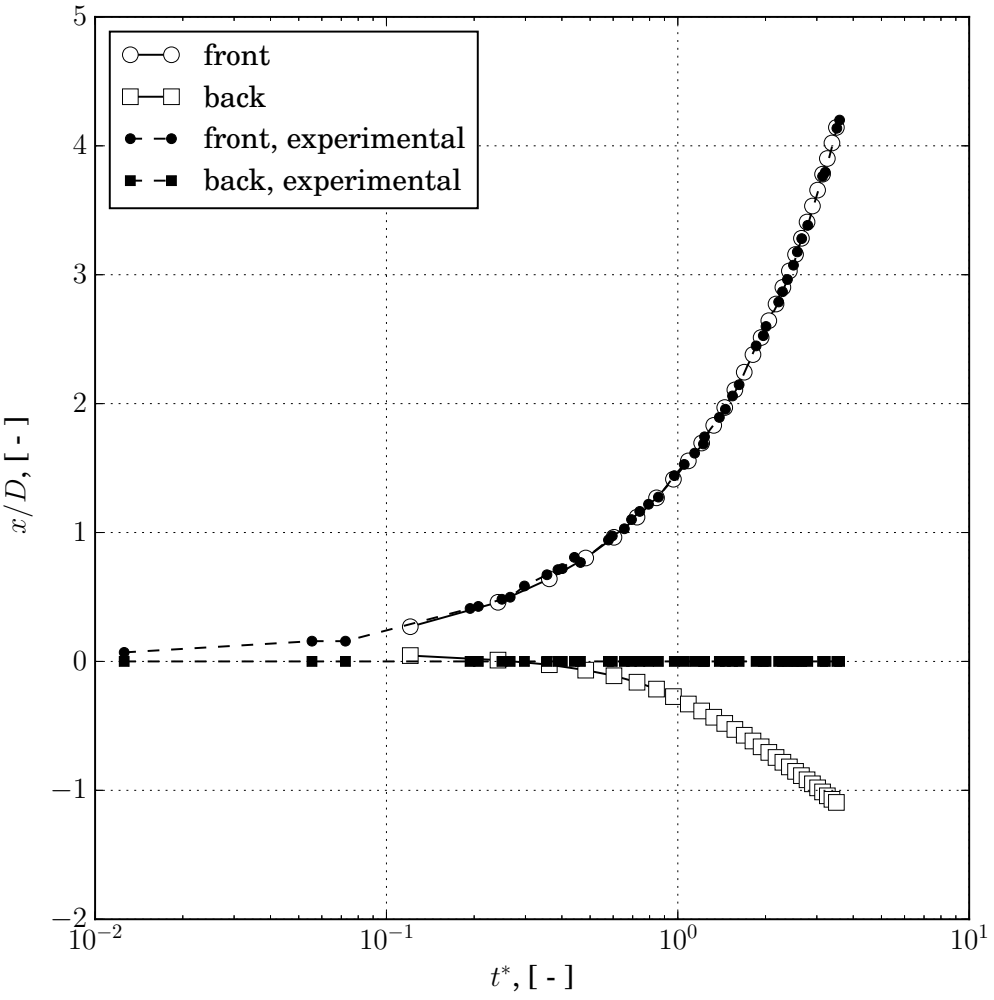

Figure 6.5: Spread factor for a smooth glass substrate, $\alpha = 10°$ and We = 391

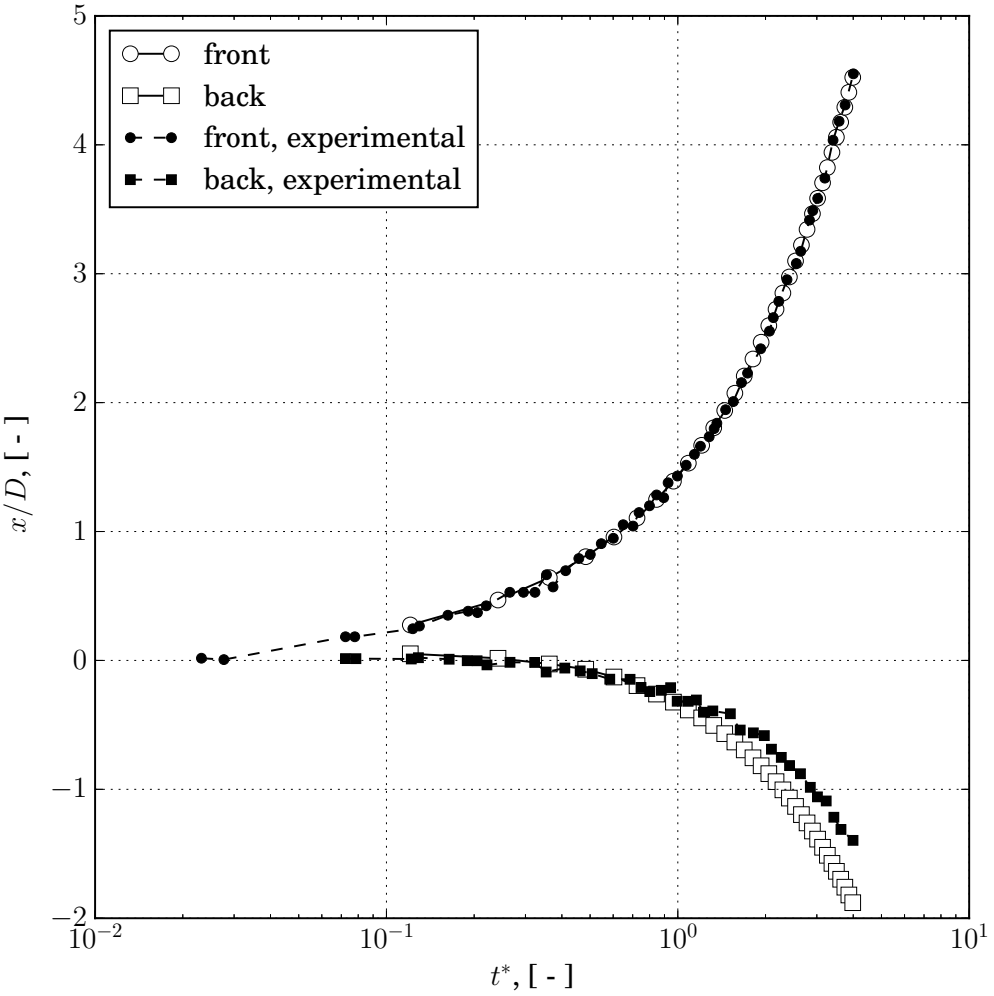

Figure 6.6: Spread factor for a wax substrate, $\alpha = 10°$ and We = 391

Figure 6.7 shows spread factors for the case of a smooth glass substrate, inclination angle $\alpha = 45°$ and Weber number We = 90. The increase of surface tension influence, compared to previous cases, had a negative effect on the results: back spread factor is highly overestimated and front spread factor moderately in later stage of droplet deposition. Prediction of droplet apex height (Figure 6.8) exhibited excellent agreement with the experiment.

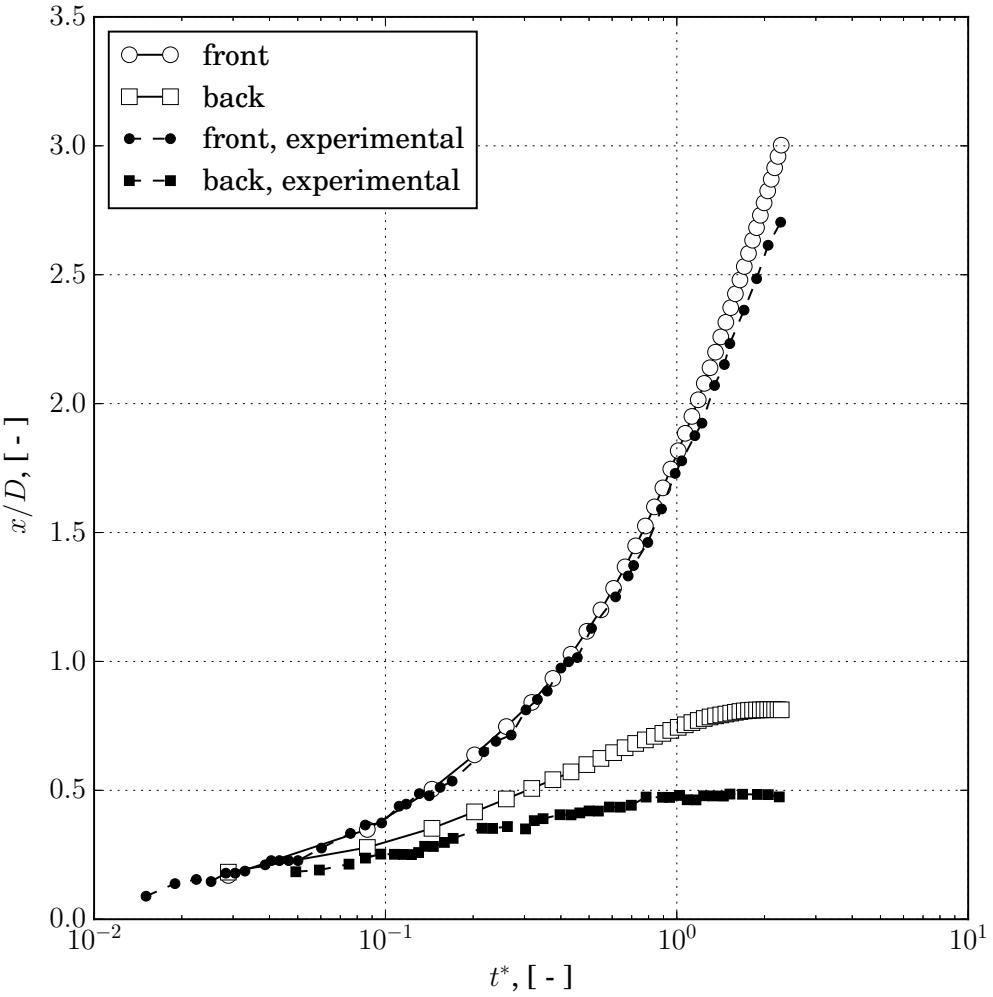

Figure 6.7: Spread factor for a smooth glass substrate, $\alpha = 45°$ and We $= 90$

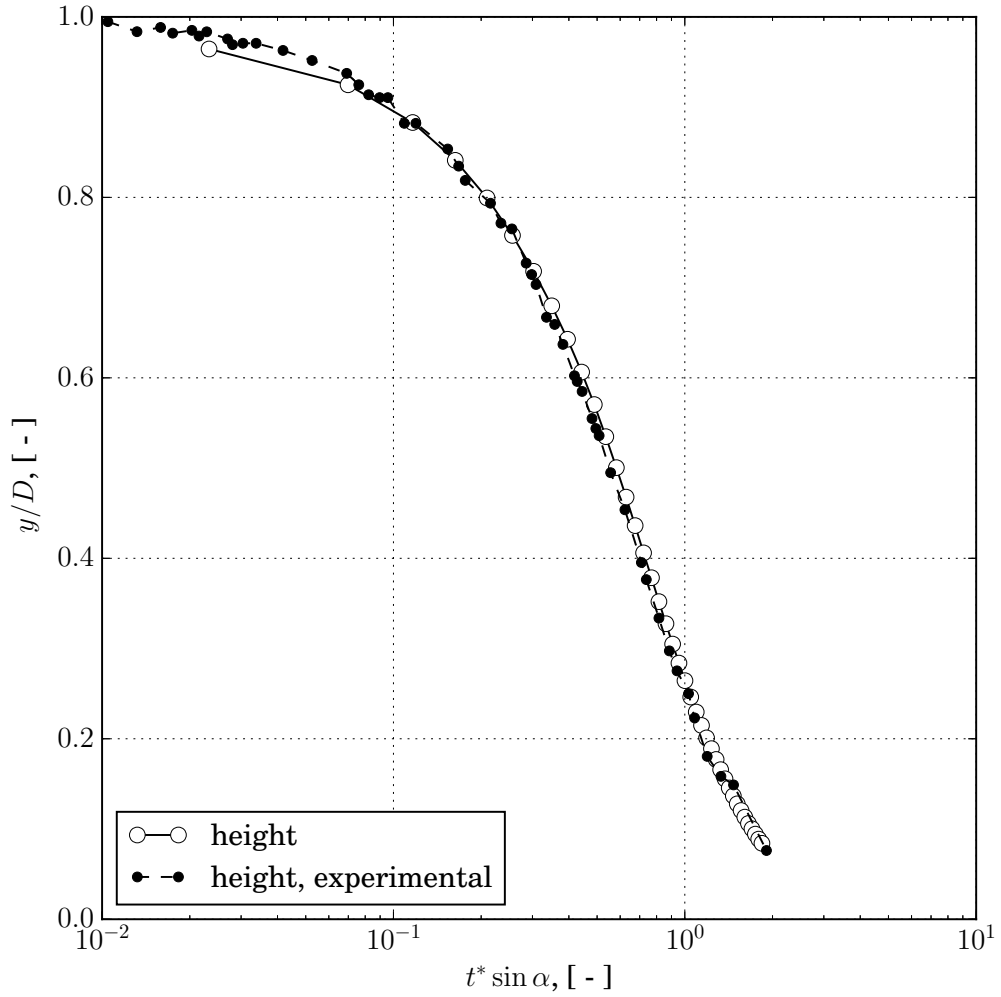

Figure 6.8: Droplet height for a smooth glass substrate, $\alpha = 45°$ and We = 90

Discrepancies between the experiments and numerical results regarding the receding motion could be due to the contact angle model itself. While the contact line should locally impinge on the glass substrate (Figure 6.5), simulation predicted sliding motion. Impingement is a consequence of the contact angle hysteresis and represents a static situation. Kistler's contact angle model, by its definition, calculates only dynamic contact angles, outside of the hysteresis band. Thus, receding motion problems could potentially be solved by expanding the boundary condition so that it takes contact angle hysteresis

into account.

Negative effects of increased surface tension influence on the results could be linked to numerical errors in calculation of 3-D gradients, needed for interface curvature terms. This is a well-know issue in literature, and it is described for example in [50].

6.2. Rivulet Flow with Thin Liquid Film Model

6.2.1. Experimental Set-Up

In order to validate their model for partial wetting, [48] conducted experimental simulation of rivulet flow, using test apparatus specially designed to generate uniform water flow. A vertical cast acrylic plate ($0,61$ m wide and $1,22$ m long) was used as a substrate. Heated tap water ($43°$) was discharged onto the upper end of the plate through laterally positioned perforated copper tube ($1,27$ cm diameter and $0,51$ m long). Water was discharged onto the plate out of sixty holes of 1 mm diameter. In order to achieve uniform initial flow, prior to impacting the plate, water streams were forced through a diffusive medium attached to the upper end of the plate. Water flow rates were measured using a flow meter and images were captured using an IR camera. Heated water properties are shown in Table 6.4.

Table 6.4: Water properties at 43°

Surface tension, [N/m]	0,0696
Dynamic viscosity, [mPas]	0,618
Density, [kg/m^3]	991

6.2.2. Case Set-Up

In [48], rivulet flow was observed for low flow rates. In this thesis, the case of water being discharged onto vertically positioned plate at flow rate $\Gamma = 73$ g/m/s was numerically recreated. The flow rate was approximated by specifying the film thickness at the inlet boundary with value of $9,24 \cdot 10^{-5}$ m and by specifying the internal field with velocity of magnitude 1,56 m/s.

The computational domain is a rectangle of dimensions $0,61 \times 1,22$ m^2 (Figure 6.9). Upper edge is denoted as inlet. Here the initial film thickness is specified, using `fixedValue` boundary condition type, with value given by a non-uniform scalar list. Velocity at the inlet uses `zeroGradient` boundary condition type. Other three edges are denoted as atmosphere. Both velocity and film thickness at atmosphere edges use `zeroGradient` boundary condition type. Internal field value of Manning field, needed for viscous stress calculation, is set at 0,01 m.

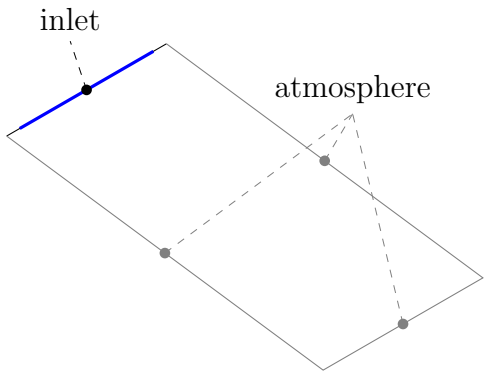

Figure 6.9: Computational domain for `liquidFilmFoam` simulations

In order to test mesh-dependency, three grid sizes were considered:

- coarse mesh of 61×122 control areas, with edge length of 10 mm;
- medium mesh of 122×244 control areas, with edge length of 5 mm;
- fine mesh of 244×488 control areas, with edge length of 2,5 mm.

Water on an acrylic substrate has the equilibrium contact angle in the range of 70°. Numerical simulation in [48] used statistical approach for determining dynamic contact angles, with standard deviation of 10° and a mean value of 75°. Thin liquid film formulation used in this thesis, uses Kistler's model for calculation of dynamic contact angles. Thus, here the receding contact angle is specified as $\theta_r = 66°$ and the advancing contact angle is specified as $\theta_a = 76°$.

All cases used adjustable time step, with the maximum Courant number of 0,2. Numerical schemes used for `liquidFilmFoam` simulations are given in Table 6.5.

Table 6.5: Finite area numerical schemes

Time schemes	
ddt(h,Us)	Euler
ddt(h)	Euler
Gradient schemes	
default	Gauss linear
grad(p)	Gauss linear
Divergence schemes	
default	none
div(phis,h)	Gauss upwind
div(phi2s,Us)	Gauss upwind
Laplacian schemes	
default	none
laplacian(h)	Gauss linear corrected
Interpolation schemes	
default	linear
Surface normal gradient schemes	
default	corrected

6.2.3. Results

A qualitative visual comparison of the flow behaviour achieved in experimental conditions and by numerical simulation from [48] is shown in Figure 6.10. Experiments observed meandering flow for low flow rates. This break-up of liquid into meandering streams occurs due to fluctuations at the inlet, surface roughness of the substrate, thermocapillary instabilites and other causes of upstream disturbances. Simulation performed by [48], achieved this behaviour by statistical treatment of the contact angle: at each computational cell a random contact angle is chosen from a normal distribution and is fixed for the duration of the calculation. The result of this approach is a contact angle that varies over the surface in a random manner. This gives rise to non-uniform flow and leads to the formation of rivulets and dry regions.

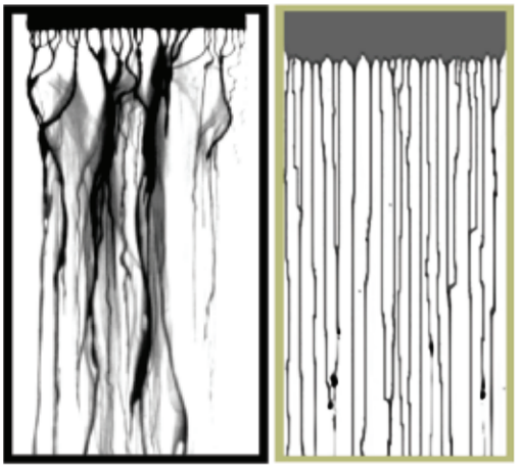

Figure 6.10: Rivulet flow - experiment (left), numerical solution (right)

Since contact angle model used in `liquidFilmFoam` depends on the velocity and substrate-liquid combination, the velocity vector was inclined at 1° in respect to the gravity axis, in order to introduce numerical error which would cause non-uniform velocity distribution across the computational space.

This method did yield a meandering flow, however, it took longer for the disturbance to propagate, causing a flooded flow at the top of the domain and rivulet flow at the bottom, as visible in Figure 6.11, 6.12 and 6.13. The flooded flow showed tendency to propagate in time, meaning that the contact angle force, as implemented in `liquidFilmFoam`, was not able to counteract the effects of inertia.

To test the mesh-dependency of the solution, three uniform grid spacings were considered:

- a coarse mesh, with edge length of 10 mm (Figure 6.11);
- a medium mesh, with edge length of 5 mm (Figure 6.12);
- a fine mesh, with edge length of 2,5 mm (Figure 6.13).

Numerical solution from [48] used uniform grid spacing of 3,8 mm.

Figure 6.11: Rivulet flow - coarse mesh

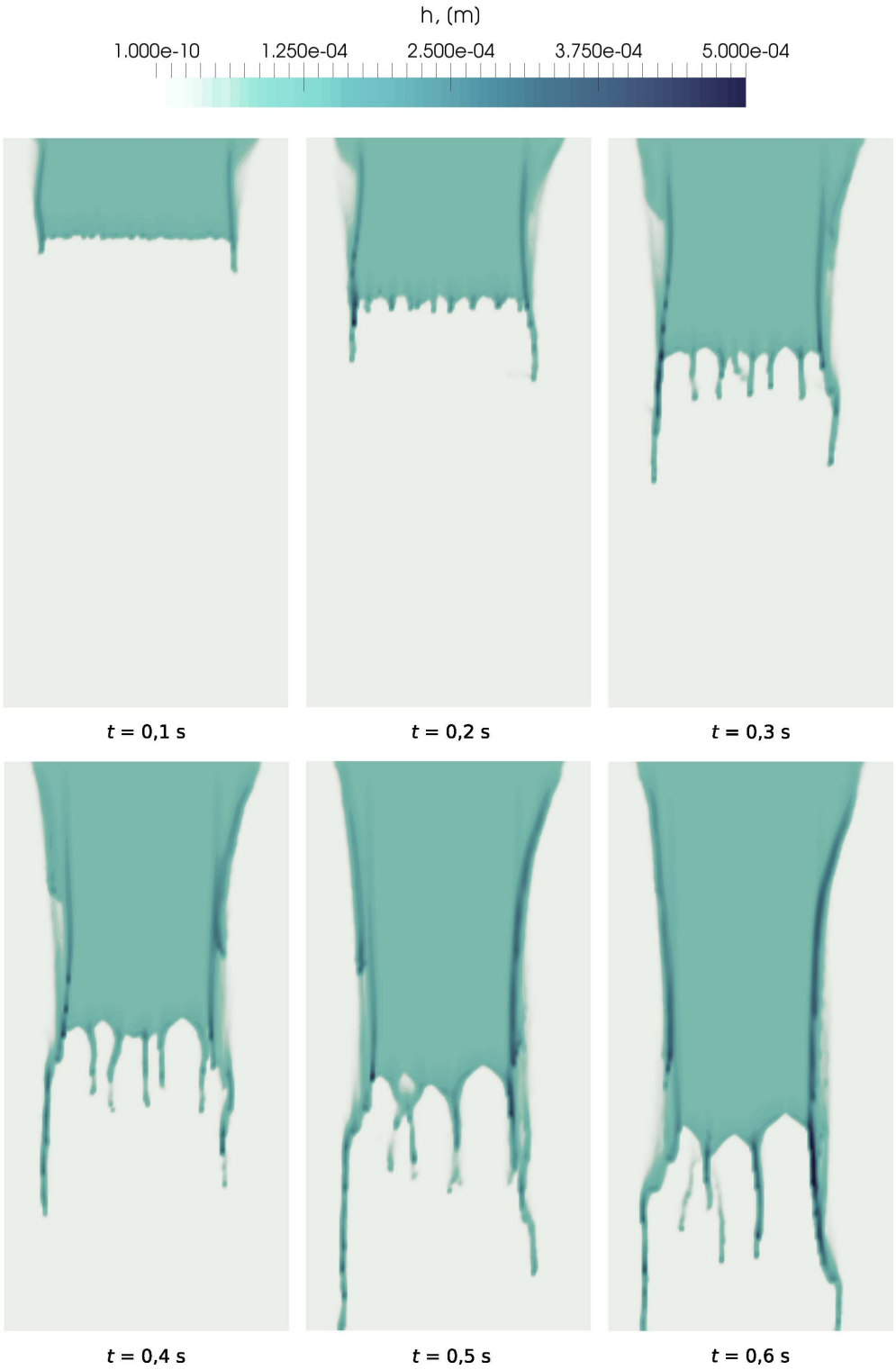

Figure 6.12: Rivulet flow - medium mesh

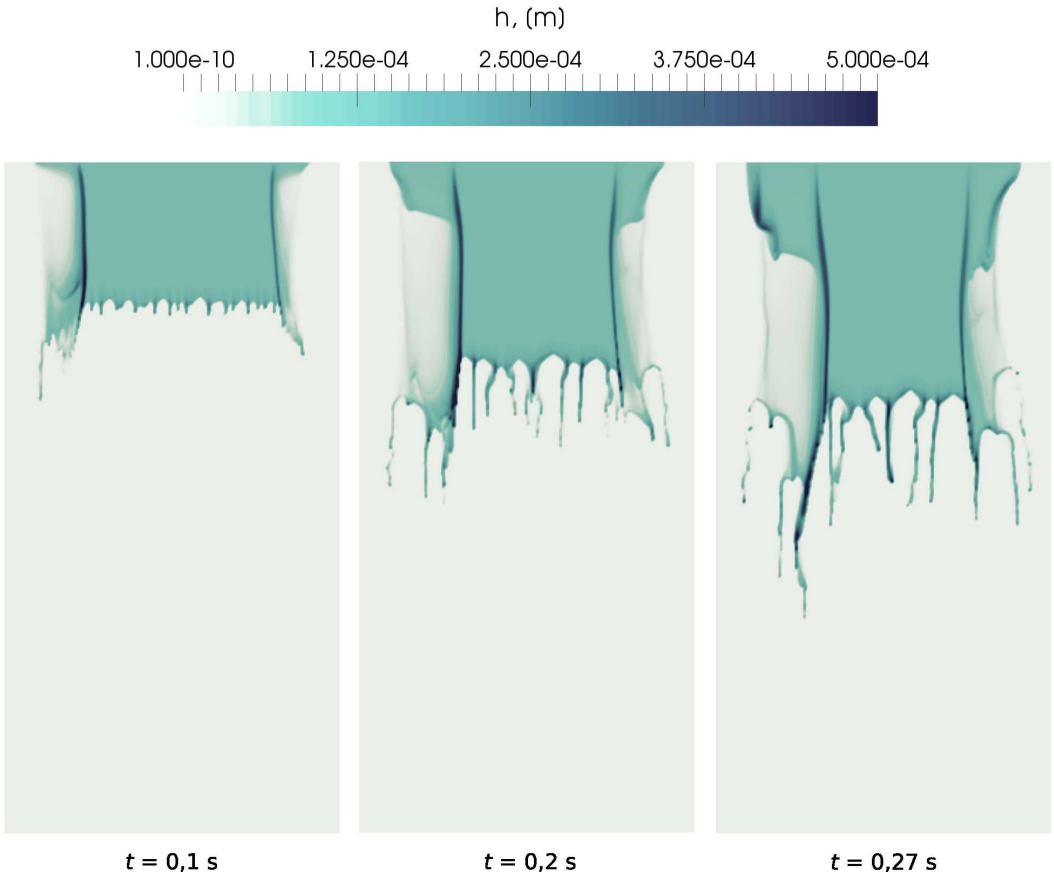

Figure 6.13: Rivulet flow - fine mesh

Mesh resolution has a two-fold effect on the solution:

1. Coarse mesh produced thick streams, as visible in Figure 6.11. Decreasing the edge length of the control area produced narrow streams and also captured individual droplets separating, as seen in Figure 6.13. In order to obtain physically consistent solutions, numerical length scales have to be appropriate. For rivulets and droplet flows, this implies very fine mesh resolutions.

2. In order to keep the dimensional consistency, the contact angle force was divided with the geodetic distance between the neighbouring computational cell centroids. This leads to inverse proportionality: small geodetic distance implies large force magnitude. Dependence of the contact angle force on the film thickness gradients (equation (5.17)) leads to numerical errors which give rise to un-physical velocities

and cause the divergence of the solution. In the case of fine mesh (Figure 6.13), simulation diverged at time step $t = 0,27$ s, not reaching the final solution.

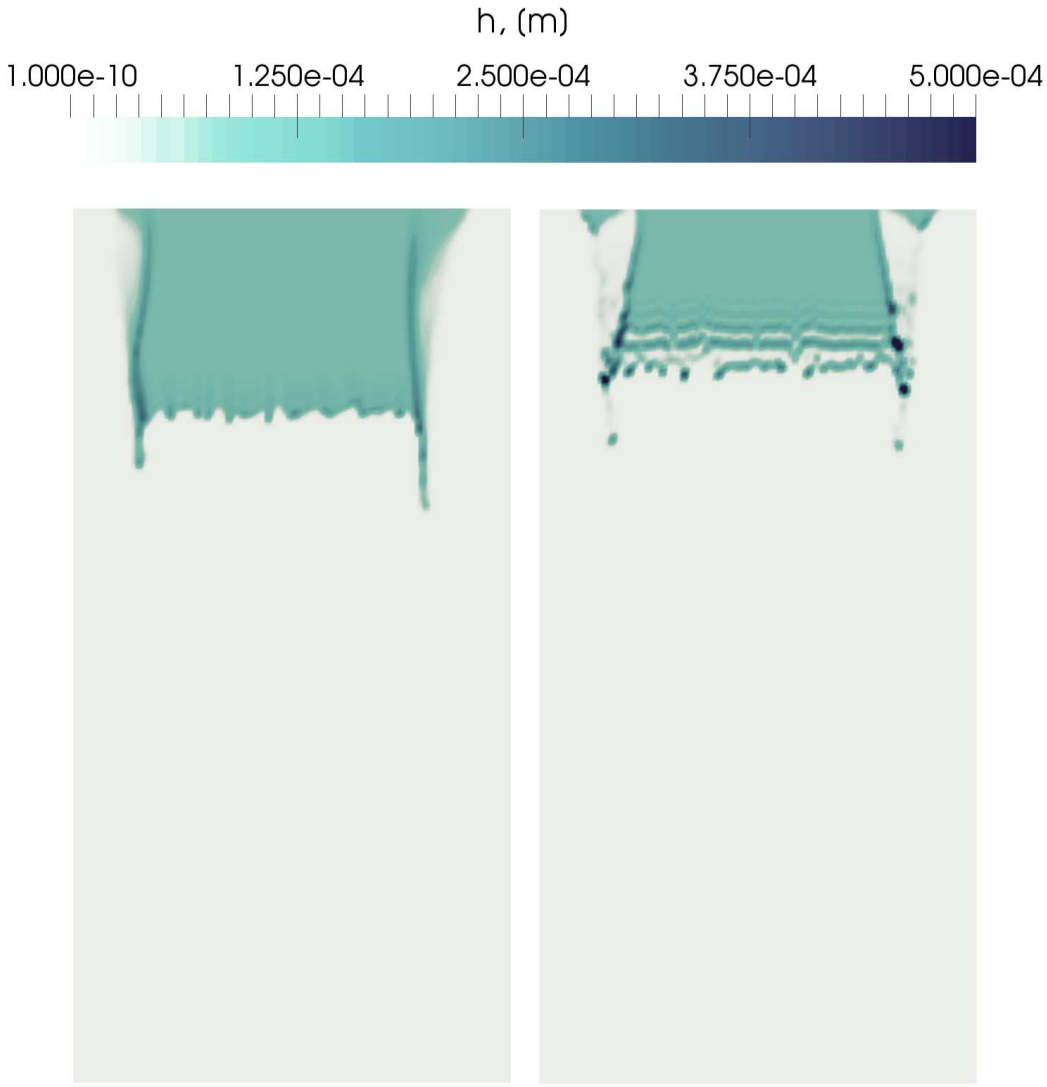

Figure 6.14: `Gauss upwind` scheme (left), `Gauss Gamma 0.5` scheme (right)

The case of medium mesh (5 mm control area edge length) was recreated using the blended `Gamma 0.5` divergence scheme. Figure 6.14 shows comparison of the solutions for time step $t = 0,15$ s. The `Gamma 0.5` divergence scheme caused liquid film separation, but in an un-physical manner, not observed by the experiment. Issues concerning the solution divergence become even more apparent when applied to droplet flows, which

will be described within the following section.

6.3. Method Comparison

6.3.1. Case Set-Up

In order to compare results obtained by both methods, a simulation of droplet exposed to a shear flow on an inclined plate was performed. Initial shape of the droplet is a cut sphere, with contact line radius of 1,5 mm and droplet height of 1 mm. In `interFoam`, initial droplet shape is set using the `setFields` utility, while in `liquidFilmFoam` the same was done using the `setInitialDroplet` utility.

The inclination angle of the plate is 45°, which was accounted for by rotating the gravity vector. In both cases the velocity vector was tangential to the substrate surface with magnitude of 1 m/s. Liquid and substrate properties are shown in Table 6.6.

Table 6.6: Liquid and substrate properties

Smooth glass hysteresis	$\theta_r = 6°, \theta_a = 10°$
Surface tension, [N/m]	0,073
Dynamic viscosity, [mPas]	1,0
Density, [kg/m^3]	996

The `interFoam` case used a domain of dimensions $8 \times 12 \times 3$ mm^3, with $160 \times 240 \times 60$ cells. Expansion rate for cells in z direction was set to 5, which amounts to a cell of dimensions $0,5 \times 0,5 \times 0,2$ mm^3 at the substrate boundary. Boundary conditions and numerical schemes are the same as described in Section 6.1.2.

The `liquidFilmFoam` case used a domain of dimensions 8×12 mm^2, with 160×240 control areas. At all domain edges `zeroGradient` boundary condition type was specified. Numerical schemes used for the `liquidFilmFoam` simulation are as given in Table 6.5.

Both simulations used adjustable time step, limited with maximum Courant number of 0,2.

6.3.2. Results

The comparison of droplet shape evolution achieved by both methods is shown in Figure 6.15. The droplet is shown for time instances: $t = 0$, $t = 3,5$ ms and $t = 7$ ms. The 3-D solution obtained by the `interFoam` solver is shown above, while the 2-D `liquidFilmFoam` solution is shown below, using deformed surface technique to represent scalar value of film thickness.

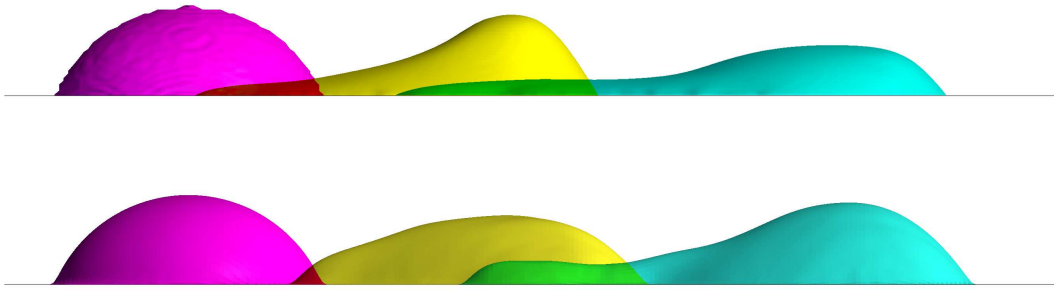

Figure 6.15: Droplet shape evolution with VoF (above) and thin liquid film model (below)

As seen in Figure 6.15, the solution obtained by `liquidFilmFoam` exaggerated both advancing and receding motion compared to the solution predicted by `interFoam`. Knowing that the `interFoam` solver has a tendency to overestimate the amount of sliding and spreading at low Weber numbers, it can be concluded that the `liquidFilmFoam` solver did not yield satisfactory results.

Back and front spread factor curves for both methods are shown in Figure 6.16. Receding and advancing motion was defined with the respect to the initial contact line centre. The advancing isohypses predicted by the thin liquid film model are moderately overestimated compared to the VoF front spread factor curve. Discrepancy is higher when the receding motion is compared.

Figure 6.17 shows droplet apex height predicted by both methods. It is visible that both methods experience some un-physical oscillations of liquid thickness. These oscillations are most noticeable in the solution obtained by `liquidFilmFoam` and are

linked to divergence issues described in Section 6.2.

It is important to note that these issues exist even without the model for partial wetting developed in this thesis. Thus, elimination of the oscillations remains a possible subject for future work.

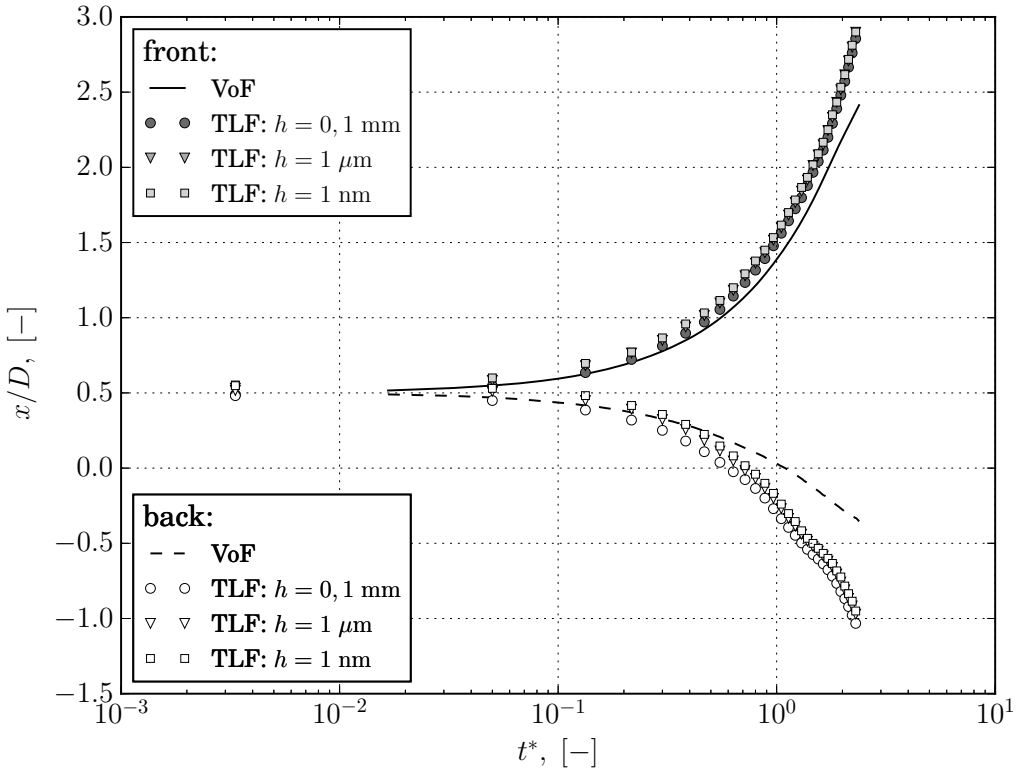

Figure 6.16: Spread factor for a smooth glass substrate, $\alpha = 45°$ and We $= 40$

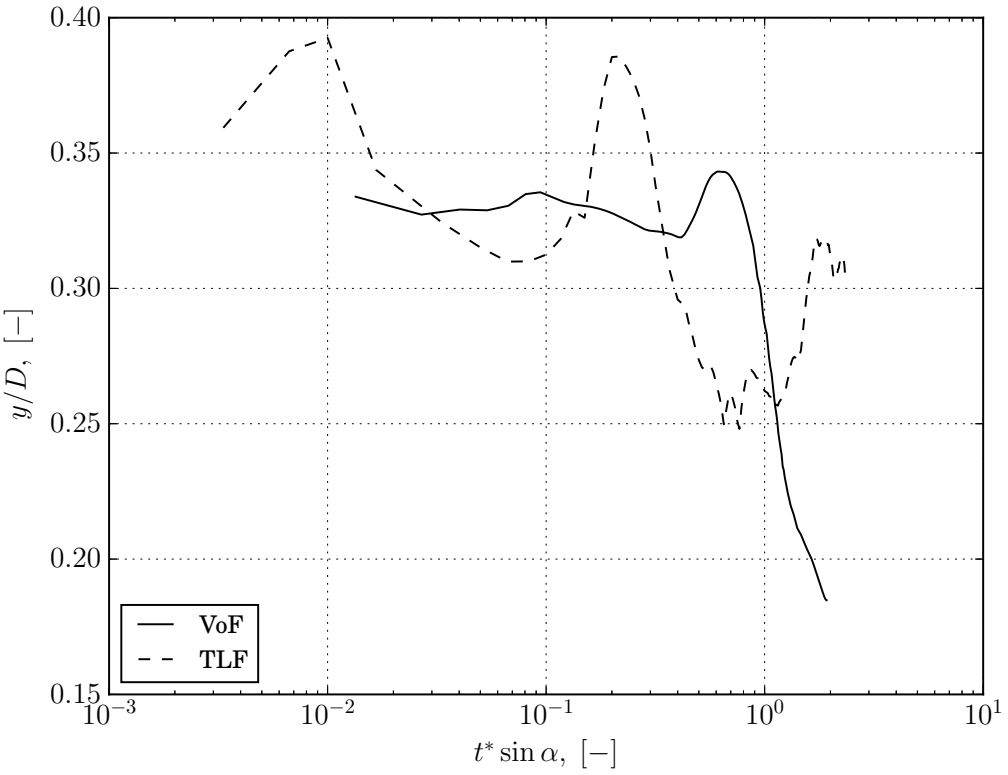

Figure 6.17: Droplet height for a smooth glass substrate, $\alpha = 45°$ and We = 40

Chapter 7.

Conclusion

The focus of this thesis was to examine the feasibility of CFD wall wetting simulations, using two model formulations. In 3-D VoF method, wetting was realized within a boundary condition based on Kistler's dynamic contact angle model. In 2-D thin liquid film model, a force term was added into the momentum equation to limit the liquid spreading. Quantity of the force term also depends on Kistler's contact angle model.

Implementation of Kistler's contact angle model in the 3-D VoF-based `interFoam` solver proved itself relatively successful when compared to experimentally observed behaviour of droplet wetting. Major disagreement with experiments was found for the receding motion of a droplet: for a hydrophilic substrate, simulation was not able to capture local contact line impingement and, for a hydrophobic substrate, the amount of sliding motion was overestimated. When implemented in 2-D thin liquid film `liquidFilmFoam` solver, Kistler's contact angle model exhibited a similar problem. Thus, probable cause for the discrepancies lies in the model itself. Being based on the hydrodynamic theory, this model is not able to recreate all of the phenomena associated with droplet wetting, most notably the hysteresis. More physically-consistent solution could be obtained by expanding the model with relations for contact line pinning.

The VoF method showed noticeably better results for inertia-driven flows. Issues related to surface tension dominated flows probably stem from numerical errors linked to the calculation of 3-D gradients needed for the interface curvature terms, which is a well-known problem in literature.

When studying wetting flows, mesh size is of utmost importance. In order to avoid premature and/or un-physical break-up of the interface, cell height has to be in the scale

of a few micrometers. Being three-dimensional, this makes the VoF method very time-consuming and therefore expensive. Thin liquid film model formulation has an advantage here, since this method approaches the matter two-dimensionally. However, being two-dimensional limits this method to contact angles less or equal to 90°. Thus, this method could potentially be used only for studying liquid interaction with hydrophilic substrates.

Being still in the development phase, `liquidFilmFoam` solver exhibits major issues related to solution divergence, which cause un-physical osciallations in liquid film thickness. Since these issues were not the focus of the thesis, causes remain undetermined. Thus, the final conclusion is yet to be found; a fair comparison of the methods remains a possible subject for future work.

Bibliography

[1] N. Roth A. Frohn. *Dynamics of Droplets*, chapter Miscellaneous Applications, pages 245–261. Springer-Verlag Berlin Heidelberg, 2000.

[2] D. Brutin. *Droplet Wetting and Evaporation*, chapter Introduction, pages xxiii–xxvii. Elsevier, 2015.

[3] T. van Hooff et al. 3d cfd simulations of wind flow and wind-driven rain shelter in sports stadia: Influence of stadium geometry. *Building and Environment*, 2010.

[4] A. Kubilay et al. Numerical modeling of turbulent dispersion for wind-driven rain on building facades. *Environ. Fluid. Mech.*, 2015.

[5] F. Gu et al. Cfd simulation of liquid film flow on inclined plates. *Chemical Engineering Technology*, 2004.

[6] AGARD-AR-344. Ice Accretion Simulation, 1997.

[7] M. B. Bragg. Aerodynamics of Supercooled Large-Droplet Ice Accretions and the Effect on Aircraft Control. Proceedings of the FAA International Conference on Aircraft Inflight Icing, Springfield, VA, Report No. DOT/FAA/AR-96/81, 1996.

[8] C. Antonini. *Superhydrophobicity as a strategy against icing: Analysis of the water/surface dynamic interaction for icing mitigation.* PhD thesis, University of Bergamo, 2011.

[9] Z. Wang et al. Numerical simulation for three-dimensional rotor icing in forward flight. *Advances in Mechanical Engineering*, 2018.

[10] Y. Cao et al. Numerical simulation of rime ice accretions on an aerofoil using an eulerian method. *Aeronautical Journal*, 2008.

[11] E. A. Whalen et al. Characteristics of Runback Ice Accretions and Their Aerodynamic Effects. Report No. DOT/FAA/AR-07/16, 2007.

[12] International Civil Aviation Organization. *Manual of Aircraft Ground De-icing/Anti-icing Operations*, 2018.

[13] D. C. Jenkins. Disintegration of raindrops by shockwaves ahead of conical bodies. *Philosophical Transactions of the Royal Society of London. Series A, Mathematical and Physical Sciences*, 1966.

[14] R. Sterkenburg M. J. Kroes. *Aircraft Maintenance and Repair, Seventh Edition*, chapter Rain-Removal Systems. AccessEngineering, 2013.

[15] O. Ubbink. *Numerical prediction of two fluid systems with sharp interfaces.* PhD thesis, Imperial College London, 1997.

[16] C. Kunkelmann. *Numerical Modeling and Investigation of Boiling Phenomena.* PhD thesis, Technische Universität, Darmstadt, 2011.

[17] N. Roth A. Frohn. *Dynamics of Droplets*, chapter Theory, pages 1–63. Springer-Verlag Berlin Heidelberg, 2000.

[18] O. Carrier D. Bonn. *Droplet Wetting and Evaporation*, chapter Liquid Spreading, pages 3–14. Elsevier, 2015.

[19] T. Young. Philosophical transactions: An essay on the cohesion of fluids. *Phil. Trans. R. Soc. Lond.*, 1805.

[20] O. Carrier D. Bonn. *Droplet Wetting and Evaporation*, chapter Contact Angles and the Surface Free Energy of Solids, pages 15–24. Elsevier, 2015.

[21] R. J. Good. *Surface and Colloid Science*, chapter Contact Angles and the Surface Free Energy of Solids, pages 1–29. Springer, Boston, MA, 1979.

[22] C. G. L. Furmidge. Studies at phase interfaces. i. the sliding of liquid drops on solid surfaces and a theory for spray retention. *Journal of Colloid Science*, 1962.

[23] S. F. Kistler. *Wettability*, chapter Hydrodynamics of Wetting, pages 311–429. Marcel Dekker, New York, 1993.

[24] R. L. Hoffman. A study of the advancing interface. i. interface shape in liquid—gas systems. *Journal of Colloid and Interface Science*, 1975.

[25] O. V. Voinov. Hydrodynamics of wetting. *Fluid Dynamics*, 1976.

[26] L. H. Tanner. The spreading of silicone oil drops on horizontal surfaces. *Journal of Physics D: Applied Physics*, 1979.

[27] N. Linder. *Numerical Simulation of Complex Wetting*. PhD thesis, Technische Universität, Darmstadt, 2015.

[28] R. G. Cox. The dynamics of the spreading of liquids on a solid surface. part 1. viscous flow. *Journal of Fluid Mechanics*, 1986.

[29] J. M. Haynes T. D. Blake. Kinetics of liquid/liquid displacement. *Journal of Colloid and Interface Science*, 1969.

[30] J.U. Brackbill et al. A continuum method for modeling surface tension. *Journal of Computational Physics*, 1992.

[31] H. Jasak. *Error analysis and estimation for finite volume method with applications to fluid flow*. PhD thesis, Imperial College of Science, Technology and Medicine, London, 1996.

[32] M. Perić. *A finite volume method for the prediction of three-dimensional flow in complex ducts*. PhD thesis, University of London, 1985.

[33] H. Jasak et al. High resolution nvd differencing scheme for arbitrarily unstructured meshes. *Numerical Methods in Fluids*, 1999.

[34] L. Mangani F. Moukalled, M. Darwish. *The Finite Volume Method in Computational Fluid Dynamics*, chapter The Finite Volume Method, pages 103–136. Springer International Publishing Switzerland, 2016.

[35] Ž. Tuković. *Metoda kontrolnih volumena na domenama promjenjivog oblika*. PhD thesis, Fakultet strojarstva i brodogradnje, Sveučilište u Zagrebu, 2005.

[36] Ž. Tuković. *Private conversations*, 2018.

[37] R.W. Powell. History of manning's formula. *Journal of Geophysical Research*, 1960.

[38] H. Jasak. Finite Area Method in OpenFOAM: Thin Liquid Film Model. Presentation slides, 2007.

[39] H. Jasak. *Private conversations*, 2018.

[40] L. E. Scriven C. Huh. Hydrodynamic model of steady movement of a solid/liquid/fluid contact line. *Journal of Colloid and Interface Science*, 1970.

[41] P. D. M. Spelt H. Ding. Onset of motion of a three-dimensional droplet on a wall in shear flow at moderate reynolds numbers. *Journal of Fluid Mechanics*, 2008.

[42] H. K. Moffatt. Viscous and resistive eddies near a sharp corner. *Journal of Fluid Mechanics*, 1964.

[43] A. N. Frumkin. On the phenomena of wetting and sticking of bubbles. *Zh. Fiz. Khim.*, 1938.

[44] B. V. Derjaguin. Theory of capillary condensation and related capillary effects: calculation of spreading action of polymolecular liquid films. *Zh. Fiz. Khim.*, 1940.

[45] D. R. J. Slade. *Gravity-Driven Thin Liquid Films: Rivulets and Flow Dynamics*. PhD thesis, The University of Leeds, School of Mechanical Engineering, 2013.

[46] N. V. Petviashvili V. S. Mitlin. Nonlinear dynamics of dewetting: kinetically stable structures. *Physics Letters*, 1994.

[47] B. V. Derjaguin N. V. Chuarev. Inclusion of structural forces in the theory of stability of colloids and films. *Journal of Colloid and Interface Science*, 1985.

[48] K. Meredith et al. *Computational Methods Multiphase Flow*, volume 6, chapter A Numerical Model for Partially-Wetted Flow on Thin Liquid Films, pages 293–250. WIT press, 2011.

[49] Š. Šikalo et al. Impact of droplets onto inclined surfaces. *Journal of Colloid and Interface Science*, 2005.

[50] D. J. E. Harvie. An analysis of parasitic current generation in volume of fluid simulations. *Applied Mathematical Modelling*, 2006.